MICROPHYSICS OF SURFACES

NANOSCALE PROCESSING

FEBRUARY 9–11, 1995

SANTA FE, NEW MEXICO

SPONSORED BY
OPTICAL SOCIETY OF AMERICA

Summaries of the papers presented at the topical meeting Microphysics of Surfaces: Nanoscale Processing
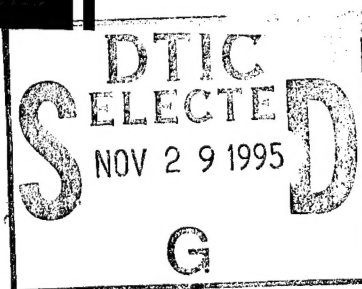
MICROPHYSICS OF SURFACES

NANOSCALE PROCESSING

February 9–11, 1995
Santa Fe, New Mexico

1995 Technical Digest Series
Volume 5

DTIC QUALITY INSPECTED 5

SPONSORED BY
Optical Society of America

Articles in this publication may be cited in other publications. To facilitate access to the original publication source, the following form for the citation is suggested:

Name of Author(s), "Title of Paper," in *Microphysics of Surfaces: Nanoscale Processing*, Vol. 5, 1995 OSA Technical Digest Series (Optical Society of America, Washington DC, 1995), pp. xx-xx.

Optical Society of America

Contents

Accesion For	
NTIS CRA&I	☒
DTIC TAB	☐
Unannounced	☐
Justification	
By	
Distribution /	
Availability Codes	
Dist	Avail and / or Special
A-1	

MICROPHYSICS OF SURFACES:
NANOSCALE PROCESSING

TECHNICAL PROGRAM COMMITTEE

Steven M. George, *University of Colorado, Chair*

Harry Atwater, *California Institute of Technology*

Joe Greene, *University of Illinois–Urbana*

Richard Hall, *Exxon Corporation*

Masataka Hirose, *Hiroshima University, Japan*

Francis A. Houle, *IBM Almaden Research Center*

†Richard M. Osgood, *Columbia University*

Thor Rhodin, *Cornell University*

Jeffrey Y. Tsao, *Sandia National Laboratories*

†OSA Technical Council Representative

ZIA B & C

8:30am–10:00am
MThA • Surface Analysis and Morphology During Processing
Phaedon Avouris, *IBM T. J. Watson Research Center, Presider*

8:30am (Invited)
MThA1 • STM characterization of surface processing: semiconductor etching, J. H. Weaver, *Univ. Minnesota.* This talk will review progress made in understanding surface etching of Si(100)-2×1 and GaAs(110) using halogens and atomic resolution scanning tunneling microscopy. **(p. 2)**

9:00am
MThA2 • Abstractive vs. dissociative chemisorption of molecular halogens on the Si(111)-7x7 surface: a molecular beam/STM study, J. A. Jensen, C. Yan, E. R. Behringer, A. C. Kummel, *UC–San Diego.* The direct chemisorption of F_2, Cl_2, and Br_2 is examined to determine the level of abstractive (single site) versus dissociative (two neighboring sites) chemisorption as a function of translational energy. **(p. 5)**

9:15am
MThA3 • STM measurements of the interaction of vacancies with steps during low-energy sputtering of Si(001), B. S. Swartzentruber, J. E. Houston, *Sandia National Laboratories;* C. M. Matzke, D. L. Kendall, *Univ. New Mexico.* We measure the evolution of the surface morphology of Si(001) during low-energy sputtering to extract the vacancy-step interaction kinetics. **(p. 6)**

9:30am
MThA4 • Morphology evolution and ion-induced surface transport during sputtering, T. M. Mayer, E. Chason, B. K. Kellerman, A. J. Howard, *Sandia National Laboratories.* We measure roughening and smoothing of surfaces during sputtering and develop a quantitative model including structure-dependent sputter yield and ion-induced viscous flow and surface diffusion. **(p. 9)**

9:45am
MThA5 • Development of surface morphology during the initial stages of CVD growth, D. P. Adams, T. M. Mayer, B. S. Swartzentruber, *Sandia National Laboratories.* We present a combined STM and rate equation analysis of the initial stages of FE layer growth by thermal decomposition of FE(CO)$_5$ on Si(100) substrates. **(p. 11)**

ANASAZI LOBBY

10:00am
Coffee Break

ZIA B & C

10:30am–12:00m
MThB • Nanostructure Fabrication Techniques
Joe Greene, *University of Illinois–Urbana, Presider*

10:30am (Invited)
MThB1 • Electron beam nanolithography, Christie R. K. Marrian, *U.S. Naval Research Laboratory.* The use of focused high energy electrons for nanolithography will be contrasted to the use of spatially localized low energy electrons from a scanning tunneling microscope. **(p. 16)**

11:00am (Invited)
MThB2 • Low-energy focused ion beam for nanofabrication, Kenji Gamo, *Osaka Univ., Japan.* Nanofabrication techniques using focused ion beams are discussed. These include low-energy FIB techniques and *in situ* fabrication to fabricate carrier confinement structure. **(p. 19)**

11:30am (Invited)
MThB3 • Nanostructure fabrication via atom optics, R. Gupta, J. J. McClelland, R. J. Celotta, *NIST–Gaithersburg.* We have demonstrated the use of an optical standing wave to focus chronium atoms into an array of nanometer-scale lines onto a silicon substrate. **(p. 22)**

12:00m–7:00pm
Afternoon Free

ZIA B & C

7:00pm–8:00pm
MThC • Surface Chemistry for Atomic Layer Control
Steven M. George, *University of Colorado, Chair*

7:00pm (Invited)
MThC1 • Surface chemistry of GaAs atmoic layer epitaxy, J. R. Creighton, C. M. Truong, *Sandia National Laboratories.* We review the surface chemical mechanisms and kinetics of GaAs atomic layer epitaxy and discuss the problems that have prevented its widespread utilization. **(p. 26)**

7:30pm
MThC2 • Atomic layer controlled deposition of Al_2O_3 films employing trimethylaluminum (TMA) and H_2O vapor, A. W. Ott, A. C. Dillon, H. K. Eaton, S. M. George, *Univ. Colorado;* J. D. Way, *Colorado School of Mines.* Sequential surface chemical reactions for the atomic layer controlled deposition of Al_2O_3 were studied using transmission Fourier transform infrared spectroscopy and atomic force microscopy. **(p. 29)**

7:45pm
MThC3 • Kinetic modeling of the atomic layer epitaxy window in Group IV semiconductor growth, Gyula Eres, *Oak Ridge National Laboratory.* The prospects for realizing atomic layer epitaxy of silicon are examined by modeling the overall surface-limited thin-film growth reaction in terms of two elementary steps. **(p. 32)**

ZIA B & C

8:00pm–10:00pm
MThD • Poster Session

MThD1 • Nanoscale characterization of InP islands on InGaP(001), V. Bressler-Hill, C. M. Reaves, S. Varma, S. P. DenBaars, W. H. Weinberg, *UC–Santa Barbara.* InP islands grown on InGaP(001) are characterized by atomic force microscopy. The effects of substrate orientation and surface roughness are discussed. **(p. 36)**

MThD2 • Micromanipulation of mono-disperse hematite particles by optical trapping, Shunichi Sato, Yasunori Harada, Yoshio Waseda, Tadao Sugimoto, *Tohoku Univ., Japan.* Micromanipulation of mono-disperse hematite particles in micrometer range is demonstrated by using optical trapping technique indicating the applicability for microstructure fabrication. **(p. 39)**

MThD3 • Nanomachining of silicon by direct laser processing, M. Müllenborn, H. Dirac, J. W. Petersen, *Danmarks Tekniske Univ., Denmark.* A high-resolution laser direct write system has been set up to etch nanostructures into silicon with a line width of less than 150 nm. **(p. 42)**

MThD4 • Step height standards for calibrating an AFM/STM, Jean M. Bennett, *Mount Holyoke College;* Mecky Puiu, *VLSI Standards, Inc.;* Van A. Hodgkin, *U.S. Naval Air Warfare Center;* Thomas McWaid, *NIST–Gaithersburg.* Accuracy of step height standards measured on three different optical profilers is discussed along with possible systematic errors.
(p. 45)

MThD5 • VUV laser (157 nm) chemical vapor deposition of high-quality amorphous hydrogenated silicon: chemical mechanism, H. Karstens, J. Knobloch, A. Winkler, A. Pusel, M. Barth, P. Hess, *Univ. Heidelberg, Germany.* The chemistry-structure-performance relationships are studied by changing the mono- and biradical concentration above the growing surface. A model supports the experimental results. **(p. 46)**

MThD6 • Surface plasmon-enhanced Raman scattering at gratings: optimization and stimulated regime, I. Baltog, N. Primeau, R. Reinisch, *Unité de Recherche Associée, France;* J. L. Coutaz, *Univ. Savoie, France.* We show that the enhancement of Raman scattering induced by surface plasmons at a coated grating can be optimized leading to a measured enhancement of 10^5 and to a stimulated process for values as low as 40 mW pump power and 50-Å thick overcoating layer. **(p. 49)**

MThD7 • Z-scan measurements of porous silicon particles in a colloidal suspension, S. S. Choi, M. A. Fiddy *Univ. Massachusetts.* Z-scan measurements of the third order nonlinear optical susceptibility of different concentrations of porous silicon particles in a colloidal suspension are reported. **(p. 52)**

ZIA B & C

8:30am–10:00am
MFA • Laser and Optical Surface Analysis
Richard M. Osgood, Jr., *Columbia University, Presider*

8:30am (Invited)
MFA1 • Optical diagnostics during film processing of micro- and nanostructures, Irving P. Herman, *Columbia Univ.* An overview of the use of optical spectroscopies for real-time *in situ* diagnostics during the fabrication of very small structures is presented, emphasizing the probing of submonolayer films and temperature. **(p. 56)**

9:00am
MFA2 • Profiling and light scattering studies of Si surfaces, E. L. Church, P. Z. Takacs, *Brookhaven National Laboratory;* J. C. Stover, *TMA Technologies, Inc.* The microroughness of silicon-wafer surfaces are shown to be fractal-like over a wide range of spatial wavelengths. These results are illustrated and discussed. **(p. 58)**

9:15am (Invited)
MFA3 • Laser diagnostics of film properties by coherent surface wave pulses, Peter Hess, *Univ. Heidelberg, Germany.* Surface acoustic wave spectroscopy by interference of broadband coherent wave pulses in layered structures is discussed. The determination of mechanical and elastic film properties is demonstrated. **(p. 60)**

9:45am
MFA4 • Analysis of surface roughness of silicon surfaces by reflection electron energy loss spectroscopy, H. N. Frase, S. S. Wong, C. C. Ahn, H. A. Atwater, *California Institute of Technology.* Reflection electron energy loss spectroscopy low-loss inelastic electron scattering spectra are correlated with surface roughness, ranging from the monolayer to micron scale on Si surfaces. **(p. 63)**

ANASAZI FOYER

10:00am–10:30am
Coffee Break

ZIA B & C

10:30am–12:00m
MFB • Laser Surface Processing and Atomic Scale Analysis
Richard Hall, *Exxon Corporation, Presider*

10:30am (Invited)
MFB1 • Sub-monolayer ablation of II–VI semiconductor surfaces, Peter D. Brewer, J. J. Zinck, G. L. Olson, *Hughes Research Laboratories;* M. Stuke, *Max-Planck Institut für biophysikalische Chemie, Germany.* This paper examines the excimer laser ablation of II–VI semiconductors and the accompanying fluence-dependent, reversible modifications to surface composition and structure. **(p. 68)**

11:00am
MFB2 • Surface preparation and photochemistry of CdTe(110), P. J. Lasky, P. H. Lu, Y. Luo, R. M. Osgood, Jr., D. A. Slater, *Columbia Univ.* We describe studies of ECR plasma-based processing of CdTe(110) surfaces and TOF mass spectroscopic studies of the photochemical dynamics of adsorbed $(CH_3)_2Cd$. **(p. 71)**

11:15am (Invited)
MFB3 • Real-time monitoring of surface reactions during plasma processing, Masataka Hirose, Yastoshi Miyoshi, Seiichi Miyazaki, *Hiroshima Univ, Japan.* Chemical bonds on growing film surfaces in silane-based plasma have been sensitively probed by real-time attenuated total reflection spectroscopy. **(p. 74)**

11:45am
MFB4 • Atomic layer growth of SiO$_2$ on Si(100) using SiCl$_4$ and H$_2$O in a binary reaction sequence, Ofer Sneh, Michael L. Wise, Steven M. George, *Univ. Colorado.* A binary reaction sequence for the atomic layer controlled deposition of SiO_2 on Si(100) was demonstrated using $SiCl_4$ and H_2O. **(p. 77)**

12:00m–6:00pm
Afternoon Free

6:00pm–7:30pm
Conference Reception

ZIA B & C

8:30am–10:00am
MSaA • Optical and Electronic Properties of Nanostructures
Harry Atwater, *California Institute of Technology, Presider*

8:30am (Invited)
MSaA1 • Optical properties of silicon nanoclusters, Louis E. Brus, *AT&T Bell Laboratories.* Abstract not available at time of printing. **(p. 82)**

9:00am
MSaA2 • Silicon solid-state LED: long-lived visible electroluminescence from silicon nanocrystallites, T. A. Burr, K. D. Kolenbrander, *Massachusetts Institute of Technology.* A solid-state light-emitting device employing the electroluminescence of well-passivated silicon nanocrystallites to produce long-lived visible (orange-yellow) light at room temperature has been constructed and characterized. **(p. 83)**

9:15am (Invited)
MSaA3 • STM imaging of electron scattering and confinement at metal surfaces, Phaedon Avouris, *IBM T. J. Watson Research Center.* We studied the scattering of metal surface-state electrons by individual steps and adsorbates. We found that we can confine these electrons in low-dimensionality structures. **(p. 86)**

9:45am
MSaA4 • Single nanocrystal spectroscopy by two-photon excitation, Sean A. Blanton, Ahmad Dehestani, Peter C. Lin, Philippe Guyot-Sionnest, *Univ. Chicago.* We use a two-photon microscopy technique to obtain low-temperature excitation and fluorescence spectra of single semiconductor nanocrystals in an amorphous host. **(p. 87)**

ANASAZI FOYER

10:00am–10:30am
Coffee Break

ZIA B & C

10:30am–12:00m
MSaB • Electronic Structure and Light Emission from Nanostructures
Masataka Hirose, *Hiroshima University, Japan, Presider*

10:30am (Invited)
MSaB1 • Obtaining bulk electronic structure with atomic resolution using spatially resolved electron energy loss spectroscopy, P. E. Batson, *IBM T. J. Watson Research Center.* Conduction band edges in Ge-Si alloys have been obtained from the silicon 2p core absorption spectra. Results are then compared with expectations based on measured atomic compositions. **(p. 92)**

11:00am (Invited)
MSaB2 • Fabrication and properties of ultrathin films of porous silicon, P. M. Fauchet, *Univ. Rochester.* We report the fabrication, optical and structural characterization, and scientific and device applications of high-quality, free-standing, ultrathin porous silicon films. **(p. 95)**

11:30am
MSaB3 • Photoluminescence and electroluminescence of Ge-implanted $Si/SiO_2/Si$ structures, K. V. Shcheglov, C. M. Yang, H. A. Atwater, *California Institute of Technology.* Germanium nanocrystal-based electroluminescent device has been fabricated using conventional VLSI processing. Structural characterization, photoluminescence and electroluminescence spectra and luminescence mechanisms will be discussed. **(p. 98)**

11:45am
MSaB4 • Correlation of size and photoluminescence for Ge nanocrystals in SiO_2 Matrices, C. M. Yang, K. V. Shcheglor, K. J. Vahala, H. A. Atwater, *California Institute of Technology.* Germanium nanocrystal size distributions obtained from electron microscopy data were used in conuunction with an exciton recombination model to compare predicted and measured photoluminescence spectra. **(p. 101)**

ZIA B & C

12:00m–12:10pm
Closing Remarks
Steven M. George, *University of Colorado, Chair*

Surface Analysis and Morphology During Processing

MThA 8:30 am-10:00 am
Zia B & C

Phaedon Avouris, *Presider*
IBM T.J. Watson Research Center

STM Characterization of Surface Processing: Semiconductor Etching, J.H. Weaver, University of Minnesota, Department of Materials Science & Chemical Engineering, 421 Washington Avenue SE, Minneapolis, MN 55455; Phone: 612-625-6548; Fax: 612-625-6043

Advanced material manufacturing often involves dry chemical etching. Most dry etching processes are done under nonequilibrium conditions at elevated temperature during irradiation by photons, electrons, and ions. While such processes are critical to semiconductor technologies, they are poorly understood -- a limitation that is easily rationalized since processing parameters are interrelated. This presentation will review recent investigations of the role of a subset of the processing parameters by focusing on etching of Si(100)-2×1 and GaAs(110) using halogens.

In our work, we prepare atomically clean semiconductor surfaces and expose them at elevated temperature to a predetermined flux and fluence of the etchant gas. Post-exposure characterization is done with atomic-resolution scanning tunneling microscopy and parallel photoemission measurements. With such information, it is possible to assess the importance of steps and defects, to relate known desorption thresholds with specific modes of etching, and to model surface reaction pathways.

Figure 1 shows scanning tunneling microscope images for Si(100)-2×1 at different stages of etching with Br_2. The images were acquired at room temperature after dosing at 900 K. The top image for the clean Si surface shows characteristic straight S_A-type steps and irregular S_B-type steps. Step etching is the dominant mode of material removal at temperatures below about 750 K. This results in step retreat and layer-by-layer etching. On an atomic scale, etching involves preferential dimer removal along the dimer row direction at a step, a pathway that leads to smoothing of irregular S_B-steps. At 900 K, a second channel involving terrace pitting is activated, as identified by the P in the center image. Once formed, the terrace pits can grow and our analysis shows elongation along the dimer row direction. With continued etching, the pits elongate, branch, and ultimately coalesce. Regrowth islands of Si, I, also nucleate on the terrace because etching removes one atom of a dimer as $SiCl_2$ and can leave the second on the surface.

Figure 2 shows that exposure to 2 ma-s of Br_2 at 850-900 K produces a state that would not have been considered unless it had first been observed experimentally. (The fluence represents the amount of Br incident upon the surface. Here, 1.5 ma-s means one Br atom per Si atom under conditions of unity sticking coefficient.) At lower fluence, there has been etching but the amount of Br on the surface is not sufficient to induce a surface phase transformation. When the phase transformation occurs, the 2×1 structure of the surface, corresponding to one Br atom bonded to each Si atom, transforms to a 3×1 structure. The structure sketched at the bottom of the figure shows a row of Si atoms with two-fold bonding to Br ($SiBr_2$-like units) alternating between dimer rows with single bonding to Br. This results in the removal of $SiBr_2$ units to produce the patterned surface shown in Fig. 2. We emphasize that this can only be induced at high temperature after a threshold fluence and that this is the dominant etching mechanism in steady state etching.

The removal of a silicon dimer from a (100) terrace produces structures with local geometries very much like those found at steps. Etching from these initiation sites is analogous to that from steps, with preferential etching along the dimer row direction. Linear growth of a pit along the dimer row direction produces a double vacancy VV elongated along an S_A-type step edge. Production of a double vacancy along the other direction represents branching. The growth of pits during etching reveals competition between linear and branched growth. Detailed analysis of the number densities for pits of different sizes and shapes makes it possible to deduce rate constants and energy differences associated with the reaction pathways, as will be discussed. Such atomic-scale analysis and modeling of etching establishes protocols that should be applicable to a wide range of systems.
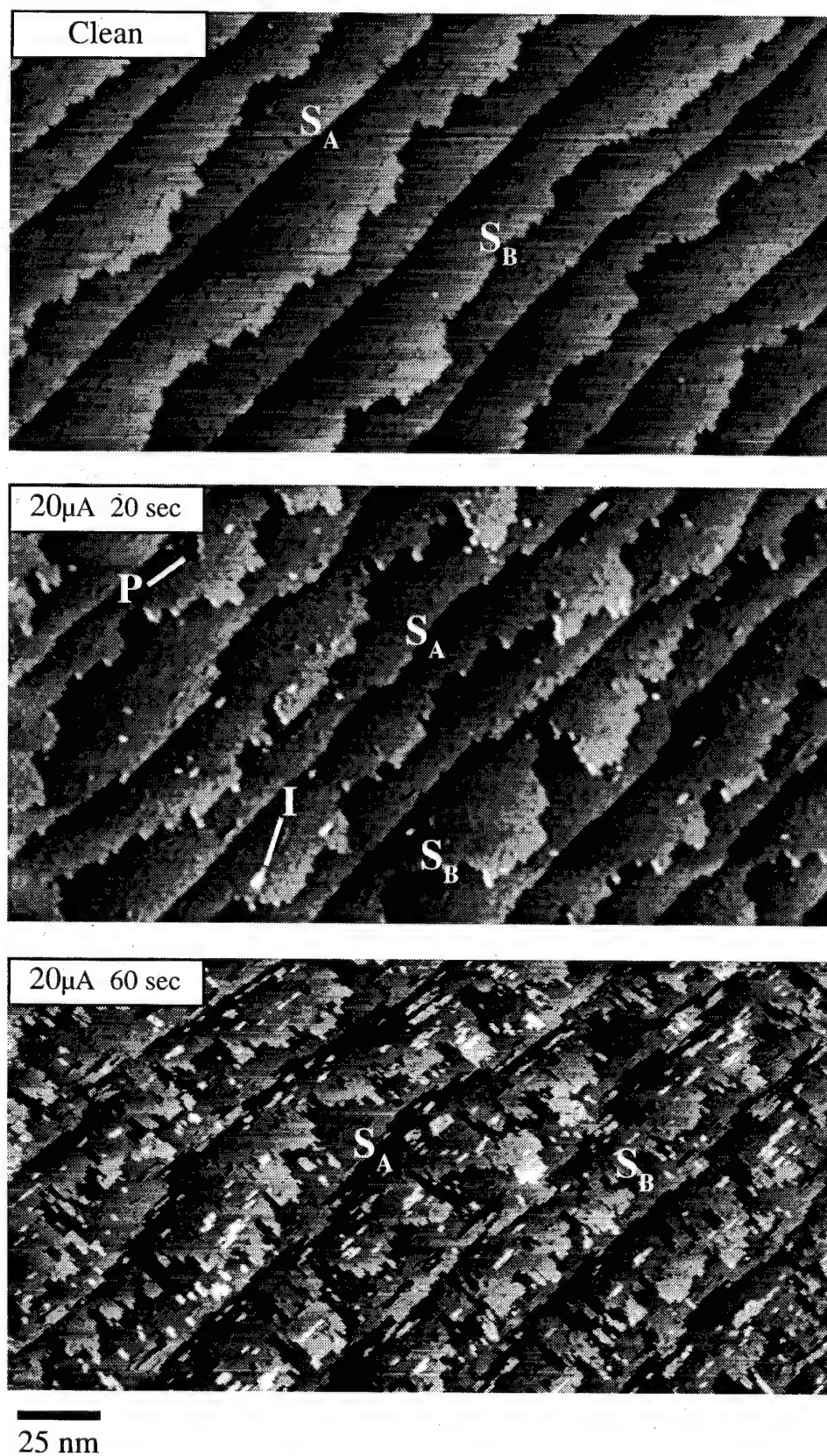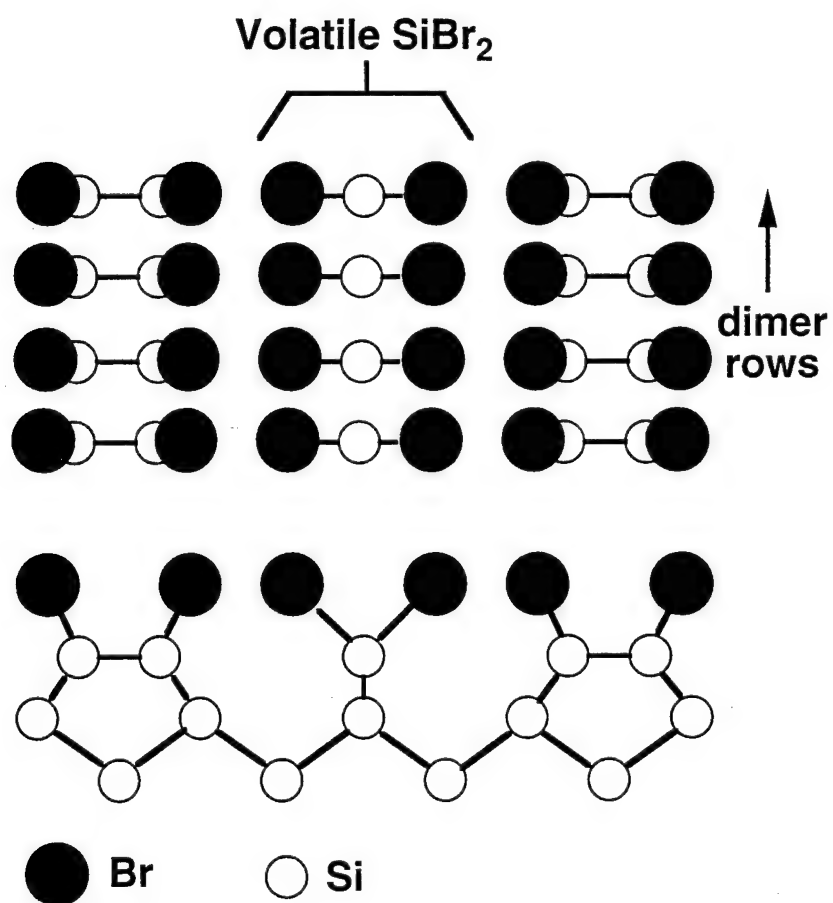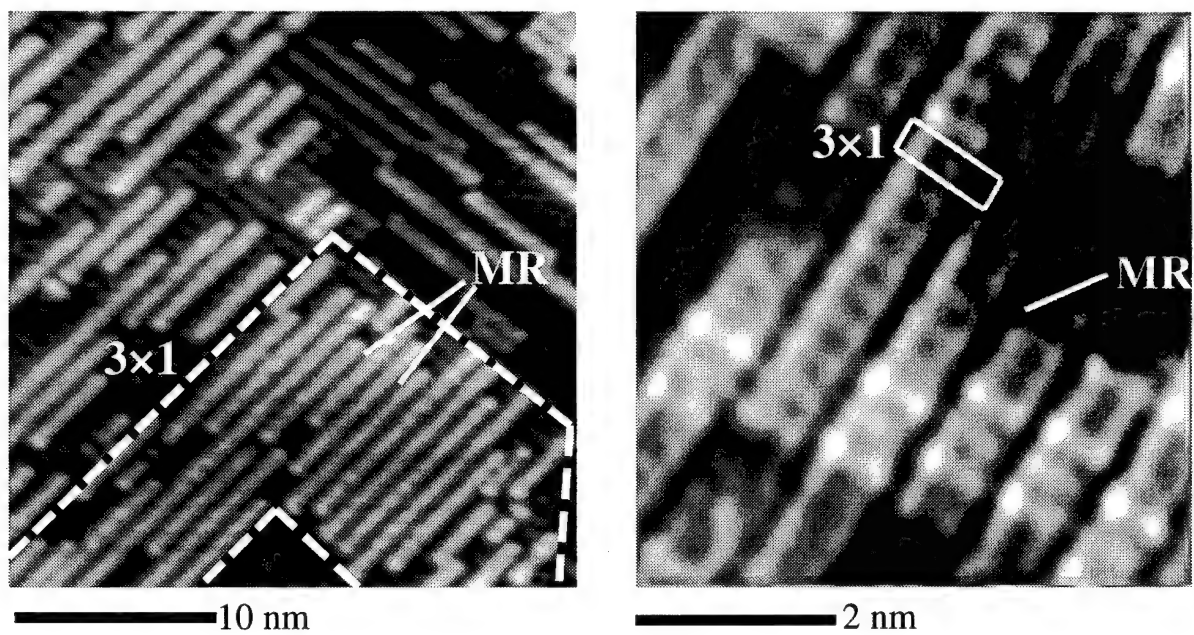
FIG. 1

FIG. 2

Abstractive vs. Dissociative Chemisorption of Molecular Halogens on the Si(111)-7x7 Surface: A Molecular Beam/STM Study.

J.A. Jensen, C. Yan, E.R. Behringer, A.C. Kummel,
U.C. San Diego Chemistry, La Jolla, CA 92093
Phone: 619/ 534-7826
FAX: 619/ 534-2063

The chemisorption of a mono-energetic molecular beams of F_2, Cl_2, and Br_2 onto a room temperature Si(111)-7x7 surface are examined using scanning tunneling microscopy and the resulting adsorbate structures are studied as a function of translational energy/chemisorption mechanism. For F_2 chemisorption on Si(111)-7x7, there is no intrinsic physisorption state and therefore no island formation at low incident translational energy[1]. Instead at low translational energy (0.03eV), we observe that the dominant adsorption sites are single reacted adatoms (Si-F), while at higher translational energy (0.27eV) dimers/neighboring pairs of reacted adatoms are commonly observed. From previous work by the Ceyer[2] and Carter[3] groups, it is known that at low translational energy, F_2 can adsorb via abstraction (F_2 collides, one F atom chemisorbs, the other is ejected into the gas phase), while at higher translational energies, dissociative chemisorption becomes the predominant adsorption mechanism. Our STM experiments, in conjunction with a simple Monte Carlo model, show that at low translational energy, the abstraction mechanism accounts for nearly all chemisorption of F_2 because nearly all adsorption sites are single reacted adatoms. At higher translational energy, the dissociative chemisorption mechanism becomes important and the predominance for single site adsorption is greatly reduced while the occurrence of dimers/pairs of reacted adatoms is increased.

Comparisons are made to the direct chemisorption of Cl_2 and Br_2 onto the Si(111)-7x7. Because of the higher masses, a molecular beam of higher halogen translational energy can be prepared. Abstraction was observed (single site adsorption) for both Cl_2 and Br_2 on the Si(111)-7x7 surface, but at a much lower level relative to the total adsorption probability. Examination of the level of abstraction for all three halogens at various translational energies reveals that the probability for abstraction (relative to the total adsorption) scales linearly with the momentum of the incident molecule.

References:

(1) C. Yan, J.A. Jensen, A.C. Kummel, "Large Island Formation versus Single-Site Adsorption for Cl_2 Chemisorption onto Si(111)-7x7 Surfaces", *Phys. Rev. Lett* **72**, 4017 (1994).

(2) Y.L. Li, D.P. Pullman, J.J. Yang, A.A. Tsekouras, D.B. Gosalvez, K.B. Laughlin, M.T. Schulberg, D.J. Gladstone, M. McGonigal, S.T. Ceyer, Submitted to *Phys. Rev. Lett.*

(3) L.E. Carter, S. Khodabanedeh, P.C. Weakliem, E.A. Carter, *J. Chem. Phys.* **100**, 2277 (1994).

STM Measurements of the Interaction of Vacancies with Steps During Low-Energy Sputtering of Si(001)*

B. S. Swartzentruber[1], C. M. Matzke[2], D. L. Kendall[2], and J. E. Houston[1]

[1]*Sandia National Laboratories, Albuquerque, NM 87185-0344*

[2]*Center for High Technology Materials, University of New Mexico, Albuquerque, NM 87131*

Spurred by the desire to control the pre-growth substrate morphology as well as the quality of epitaxial thin films several groups have investigated the effects of low-energy ion beam sputtering on the Si(001) surface morphology and growth kinetics. [1] To first order, low-energy sputtering can be understood as introducing surface vacancies which diffuse across terraces and annihilate at step edges and with adatoms. [2] The introduction of vacancy formation and diffusion as additional kinetic processes controlling surface morphology has led to interesting phenomenology, and the metaphor of vacancies as "anti-atoms" on the silicon surface is rather striking. For example, just as Si can be grown epitaxially on the Si(001) surface in a layer-by-layer growth mode, low-energy ion bombardment can result in the layer-by-layer removal of the surface atoms. [2]

Rows of neighboring atoms on the Si(001) surface dimerize to form a surface reconstruction with 2×1 periodicity. Because of this symmetry there are two types of steps on the surface. A step that terminates at the side of an upper terrace dimer row is called SA and a step that terminates at the end of an upper terrace dimer row is called SB. Surfaces slightly miscut from the [001] direction toward [110] are comprised of a staircase of alternating rough and smooth steps with alternating domains of 2×1 and 1×2 periodicity. The rough steps have SB segments parallel to the nominal step direction and contain kinks of the SA type, while the smooth steps have SA segments parallel to the step direction and contain kinks of the SB type.

Analogous to adatoms, surface vacancy kinetics are anisotropic. Like adatoms, the diffusion of vacancies parallel to the dimer rows is greater than perpendicular to the dimer rows, [3-5] and vacancies also preferentially annihilate at the ends of the dimer rows. [6] Under appropriate conditions, by adding vacancies to the surface one can make the rough steps retract with respect to their smooth neighbors forming a majority domain 1×2 surface. [6]

In the present work, we create mobile surface vacancies on a stepped Si(001) surface by sputtering with low-energy (300 eV) Xe ions in a temperature regime where the vacancies can diffuse to and annihilate at the steps without a significant probability of forming vacancy islands on the terraces. During the first 5 minutes of sputtering, Fig. 1a, the vacancies preferentially

annihilate at the rough step causing it to retract, and the majority domain population reaches ~77%. At twice the dose, Fig. 1b, the majority domain population is only slightly greater, ~80%, although twice as many atoms have been removed. Doubling the dose again, Fig. 1c, does not affect the majority domain population, indicating that the step configuration has reached steady-state. Additional removal of surface atoms results in step flow whereby the rough and smooth steps retract at the same rate. If the process of surface atom removal is

Figure 1: STM images of low-energy ion bombarded Si(001) as a function of dose. a) 5 min. b) 10 min. c) 20 min. d) post-annealed surface.

shut off and the temperature of the sample is held at 465 C, then the step configuration returns to one that contains equal domain populations, as seen in Fig. 1d.

The equilibrium, *i.e.*, minimum free energy, step configuration is one in which the steps are equally spaced. Because the 2×1 surface reconstruction has an anisotropic surface stress, alternating domains are in compression and tension. This sets up a long-range stress field that extend into the bulk, the energy of which is minimized by a configuration with equal domain populations — in this case a staircase of equally spaced steps. [7] The stress energy can be viewed as an
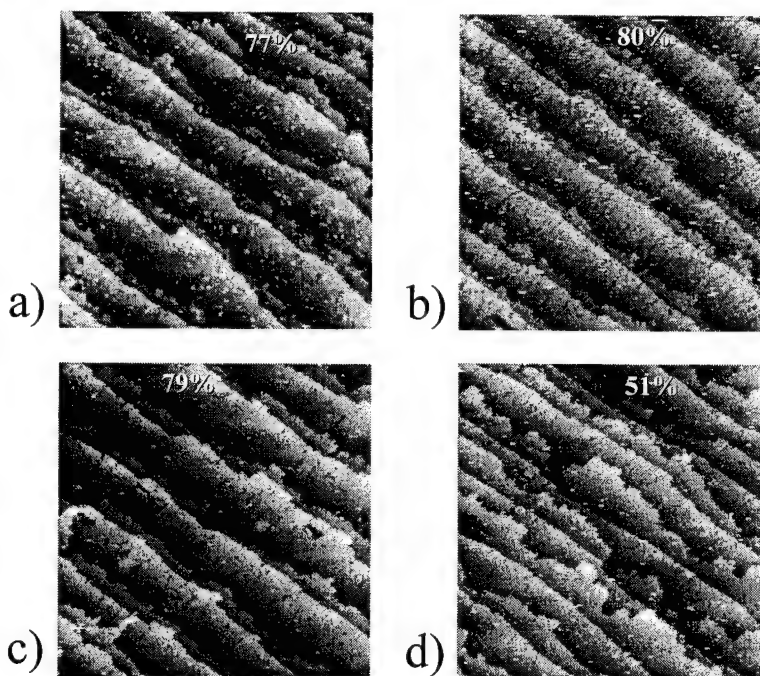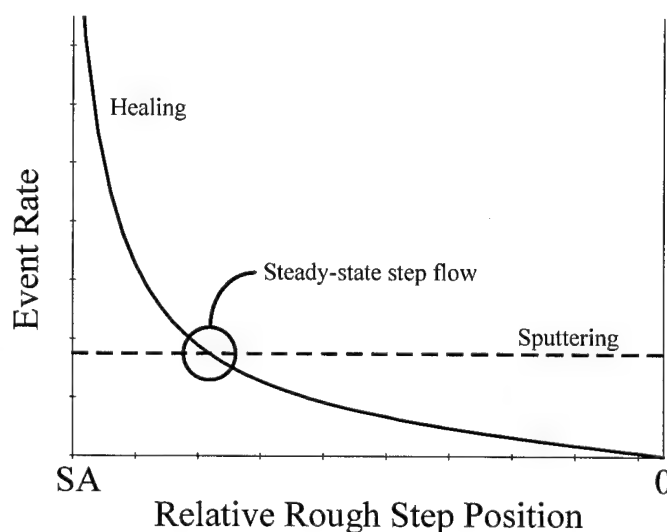

Figure 2: The step configuration reaches steady state when the step-retraction rate due to sputtering is balanced by the step-advancing rate due to the healing process.

indirect repulsive step-step interaction.

The vacancy annihilation events retract the steps. Since the sticking coefficient of the vacancies is greater at the rough step than at the smooth step, the rough steps retract faster and the step configuration moves away from the equilibrium configuration of equally spaced steps. We show this effective retraction rate as the horizontal dashed line in Fig. 2. The vacancy-induced retraction rate is constant while the healing rate increases as the step configuration gets further from equilibrium; therefore, there exists a steady-state configuration in which these two competing rates balance and the relative position of the rough step between its smooth neighbors remains constant. At steady state, the removal of surface atoms through the sputtering process is manifest as simple step flow wherein the rough and smooth steps retract at the same rate maintaining their relative positions.

[1] J. Greene, S. Barnett, J. Sundgren, and A. Rockett, in *Ion Beam Assisted Film Growth*, edited by T. Itoh (Elsevier, Amsterdam, 1989). p. 101.
J. Y. Tsao, E. Chason, K. Horn, D. Brice, and S. T. Picraux, Nucl. Instrum. Methods Phys. Res., Sect. B **39**, 72 (1989).

[2] P. Bedrossian, J. E. Houston, J. Y. Tsao, E. Chason, and S. T. Picraux, Phys. Rev. Lett. **67**, 124 (1991).

[3] N. Kitamura, B. S. Swartzentruber, M. G. Lagally, and M. B. Webb, Phys. Rev. B, **48**, 5604 (1993).

[4] N. Kitamura, M. G. Lagally, and M. B. Webb, Phys. Rev. Lett. **71**, 2082 (1993).

[5] B. S. Swartzentruber and M. Schacht, Surf. Sci. (in press).

[6] P. Bedrossian and T. Klitsner, Phys. Rev. Lett. **68**, 646 (1992).

[7] O. L. Alerhand, D. Vanderbilt, R. D. Meade, and J. D. Joannopoulos, Phys. Rev. Lett. **61**, 1973 (1988).

Morphology Evolution and Ion-Induced Surface Transport During Sputtering

T.M. Mayer, E. Chason, B.K. Kellerman, A.J. Howard
Sandia National Laboratories
Albuquerque, NM 87185

We have investigated the evolution of nanometer-scale surface morphology on crystalline and amorphous substrates during off-normal, heavy and light ion sputtering. We use *in-situ* X-ray reflectivity to measure kinetics of surface morphology evolution and atomic force microscopy to obtain three dimensional structure of sputtered surfaces. Roughening processes associated with material removal and smoothing processes associated with ion-induced surface transport are combined into a comprehensive kinetic model of surface morphology development.

Sputtering of SiO_2 surfaces by heavy ions (Xe, 1 keV) at off-normal incidence leads to roughening of the surface with development of a highly coherent ripple pattern. The ripples have a period of approx. 30 nm, with wavevector oriented parallel to the direction of the incident ion. The magnitude of the surface roughness increases exponentially with ion fluence. Irradiation of the roughened surface with H or He ions leads to smoothing with an exponential decay of the surface roughness with fluence. Similar behavior is observed on Ge surfaces sputtered by Xe, however the degree of roughening is temperature and surface structure (crystalline vs. amorphous) dependent.

Bradley and Harper (1) have proposed that ripple formation and exponential roughening kinetics are due to a curvature dependence to the sputter yield, which causes troughs to etch faster than crests, and leads to exponential growth of all spatial frequencies in the surface roughness spectrum. High spatial frequency features are proposed to relax by surface diffusion, giving a maximum in the growth rate for a narrow range of spatial frequencies, and hence ripple formation. We find that in addition to surface diffusion, amorphous materials can relax by viscous flow. The roughening and smoothing processes have different dependencies on the spatial frequency of the surface features, such that the amplitude of a particular Fourier component with frequency, q, is given by:

$$|h(q,t)|^2 = h_0(q)^2 \exp(R(q)t)$$

where

$$R(q) = Sq^2 - Fq - Dq^4$$

S is the curvature dependent sputter yield, F is the viscous relaxation rate, and D is the relaxation rate by surface diffusion. In the absence of viscous relaxation (crystalline surfaces) there will be a maximum in the growth rate, corresponding to the ripple frequency. If viscous relaxation is possible (amorphous surfaces) the rate can be negative at all frequencies and surfaces will smoothen in exponential fashion.

Using this model combined with a stochastic roughening term to account for the shot noise in the ion flux, we have quantitatively analyzed the roughening and smoothing behavior of SiO_2 and Ge surfaces. Calculations of the sputter yield, S, using the formalism of Bradley and Harper and ion scattering parameters obtained from TRIM computations give semi-quantitative agreement with the experiments on SiO_2 but agree less well with Ge sputtering. The viscous relaxation rate of SiO_2 is obtained directly from the smoothing behavior. We find the viscosity to be very dependent on the ion energy, but not on temperature. Ion induced surface and bulk relaxation measurements both suggest a defect mediated relaxation mechanism, in which transient defects produced by ion bombardment cause viscous relaxation in competition with a second order annihilation process. The ion-induced surface diffusion rate on SiO_2 is inferred from the observed frequency of the ripple pattern produced by Xe bombardment.

The temperature dependent phenomena observed on Ge surfaces are a reflection of the different transport processes available. At low temperature (<150° C) the surface becomes amorphous during sputtering. Ion-induced viscous relaxation competes effectively with roughening, and the surface roughens only slightly to a steady state value. Above 150° C the surface remains crystalline and exponential roughening is observed. Thermally induced smoothing by surface diffusion now competes with roughening, such that the roughening rate decreases as temperature increases. The activation energy for surface diffusion on Ge is estimated to be 0.4 eV, which is consistent with previous measurements.

1. R. M. Bradley, J. M. E. Harper, J. Vac. Sci. Technol. A **6**, 2390 (1988).

Development of Surface Morphology During the Initial Stages of CVD Growth

D.P. Adams, T.M. Mayer and B.S. Swartzentruber

Sandia National Laboratories, Albuquerque, N.M. 87185

We present an investigation of the initial stages of Fe layer growth by thermal decomposition of $Fe(CO)_5$ on Si(100) substrates. Scanning tunneling microscopy has been employed to study the evolution of film morphology. Specifically, this investigation has determined the scaling behavior of average cluster density and cluster size distributions for growth over a range of substrate temperatures (100 - 215°C) and coverages. In general, clusters are found to nucleate on Si terraces showing no preference for dissociation of precursor molecules at Si steps. (See Fig. 1)   Fig. 2 shows a plot of average island number / area (and areal coverage) vs. exposure for samples dosed with 1×10^{-8} Torr of $Fe(CO)_5$ at several different temperatures. Fig. 3 shows the corresponding island size distributions for growth at 165°C. By comparing the morphology of submonolayer films measured by STM to that predicted by a rate equation analysis and kinetic Monte Carlo calculations, we have monitored the relative roles of various kinetic processes on changing layer morphology.   The nucleation model that will be presented accounts for various processes occuring during CVD growth including formation of nuclei on the Si starting surface and decomposition of the precursor molecule on pre-existing clusters (either by diffusing to a cluster or by direct impingement from the gas phase) and therefore should accurately predict the evolution of layer morphology for other systems. We have also begun to investigate the influence of surface chemistry on nucleation. Preliminary work involving passivating the Si surface prior to CVD growth will be presented.
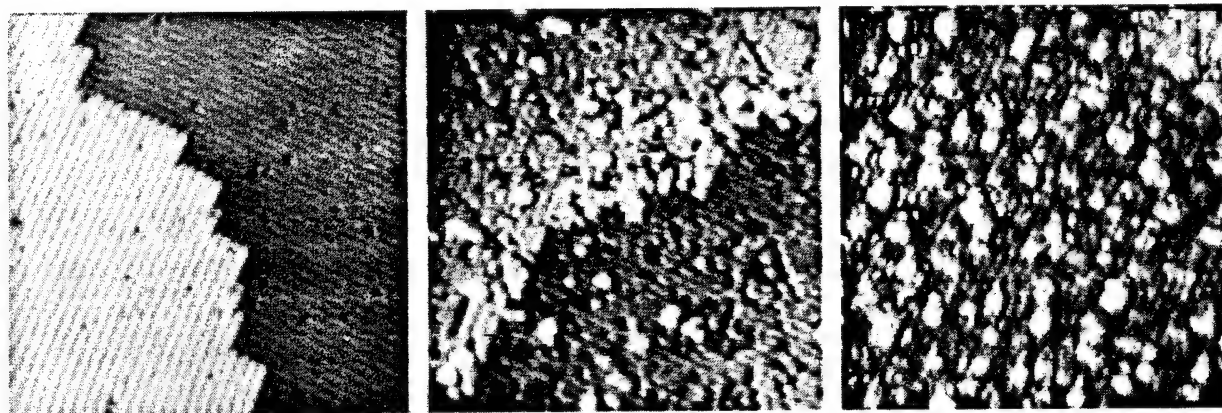
Fig. 1 Scanning tunneling microscope images of a clean, Si(100) surface and after dosing with 1.0 and 5.0L of Fe(CO)$_5$ at 165°C. (V = - 2.5V)

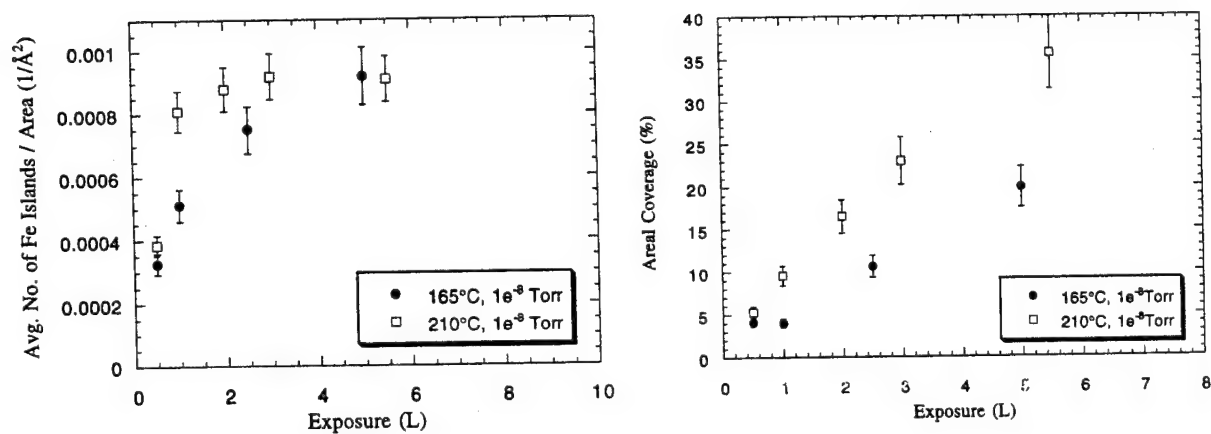Fig. 2 Average island number / area (and areal coverage) vs. exposure.

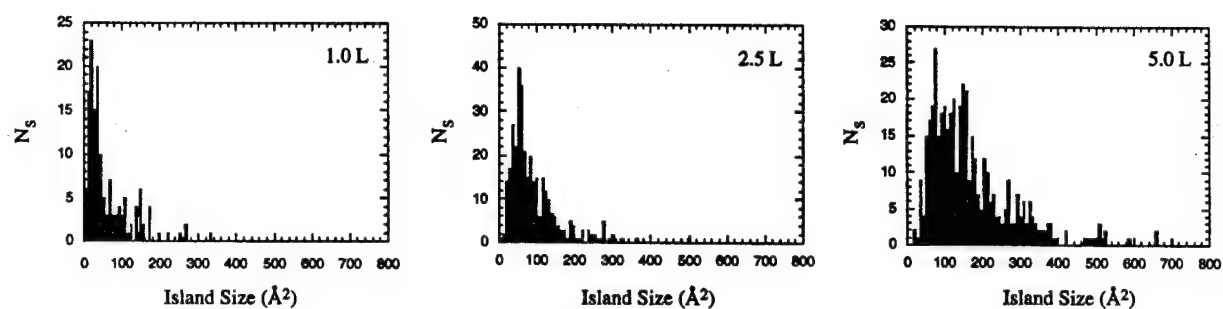Fig. 3   Island size distributions measured by STM for growth at 165°C

Nanostructure Fabrication Techniques

MThB 10:30 am-12:00 m
Zia B & C

Joe Greene, *Presider*
University of Illinois–Urbana

'Electron Beam Nanolithography'

Christie R.K. Marrian
Nanoelectronics Processing Facility, Code 6804
Naval Research Laboratory, Washington DC 20375
Tel: 202-767-3150 Fax: 202-767-4998
e-mail: Christie.Marrian@nrl.navy.mil

Motivated by trends in the microelectronics industry and the quest to investigate electronic and material properties in the quantum effect size regime, there is a strong drive to understand and overcome the limits of the processing required for microfabrication. At the beginning of the next century, the precision required in feature sizes for microelectronics manufacturing is projected to be close to 10 nm, i.e. about 25 atomic diameters. Still smaller feature sizes are needed for nanoelectronic device research. For example, to observe effects such as lateral resonant tunneling and coulomb blockade at close to room temperature, feature sizes below 10 nm are necessary. Central to any fabrication scheme for these dimensions is a lithographic step where a pattern is defined in a radiation sensitive material, commonly called the resist, and then replicated into the substrate to define a structure or device. Due to the availability of equipment and knowledge base, the preferred means for defining the smallest possible structures involves the use of a focused high energy beam of electrons.

Over the years feature sizes down to a few nanometers have been defined in this way. However, many of these nanolithographic demonstrations have proved to be unsuited for the fabrication of actual devices or nanostructures. The reasons for this are typically related to the incompatibility of the materials associated with the particular nano-lithographic process with the other fabrication steps involved or that the process itself is too slow or cumbersome. As a result, most nanolithography is performed with a high resolution polymethylmethacrylate (PMMA) resist and a tightly focused beam of electrons with 50 keV or greater energy. Under these conditions, there is little (if any) process latitude and the resolution and pattern fidelity are limited by proximity effects caused by electron backscattering. The scattering results in exposure of the resist layer over a region which extends many microns from the point of impact of the primary electron beam.

The problem of electron scattering can be overcome by reducing the electron energy to a value close to the threshold energy (a few eV) required for the chemical change associated with the exposure of the resist material. A convenient way to generate such electrons is with a scanning tunneling microscope operated in the field emission regime, i.e. with a tip-sample bias greater than ~4 V. Our initial results with electron beam resist

materials demonstrated that indeed one can observe reduced feature sizes and superior pattern fidelity (i.e. closer resolvable feature placement) with the STM compared to exposure with a 50 keV focused e-beam. In addition, there is a considerably larger process latitude with low voltage exposure which significantly eases the tolerances on resist processing such as bake and development times. However, one is restricted to thin (<75 nm) layers of polymeric resists as they are typically extremely poor conductors. Such thin layers are poor reactive ion etch masks limiting subsequent pattern transfer.

To extend the resolution of this STM (or AFM with conductive tip) based lithography, an ultrathin imaging layer is necessary. An additional requirement is that the thin layer must be able to serve as a template for a subsequent growth or selective deposition process to allow pattern transfer into a material of interest. Self assembly is a technique for depositing such layers. A self assembling monomer comprises of a group which will form a covalent bond with the desired substrate attached to chemical groups which give the substrate surface a particular chemical functionality. For example, monomers containing chlorosilane end groups will form a covalent bond to substrates terminated with hydroxyl groups (or oxygen) and form densely packed homogeneous layers with mono-molecular thickness. In our work to date, we have studied organosilane self assembling materials that contain a ligating functionality which has an affinity for a Pd catalyst. A Ni film can be built up on the catalyzed surface by immersion in an electroless plating bath. Energetic irradiation destroys the affinity of the organosilane for the catalyst, thus preventing build up of the Ni film in the exposed regions of the surface. Low voltage electrons induce the same change in the affinity of ligating groups so a positive tone image of the pattern defined with the STM is replicated in the electroless plated metal film.

Our results can be summarized as follows. The lithographic performance of various self-assembling materials has been analyzed in terms of exposure energy threshold, dose effects, substrate preparation and exposure mechanisms. In a film of an organosilane containing a benzyl chloride group, an exposure threshold close to 4 eV was observed. Films based on a monomer with an organosilane moiety, exhibited a somewhat higher exposure threshold of 8 eV. This can be reduced to about 6 eV when the films are deposited on a Si surface where the native oxide has been removed. However, surface preparation is critical. Very little dependence on feature size with dose and tip-sample current has been found. Studies of the mechanism of exposure of these films to energetic photons, reveal that cleavage of the monomer takes place, resulting in the chemical functionality of the exposed regions being drastically changed.

Feature sizes down to 15 nm have been transferred into the electroless Ni film. This film provides an excellent etch mask to a fluorine based reactive ion etch of several microns. Studies of the latent exposure image using the STM itself to image the exposed regions suggest that the inherent resolution of the process is below 10 nm. The resolution step at present appears related to the catalyst step in the metalization process. Significant progress has been made recently in this regard.

Acknowledgments

Selected Recent References

"Technology of Proximal Probe Lithography", Christie R.K. Marrian ed., Institutes of Advance Optical Technologies, Volume IS10, SPIE Press, Bellingham WA , 1993

"Determination of Acid Diffusion Rate in a Chemically Amplified Resist with Scanning Tunneling Microscope Lithography", F. Keith Perkins, Elizabeth A. Dobisz and Christie R.K. Marrian, Journal of Vacuum Science and Technology B 11, 2597 (1993).

"Low Voltage Electron Beam lithography in Self-Assembled Ultrathin Films with the Scanning Tunneling Microscope", Christie R.K. Marrian, F.. Keith Perkins, Susan L. Brandow, Tim S. Koloski, Elizabeth A. Dobisz, & Jeffrey M. Calvert, Applied Physics Letters 64, 390 (1994).

Low Energy Focused Ion Beam for Nanofabrication

Kenji Gamo
Faculty of Engineering Science and Research Center for Extreme Materials
Osaka University
Toyonaka, Osaka 560, Japan

1. Introduction

Maskless fabrication capability and high current density of focused ion beam provide unique applications for microfabrication technology and various new devices and processing techniques have been developed. This paper will discuss some of the recent developments of focused ion beam techniques including low energy focused ion beam technique and *in situ* fabrication.

2. Performance of FIB

Over the past several years, many FIB systems have been developed and important improvement s have been achieved. Typical FIB systems produce focused ion beams with a diameter of <100nm and a current of several 100pA. The most fine focused beam has a diameter of <10nm. 12nm resist pattern or etched pattern were fabricated by using such fine beams. Figure 1 shows an example of etched pattern with a width less than 100nm.

These structures were fabricated using high energy (30-100keV) beams. However, high energy beams produce damage which should be minimized for nanostructure fabrication. For example, high mobility of $10^6 cm^2/Vs$ of two dimensional electron gas (2DEG) system in GaAs/GaAlAs modulation doped heterostructures decreases by 70% at a dose of $10^{16}/cm^2$ for 20eV Ar. Therefore, it should be important to use low energy beams especially for high mobility 2DEG structure. Recently, low energy FIB systems have been developed by several grope, which uses retarding optics and has expected focused ion beams with a spot size less than 100nm, an energy lower than 100eV and a beam current of 50pA. Figure 2 shows a calculated beam spot size as a function of a beam current. Using low energy FIB system, metal deposition with low damage and selective growth of GaAs has been demonstrated.

3. Nanofabrication

Nanostructures have been fabricated by FIB by utilizing ion beam lithograph, maskless ion implantation, ion induced damage isolation and ion beam induced intermixing at heterostructure interface, etc. In GaAs, ion beam induced damage yields high resistive layer, which can be used to define device patterns by a single scanning of FIB. Many nanostructures including quantum point contacts, quantum wires with and without side gates and single electron tunnel devices.

4. In situ processing

Many new semiconductor devices, particularly those utilizing quantum effects and fabricated in III-V semiconductors, require buried nanostructures with clean interfaces and less process induced

damage. As shown in Fig. 3, *in situ* fabrication system which consists of a low energy focused ion beam (FIB) and a molecular beam epitaxy (MBE) systems combined by UHV tunnel is a promising candidate to realize such nanostructures.

To investigate the importance of low energy beams for reducing residual damage, effect of damage and annealing characteristics in GaAs and GaAs/GaAlAs high electron mobility hetero-structures were investigated by Hall effect and deep level transient spectroscopy (DLTS) measurements. From DLTS measurement it was observed that 100eV Ga FIB irradiation induces 7 different kinds of trap centers at a dose ranging from 1×10^{13} to $5 \times 10^{15}/cm^2$. As shown in Fig. 4 these trap centers are annealed out at temperatures ranging from 400 to 600°C, depending on the irradiation dose. The characteristics are compared with those induced by high energy (150keV) Ga irradiation.

As a possible nanostructure device, which requires *in situ* processing to fabricate, a coupled electron waveguide with a new structure is proposed. The device is a vertically coupled electron waveguide device and is composed of two buried quantum wires or electron waveguides which are fabricated in GaAs/GaAlAs heterostructures using MBE and low energy FIB implantation. The device function is based on tunneling between the coupled electron wave guides which can be controlled by a gate bias voltage. Transport properties of the device such as the transfer length and the transfer coefficient are calculated numerically. It is shown that an electron can be transferred completely from a waveguide to the other one if the structural and material parameter is chosen properly.
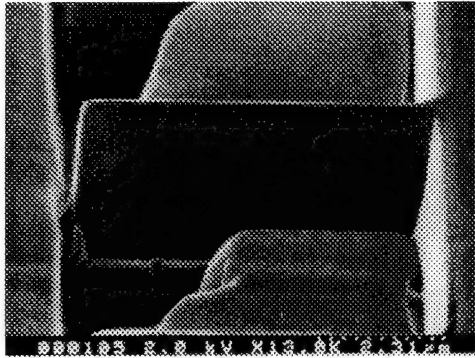

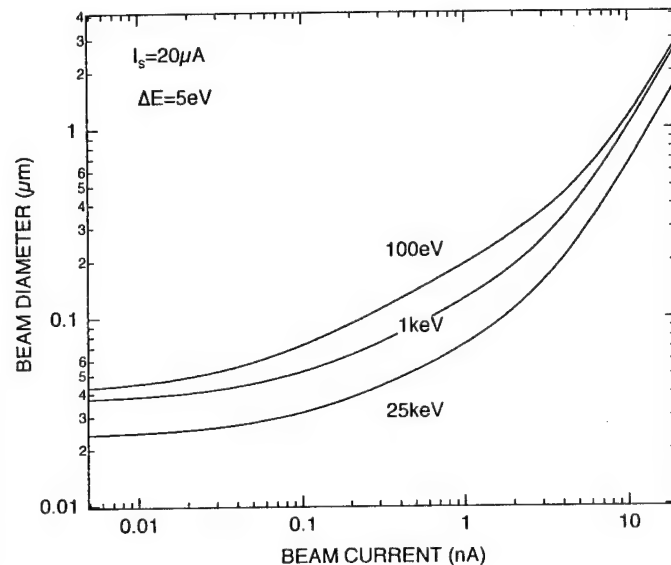Fig. 1 Nanostructures formed by Ga FIB.

Fig. 2 Beam diameter of low energy FIB as a function of a beam current.
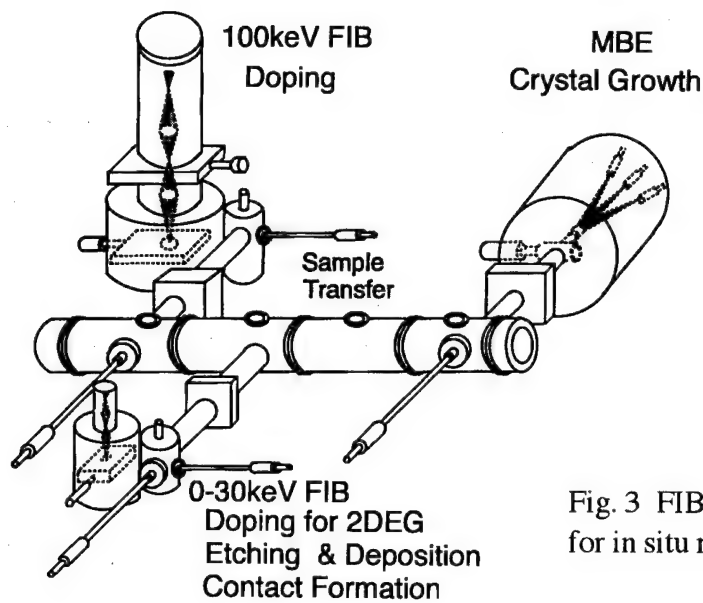
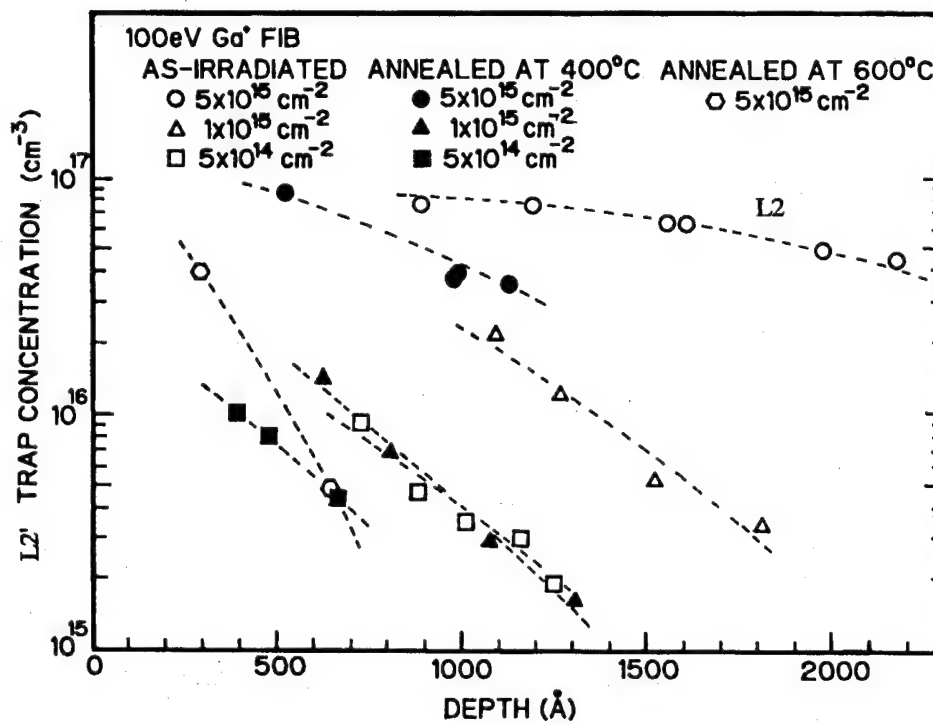Fig. 3 FIB and MBE coupled systems for in situ nanofabrication.

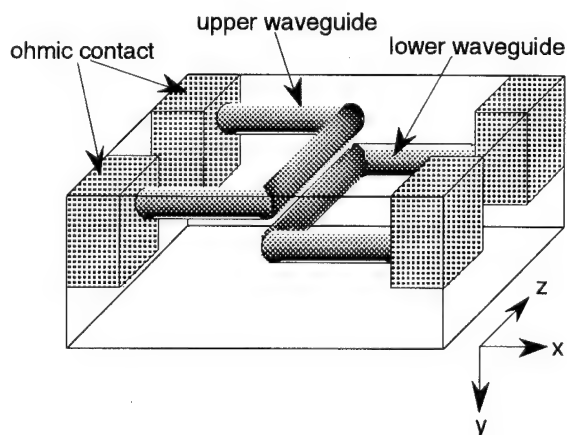Fig. 4 Distribution profiles of electron trap centers formed by 100eV Ga FIB.

Fig. 5 Vertical cooupled waveguide device.

Nanostructure fabrication via atom optics

R. Gupta, J. J. McClelland and R. J. Celotta
Electron Physics Group, National Institute of Standards and Technology
Gaithersburg, MD 20899.

Phone: (301)-975-3768   Fax: (301)-926-2746

As electronic and magnetic devices continue to become smaller, the need for fabricating structures on the nanometer scale grows larger. In lithographic techniques, the fundamental limitation in making nano-scale structures is imposed by diffraction effects which limit the size of the structures to the order of the wavelength of light used. Consequently, technologies are being driven towards using photons of shorter wavelength and/or high energy electrons or ions to produce structures with the highest resolution.

We are currently exploring the techniques of atom optics to fabricate structures on the nanometer scale. Atom optics treats neutral atoms, which can have extremely small de Broglie wavelengths, in an analogous way to light beams or charged particle beams. In atom optics, "optical elements" such as lenses, mirrors and beamsplitters are used to manipulate the atoms' trajectories. Focusing of neutral atoms can be achieved in a number of ways, including passing them through a microfabricated zone plate [1], or subjecting them to the light forces exerted by near-resonant laser light [2]. Optical forces can be either dissipative in nature, in which case they can cool, collimate and/or intensify an atom beam [3], or conservative, in which case they can serve as a lens [4].

In our experiments we use the dissipative spontaneous force to collimate a beam of chromium atoms and the conservative dipole force to focus the atoms into an array of lines as they deposit onto a Si substrate [5]. The dipole force arises from the interaction of the induced dipole in an atom with the gradient in the laser intensity. The intensity variation in the standing wave acts as a series of cylindrical lenses, spaced by $\lambda/2$, which can focus atoms in the nodes (antinodes), when the laser frequency is tuned above (below) the atomic resonance. The first demonstration of laser focused atomic deposition was by Timp *et al.*, using sodium [6].

Figure 1 shows the experimental arrangement consisting of an effusive source of chromium atoms, a pre-collimating aperture, a region of optical collimation and a substrate mounted facing the atomic beam. A single-frequency dye laser provides a few hundred mW of laser light for both the optical collimation and the standing wave. The dye laser is tuned 10 MHz below the atomic resonance to collimate the atom beam and 500 MHz above the atomic resonance for focusing the atoms. The frequency of the dye laser is calibrated against a chromium saturated absorption cell.

Optical collimation of the atom beam is necessary because the final spot size of the focused atoms depends directly on the collimation angle. A pair of counterpropagating laser beams,
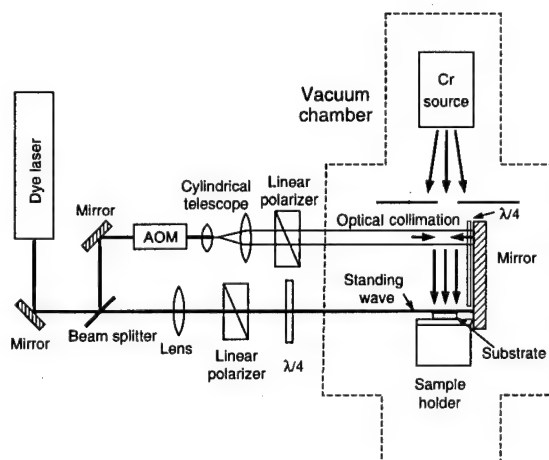

Figure 1. Schematic of laser focused atomic deposition apparatus.

with orthogonal laser polarizations, is used to transversely cool the atoms. With this arrangement, atomic beam collimation of 0.2 mrad can be achieved which is a factor of 10 smaller than the collimation of a typical He-Ne laser beam.

The standing wave laser, with $1/e^2$ diameter 0.4 mm, grazes across the sample so as to generate a half-Gaussian intensity distribution with maximum at the surface of the substrate. Figure 2 shows an atomic force micrograph of a section of the chromium lines created by deposition through the standing wave. The laser wavelength fixes the spacing between the lines at 212.78 nm. Lines extend over the entire region covered by the laser beams. The linewidth is measured to be 65 ± 6 nm and the height of the structures is 34 ± 10 nm.

The linewidth of the structures can be reduced by using an atom optical lens of a shorter focal length. In recent experiments we have succeeded in making lines with a width of 45 nm by using a standing laser with $1/e^2$ diameter of 0.13 mm.
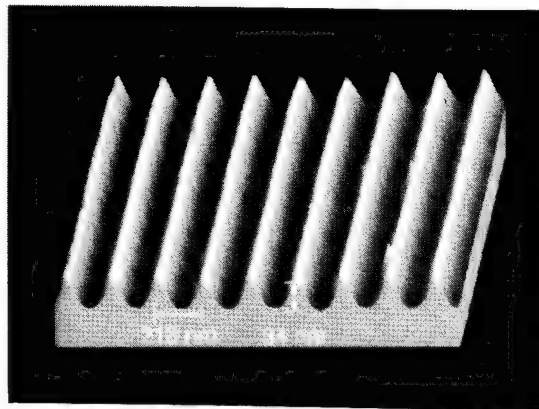
Figure 2. AFM image of Cr lines created by laser focused atomic deposition.

We have also done preliminary experiments to generate two dimensional patterns through the superposition of two standing waves at right angles. Such a configuration produces either an array of crossed perpendicular lines or spots depending on the laser frequency and polarization. In the future, efforts will be made to monochromatize the beam and make other improvements to reduce the linewidth of these structures. With the generation of spots of minimal size the substrate could be translated under the lens to write an arbitrary pattern in a massively parallel manner.

References

1. O. Carnal, M. Sigel, T. Sleator, H. Takuma, and J. Mlynek, Phys. Rev. Lett. **67**, 3231 (1991).
2. V. I. Balykin and V. S. Letokhov, Physics Today **42**, 23 (April 1989).
3. V. I. Balykin, V. S. Letokhov, and A. I. Sidorov, JETP Lett. **40**, 1026 (1985); B. Sheehy, S.-Q. Shang, R. Watts, S. Hatamian, and H. Metcalf, J. Opt. Soc. Am. B **6**, 2165 (1989).
4. J. J. McClelland and M. R. Scheinfein, J. Opt. Soc. Am. B **8**, 1974 (1991).
5. J. J. McClelland, R. E. Scholten, E. C. Palm and R. J. Celotta, Science **262**, 877 (1993).
6. G. Timp, R. E. Behringer, D. M. Tennant, J. E. Cunningham, M. Prentiss, and K. K. Berggren, Phys. Rev. Lett. **69**, 1636 (1992).

Surface Chemistry for Atomic Layer Control

MThC 7:00 pm-8:00 pm
Zia B & C

Steven M. George, *Presider*
University of Colorado

Surface Chemistry of GaAs Atomic Layer Epitaxy

J. R Creighton and C. M. Truong
Org. 1126, MS 0601
P.O. Box 5800
Sandia National Laboratories
Albuquerque, NM 87185-0601

Atomic layer epitaxy (ALE) is a technique which, in principle, yields unparalleled deposition uniformity with precise (i.e. monolayer) thickness control. The technique has been used to deposit compound semiconductors, e.g. GaAs, although the success has not been universally good. In many examples the ALE operating "window" is very small or non-existent. Unintentional carbon doping is another problem which has limited the utility of this technique. In order to address the problems limiting GaAs ALE, we have investigated the surface chemical properties of the standard deposition precursors on GaAs(100) using a variety of surface science diagnostics. Results of these experiments have shed light on the mechanisms of precursor decomposition which lead to film growth and carbon doping. For instance, the kinetics of trimethylgallium (TMGa) decomposition on the Ga-rich and As-rich surfaces, measured by TPD, are in semiquantitative agreement with ALE results. This indicates that the dominant growth mechanism during ALE is heterogeneous in nature. We have also investigated the mechanism of carbon incorporation when using TMGa. Normally, a small fraction of adsorbed methyl (CH_3) groups dehydrogenate into methylene (CH_2) groups, which are a likely precursor to carbon incorporation. This adsorbate was characterized with vibrational spectroscopies and static SIMS. The rate of CH_3 dehydrogenation is consistent with the carbon doping levels obtained during ALE and MOMBE.

We have focused recent efforts towards elucidating the structure of the adsorbate covered GaAs(100) surfaces using LEED and multiple internal reflection infrared spectroscopy (MIRIRS). By examining the polarization and azimuthal dependence of the adsorbate vibrational modes, it is sometimes possible to determine the bonding geometry of the adsorbate with respect to the surface. Reaction of trimethylgallium (TMGa) with the GaAs(100) surface at 300-400°C creates an ordered CH_3 adlayer that exhibits a (1 X 2) LEED pattern. We refer to this surface condition as the monomethylgallium (MMGa) state. At typical GaAs ALE conditions the GaAs surface

should exist in the MMGa state at the end of the TMGa exposure cycle. The CH_3 adsorbate in the MMGa state exhibits relatively sharp (FWHM < 10 cm^{-1}) vibrational modes at 1191 and 2889 cm^{-1}, corresponding to the symmetric C-H bending (δ_s) and stretching modes (ν_s), respectively (see figure). Polarization experiments indicate that the carbon-surface bond lies exclusively in the [-1,1,0] plane, demonstrating that the CH_3 adsorbate is bonded to surface gallium (rather than arsenic) atoms. The Ga-CH_3 bond is tilted away from the surface normal by 50 ± 10°, in good agreement with the expected bond angle for a tetrahedral geometry. Using these results we propose a structure of the (1 X 2) CH_3-covered surface that consists of 1/2 ML of CH_3 groups bonded to a complete monolayer of Ga atoms. The proposed structure is consistent with the CH_3 bond orientation obtained by MIRIRS, the observed LEED pattern, and the electron counting scheme for compound semiconductors. Also, since the structure contains a complete monolayer of Ga atoms (in contrast to the adsorbate-free GaAs reconstructions) it resolves the stoichiometry question of how GaAs ALE yields 1 ML deposition per cycle.

In order to explain the large crystallographic dependence exhibited for GaAs ALE, we have recently investigated the chemisorption properties of TMGa and arsine on GaAs (111) and (110). The behavior of TMGa on GaAs(111)A is similar to the behavior on the (100) surface. Both the (100) and (111)A surfaces reconstruct to create a sizable number of atom vacancies, and both surface easily decompose TMGa irreversibly. However, the (110) surface is stoichiometric (i.e. no vacancies) and TMGa chemisorption on this surface is reversible. These results shed light on how the GaAs surface structure determines the reactivity towards organometallic compounds.
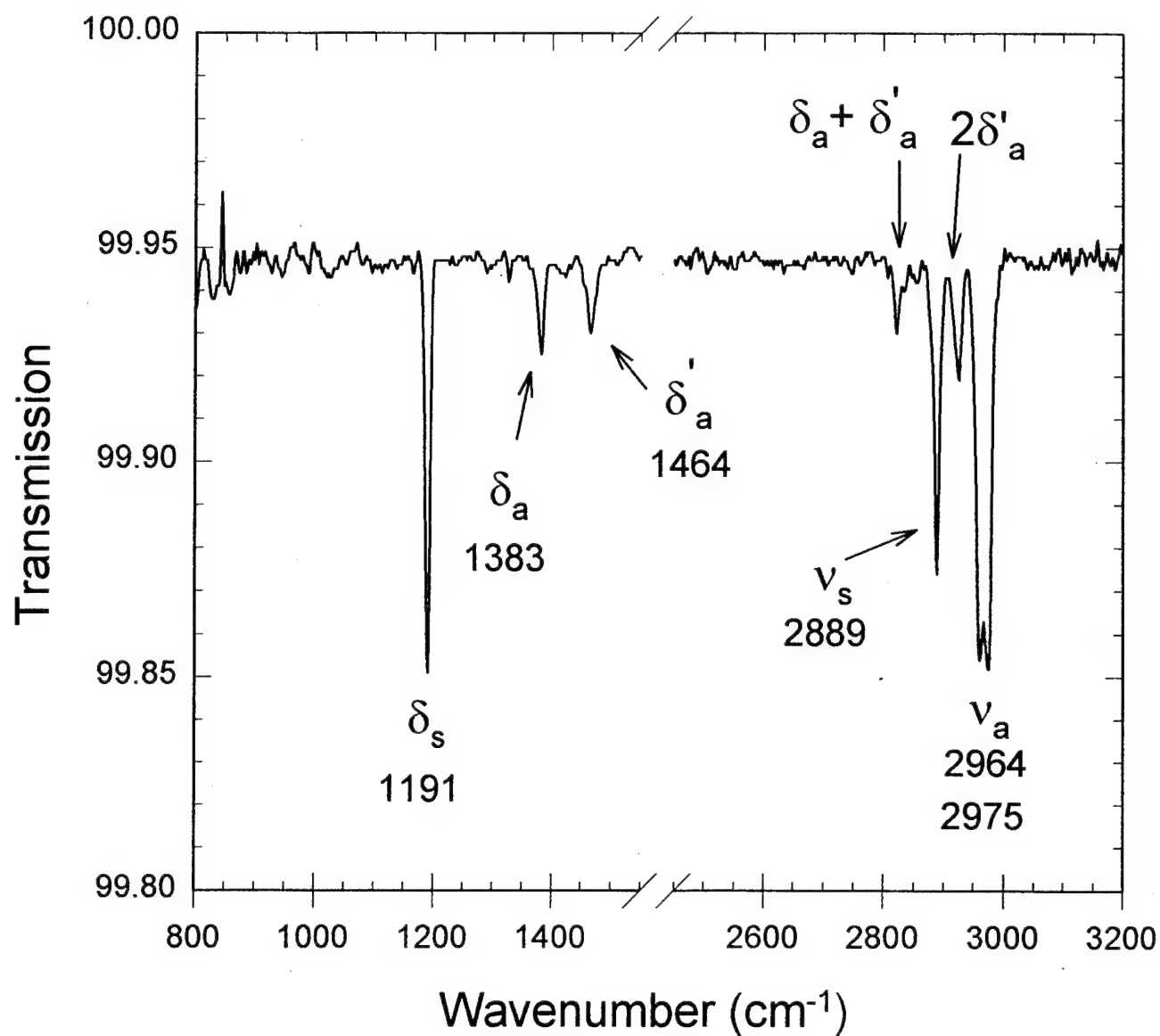
Unpolarized IR spectrum (recorded at 120 K) of the Ga-rich GaAs(100)-(1 X 2)-CH_3 surface prepared by TMGa adsorption at 350°C.

Atomic Layer Controlled Deposition Of Al$_2$O$_3$ Films Employing Trimethylaluminum (TMA) And H$_2$O Vapor

A. W. Ott, A.C. Dillon, H.K. Eaton and S.M. George, Dept. of Chemistry and Biochemistry, University of Colorado, Boulder, Colorado 80309; and J.D. Way, Dept. of Chemical Engineering and Petroleum Refining, Colorado School of Mines, Golden, CO 80401

The development of atomic layer controlled deposition processes has been a focus of recent research(1). The controlled growth of Al$_2$O$_3$ thin films has several important technological applications. For example, Al$_2$O$_3$ deposition on silicon surfaces is useful for the low temperature formation of high dielectric insulators.

Trimethylaluminum [Al(CH$_3$)$_3$] (TMA) and H$_2$O vapor may be employed for controlled Al$_2$O$_3$ deposition using the binary reactions:

A) AlOH + Al(CH$_3$)$_3$ --> Al-O-Al(CH$_3$)$_2$ + CH$_4$

B) Al-O-Al(CH$_3$)$_2$ + 2H$_2$O --> Al-O-Al(OH)$_2$ + 2CH$_4$.
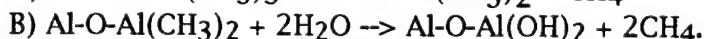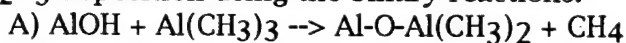
The growth of thin films by the sequential adsorption of water and TMA has been reported on both alumina (2) and silicon surfaces (3). Similarly, a TMA and H$_2$O$_2$ binary sequence was employed for Al$_2$O$_3$ deposition on GaAs and related compounds (4). However, these previous studies did not confirm the surface reaction mechanism. The earlier investigations also did not probe a wide range of reaction conditions in order to establish an optimal Al$_2$O$_3$ growth process.

In the current study, optimal conditions were established for the controlled deposition of Al$_2$O$_3$ on alumina. Alternate H$_2$O and TMA exposures at 0.3 Torr for 1 min. at 500 K provided the most efficient deposition. Previous studies have indicated that alumina film growth processes are nearly independent of the starting substrate (4). Consequently, the optimal Al$_2$O$_3$ growth recipe established here may be employed in a variety of applications.

Sensitivity requirements limit transmission FTIR studies to high surface area materials. ANOPORE porous alumina membranes were obtained from Anotec Inorganic Membrane Technology. These samples provided a surface area of 4 m^2/g. The surface species produced following TMA and H$_2$O adsorption were studied as a function of exposure and alumina surface temperature. In these experiments, the alumina substrate was held at a constant surface temperature for a specified TMA or H$_2$O exposure. Upon evacuation of the chamber, FTIR spectra were recorded at 300 K. Each new porous alumina membrane was annealed to 1000 K for 10 min. prior to the adsorption studies. This procedure was sufficient to convert the amorphous alumina membrane to crystalline γ-alumina (5). Infrared spectra were referenced to background spectra of the newly annealed substrate.

Changes in the infrared absorption spectra of porous alumina membranes versus H$_2$O or TMA exposures at 500 K are displayed in Fig. 1. The broad infrared feature between 3800-2600 cm^{-1} is characteristic of AlO-H stretching vibrations (6). An analysis of bonds assigned to isolated and hydrogen-bonded hydroxyls have been

previously reported (7). The sharp infrared features between 2942-2838 cm^{-1} are consistent with AlC-H$_3$ stretching vibrations (8).

Figure 1 displays the changes in the infrared spectra of a porous alumina membrane versus sequential 0.3 Torr, 1 min. H$_2$O and TMA exposures at 500 K. The infrared spectrum at the top of Fig. 1 was recorded following H$_2$O exposure to a sample previously annealed to 1000 K. The spectrum reveals a broad infrared absorbance in the AlO-H stretching region. Upon TMA exposure, this broad absorption feature disappeared and a concurrent growth was observed in the C-H$_3$ stretching region. Subsequent exposure to H$_2$O resulted in the disappearance of the infrared absorbance of the C-H$_3$ stretching vibrations and an increase in the AlO-H stretching region. These spectral results are consistent with aluminum oxide growth on the alumina surface according to the A and B binary reactions given above.
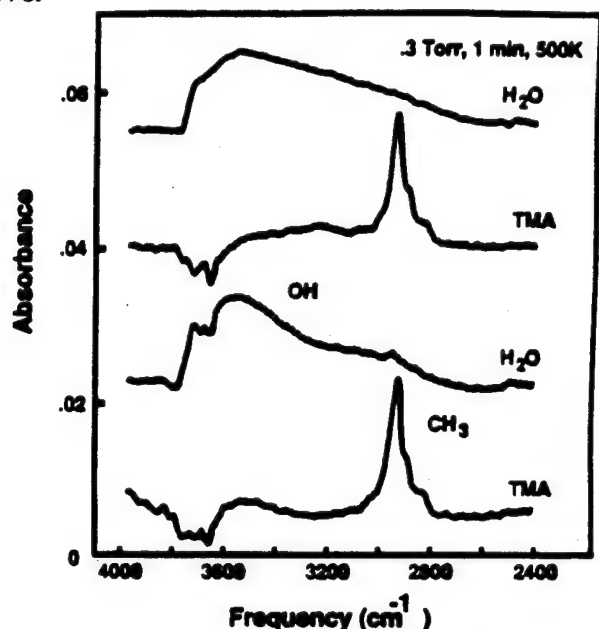
Figure 1 Infrared absorption spectra of porous alumina versus sequential 0.3 Torr, 1 min. H$_2$O and TMA exposures at 500 K

Sequential 0.3 Torr, 1 min. H$_2$O and TMA exposures at 500 K have been shown to be the optimal reaction conditions (7). TMA exposures at less than 500 K resulted in the incomplete reaction of TMA with surface hydroxyl species. In addition, annealing an hydroxylated surface to temperatures greater than 300 K results in the loss of surface hydroxyl species as: 2 Al-OH --> Al-O-Al + H$_2$O. The thermal stability of the hydroxyl species has been previously published (7). At 500 K the hydroxyl coverage is approximately 56% of the maximum hydroxyl coverage at 300 K. The optimal reaction conditions represent a high enough temperature for reaction with the smallest hydroxyl loss possible.

Figures 2 and 3 display the normalized integrated absorbance vs. exposure times for .01 Torr TMA and H$_2$O, respectively, at 500 K. The initial TMA exposure in Fig. 3 was on an alumina surface with a saturation coverage of AlOH species produced by H$_2$O exposure at 500 K. The initial H$_2$O exposure in Fig. 4 was on an alumina surface that had reacted to completion with TMA at 500 K. The integrated absorbances in both Figs. 3 and 4 were normalized to the maximum values.

Figure 2 displays a nearly linear decrease in the AlO-H stretching vibration. A corresponding increase is observed for the infrared absorbance of the C-H$_3$ stretching vibrations of the surface AlCH$_3$ species. The AlCH$_3$ uptake rate eventually slows and indicates the completion of the reaction.

Figure 3 displays a decrease in the infrared absorbance of the C-H$_3$ stretching vibration. Concurrently, an increase is observed for the infrared absorbance of the AlO-H stretching vibrations. This AlOH uptake rate progressively decreases and eventually indicates the completion of the reaction. Figures 2 and 3 indicate that the reaction of H$_2$O with AlCH$_3$ alumina surface species is slightly more rapid than the reaction of TMA with an hydroxylated alumina surface.
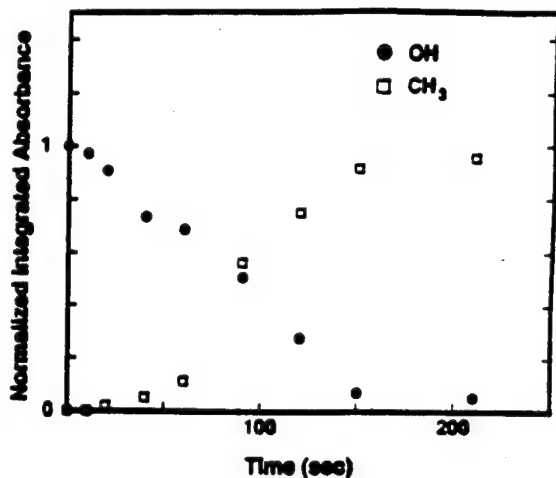
Figure 2 The normalized integrated absorbances of the AlO-H and AlC-H$_3$ stretching vibrations versus a 0.01 Torr, TMA exposure at 500 K.
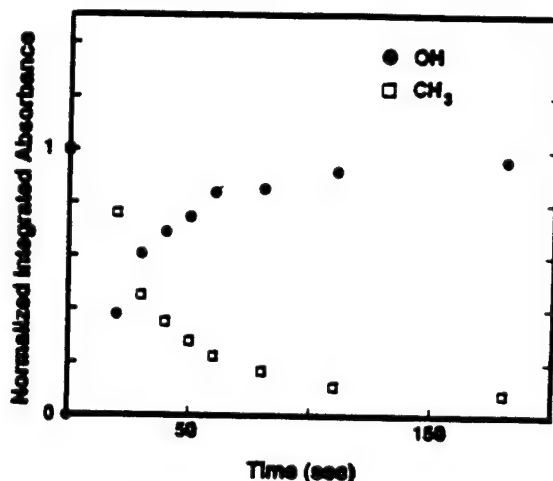
Figure 3 The normalized integrated absorbances of the AlO-H and AlC-H$_3$ stretching vibrations versus a 0.01 Torr H$_2$O exposure at 500 K.

Al$_2$O$_3$ thin film deposition employing the TMA/H$_2$O binary reaction sequence was demonstrated on a sapphire surface for 0.3 Torr, 60 s. TMA and H$_2$O exposures at a variety of reaction temperatures. The surface was prepared by masking half of the crystal with chromium. Fifty TMA/H$_2$O cycles were performed and then the chromium mask was etched away. Atomic force microscopy (AFM) was subsequently employed to determine the step height. For the optimal reaction conditions at 500 K, a step height of approximately 150 Å was observed. This step height corresponds to a growth rate of less than one monolayer/cycle. This rate is consistent with the expected gowth rate given the hydroxyl group stability on Al$_2$O$_3$.

References
1. C.H.L. Goodman and M.V. Pesa, J. Appl. Phys., 60 (1986) R65.
2. C. Soto and W.T. Tysoe, J. Vac. Sci. Technol. A, 9 (1991) 2686.
3. G.S. Higashi and C.G. Flemming, Appl. Phys. Lett., 55 (1989) 1963.
4. J.F. Fan, K. Sugioka and K. Toyada, Jpn. J. Appl. Phys., 30 (1991) L1139.
5. E. Highwell, Anotec Inorganic Membrane Technology, New York, NY (private communications).
6. J.B. Peri, J. Phys. Chem., 69 (1965) 211.
7. A.C. Dillon, A.W. Ott, S.M. George and J.D. Way, Surf. Sci., (*in press*)
8. T. Ogawa, Spectrochim. Acta, 24 (1968) 15.

Kinetic Modeling of the Atomic Layer Epitaxy Window in Group IV Semiconductor Growth

Gyula Eres

Oak Ridge National Laboratory, P.O. Box 2008, Solid State Division, Bldg. 2000, MS 6056,
Oak Ridge, Tennessee 37831-6056
Phone: (615) 574-5494, FAX: (615) 574-4814

Atomic layer epitaxy (ALE) is a method for epitaxial growth of semiconductor thin films that utilizes the adsorption kinetics of source gases for external control of the film growth process [1]. ALE takes advantage of the self-limiting nature of the chemisorption process for achieving layer-by-layer growth of semiconductors with uniform film thickness, ideally, 1 ML per adsorption cycle. The 1 ML/cycle film growth is a uniquely distinguishing feature, that makes ALE highly attractive for preparation of ultrathin films of precisely controlled thickness. Other unique characteristics of ALE growth are that the spatial homogeneity of thin films, and the film thickness per cycle are insensitive to small variations in the external process parameters. The parameter space in which ALE is independent of external conditions is known as the ALE window [2].

The existence of the ALE window in II-VI, and III-V compound semiconductor ALE is intuitive and fairly straightforward to realize in practice [2,3]. The polar nature of the chemical bonding between successive layers in these materials assures that each chemisorption cycle terminates after formation of a monolayer. Multilayer adsorption characterized by much weaker interactions is easily eliminated by elevating the substrate temperature above the range where physisorption occurs. A film of finite thickness is deposited by alternating exposure to the constituent source gases in a sequential fashion.

Because bonding in group IV materials is covalent (non-polar), group IV ALE cannot be realized simply based on the difference in the interaction strength between chemisorption and physisorption. Instead, an alternative strategy that is based on utilizing bonding with peripheral atoms of different electronegativity has been proposed [4]. For example, several processes using the H/Cl exchange reaction for realizing silicon ALE have been reported [5]. Silicon ALE by the H/Cl exchange reaction is perceived to occur between a saturated layer of either surface hydride, or surface chloride with the appropriate silicon source gas to release HCl and to deposit a silicon film. However, formation of an ALE window with either silicon hydride, or silicon chloride source gases is not well understood [6]. In this letter, the role of a fundamental kinetic parameter, the kinetic order of the elementary reaction steps, in formation of the ALE window in group IV semiconductors is explored by modeling the overall film growth reaction in terms of its elementary reaction steps. To facilitate meaningful comparison with experiments, the formation, and evolution of a hydridic layer, for which a wealth of data exist will be used as an example [7]. However, the conclusions that are reached have a general significance, and are applicable in other chemisorption systems.

The surface hydride coverage in epitaxial growth of silicon from silanes is the consequence of the dynamic equilibrium between silane chemisorption and molecular hydrogen desorption. However, instead of the absolute hydride coverage, the description of the thin film growth process is more meaningful in terms of depletion and regeneration of the active film growth sites [7,8]. In group IV thin film growth, the dangling bonds represent the active sites. The depletion of the active surface sites is described by the following rate equation:

$$\frac{d\theta}{dt} = k_1(1-\theta)^n - k_2\theta^m, \tag{1}$$

where θ is the fraction of depleted active sites, k_1 is the depletion rate constant, k_2 is the regeneration rate constant, and n, and m, are the reaction orders of the depletion, and the regeneration steps, respectively.

Hydrogen desorption from Si(100) has received a great deal of attention in recent years because it was found to be first-order, rather than second-order as had been expected for recombinative desorption [9]. Additionally, first-order molecular hydrogen desorption was found following chemisorption of disilane on the Si(100) surface [7]. According to experimental data, first-order behavior of hydrogen desorption from the Si(100) surface is quite general and is independent of whether the hydride coverage is produced by atomic hydrogen adsorption, or by chemisorption of silanes [10]. Similarly, first-order hydrogen desorption was found from the Ge(100) surface following chemisorption of digermane [11]. Therefore, governed by the experimental data, the solution to the above rate equation will only be sought for a first-order ($m = 1$) regeneration step.

In contrast with molecular hydrogen desorption, a consensus has not been reached on the reaction order of the chemisorption step. The results of mechanistic studies of fragments produced by the annealing of

adsorption layers of silanes formed below room temperature, suggest that the elementary reaction step of source gas chemisorption is second-order [12]. On the other hand, the reaction order in kinetic studies of thin film growth processes was found to be first-order [7]. Since the reaction order of the chemisorption step is not clearly established by experiment, both first- ($n = 1$), and second-order ($n = 2$) depletion of active sites need to be considerred in modeling the film growth process.

The solutions to the rate equation describe the time dependence of the active site coverage. The solution for $n = m = 1$ is given by:

$$\theta(t) = \theta_0 \exp[-(k_1 + k_2)t] + \frac{k_1}{(k_1 + k_2)}\{1 - \exp[-(k_1 + k_2)t]\}, \tag{2}$$

where θ_0 is the fraction of the depleted active sites at $t = 0$. For $n = 2$ and $m = 1$ the solution is given by:

$$\theta(t) = \frac{1}{2k_1}\left[2k_1 + k_2 + r\left(\frac{1 - C\exp(rt)}{1 + C\exp(rt)}\right)\right], \tag{3}$$

where $r = \sqrt{k_2^2 + 4k_1 k_2}$, and $C = (2k_1\theta_0 - 2k_1 - k_2 - r)/(2k_1\theta_0 - 2k_1 - k_2 + r)$. In terms of the absolute hydrogen coverage, the above solutions represent pure monohydride coverage.

Since the thin film growth rate is directly proportional to the rate of the active site depletion, the total film thickness $\mathcal{T}$ at time t is obtained by integrating the active site depletion rate from Eq. (1) between 0 and t,

$$\mathcal{T}(\text{ML}) = \int_0^t k_1(1 - \theta(t))^n dt. \tag{4}$$

The integral in Eq. (4) for $n = 1$ is given by:

$$\mathcal{T}(\text{ML}) = -\frac{k_1(\theta_0(k_1 + k_2) - k_1)}{(k_1 + k_2)^2} + \frac{k_1 k_2}{(k_1 + k_2)}t + \frac{k_1(\theta_0(k_1 + k_2) - k_1)}{(k_1 + k_2)^2}\exp[-(k_1 + k_2)t], \tag{5}$$

and for $n = 2$ the integral is given by:

$$\mathcal{T}(\text{ML}) = \frac{k_2(C - 1)\ln(C - 1)}{k_1(C - 1)} + \frac{(k_2 + r)^2}{4k_1}t + \frac{r}{k_1(1 - C\exp(rt))} - \ln(-1 + C\exp(rt))\frac{k_2}{k_1}. \tag{6}$$

Assuming that one original active site is regenerated per atom that is incorporated into the film, Eq. (5) and Eq. (6) describe the evolution of film thickness for first-, and second-order depletion of active sites, respectively.

The significance of Eq. (5) and Eq. (6) is that these equations identify time as an important variable in the ALE of group IV semiconductors. The time-dependence arises because the active sites regenerated by desorption of molecular hydrogen are immediately depleted by chemisorption of new source gas molecules, resulting in continuous film growth. However, the first term in both Eq. (5) and Eq. (6) is independent of time, and suggests that a self-limiting mechanism could be achieved if the contributions from the time-dependent terms are made negligible. Assuming that $\theta_0 = 0$, Eq. (5) shows that ideal ALE, i.e. 1 ML/cycle growth for a first-order chemisorption step requires that $k_1 \gg k_2$,

$$\mathcal{T}(\text{ML}) \approx 1 + k_2 t - \exp(-k_1 t). \tag{7}$$

The exponential term in the above equation is associated with approaching steady-state, and the $k_2 t$ term describes continuous film growth, characteristic of gas source MBE. Eq. (5) and Eq. (7) illustrate that thin film growth from a first-order depletion step occurs by two kinetically different stages. The initial stage corresponding to growth of the first monolayer can be thought to occur in a discrete fashion. After the first monolayer is grown, the rest of the film grows continuosly. Consequently, a strategy for achieving ALE requires separation of the two film growth stages, and assuring that upon completion of the first monolayer, continuous film growth is cut off as quicky as possible. The parameter space for achieving ALE type behavior is illustrated by the three-dimensional plot in Fig. 1. The ALE window corresponds to the plateau region in which monolayer-thick adsorption layer formation is maintained.

In comparison, the expression for thin film growth from a second-order chemisorption step given by Eq. (6), is more complex and shows that elimination of the continuous growth component represented by the

time-dependent terms is more difficult to accomplish. A three-dimensional plot of the film thickness given by Eq. (6) is shown in Fig. 2. The slow approach to steady-state by a second-order chemisorption step provides time for chemisorption on the freshly regenerated sites, and results in the pronounced curvature in Fig. 2. Therefore, second-order chemisorption is less favorable than first-order chemisorption for realization of ALE-like conditions in thin film growth of group IV semiconductors.
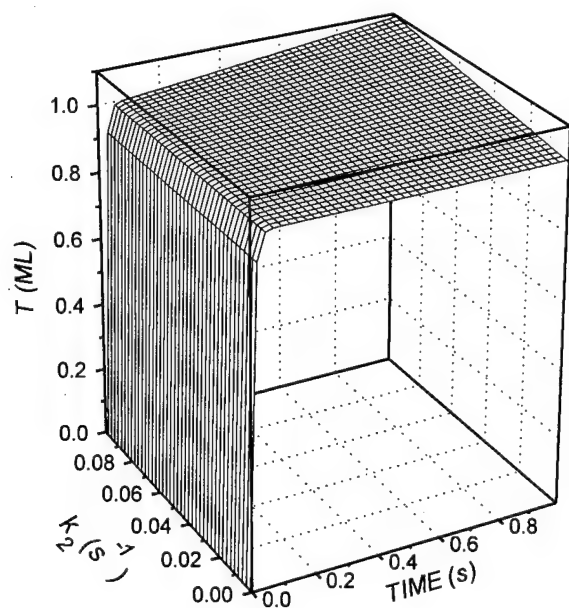
FIG.1. Three-dimensional plot of the film thickness for $n = m = 1$ and a fixed $k_1 = 100s^{-1}$. The plateau in the 1 ML region represents the ALE window.
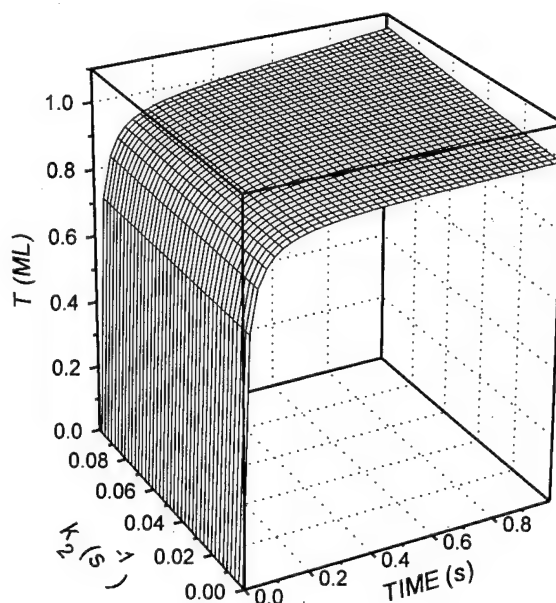
FIG.2. Three-dimensional plot of the film thickness for $n = 2$, $m = 1$ and $k_1 = 100s^{-1}$. The plateau in the 1 ML region represents the ALE window.

[1] See articles in Thin Solid Films **225**, (1993).
[2] T. Suntola, Mater. Sci. Rept. **4**, 261 (1989).
[3] M. Ozeki, Mater. Sci. Rept. **8**, 97 (1992).
[4] C.H.L. Goodman and M.V. Pessa, J. Appl. Phys. **60**, 65R (1986).
[5] Thin Solid Films **225**, 145-212 (1993).
[6] P. Hirva and T.A. Pekkanen, Surf. Sci. **220**, 137 (1989).
[7] G. Eres and J.W. Sharp, J. Appl. Phys. **74**, 7241 (1993).
[8] K. Werner, S. Butzke, S. Radelaar, and P. Balk, J. Crystal Growth, **136**, 338 (1994).
[9] K. Sinniah, M.G. Sherman, L.B. Lewis, W.H. Weinberg, J.T. Yates, Jr., and K.C. Janda, J. Chem. Phys. **92**, 5700 (1990).
[10] K.J. Uram and U. Jansson, J. Vac. Sci. Technol. **B 7**, 1176 (1989).
[11] G. Eres and J.W. Sharp, J. Vac. Sci. Technol. **A 11**, 2463 (1993).
[12] S.M. Gates and S.K. Kulkarni, Appl. Phys. Lett. **58**, 2963 (1991).

Poster Session

MThD 8:00 pm-10:00 pm
Zia B & C

Nanoscale Characterization of InP Islands on InGaP(001)

V. Bressler-Hill,[a,c] C. M. Reaves,[a,b] S. Varma,[c] S. P. DenBaars,[a,b] and W. H. Weinberg,[a,c]

[a] Center for Quantized Electronic Structures, University of California, Santa Barbara, CA 93106

[b] Materials Department, University of California, Santa Barbara, CA 93106

[c] Chemical Engineering Department, University of California, Santa Barbara, CA 93106

voice: (805) 893-4829   fax: (805) 893-4731   e-mail: vbhill@engineering.ucsb.edu

I.   Introduction

Indium phosphide and its related alloys are widely used in optoelectronic materials and devices. Using InP in strained-layer material systems presents a way of producing nanostructures. From growth simulations of InAs/GaAs(001), Ghaisas and Madhukar [1] proposed that islands in registry with the substrate occur before defect formation. In addition, they predicted a critical volume for an island to be coherently strained to the substrate. After this critical volume is exceeded, dislocations or other defects can result. Recently, the existence of strain-induced coherent islands has been verified experimentally in other systems, i.e., Ge/Si(001)[2] and InGaAs/GaAs(001)[3-6], InP/InGaP(001)[7], and InP/GaAs(001)[8] and have all been shown to produce a single type of coherently strained island during growth.

Many studies have looked at the formation of strained islands while varying the parameters which affect the deposited material. Here we investigate, using atomic force microscopy (AFM), the effect of InGaP surface morphology on the size and density of coherently strained InP islands at a constant coverage. From a detailed analysis of the islands on the various surfaces, we have observed that the island density and base area is a strong function of surface morphology, while the height of the islands remains unchanged.

II.   Experimental Procedures

The samples were grown in a metalorganic chemical vapor deposition system which is operated at atmosphere pressure. The gallium source was trimethylgallium (TMG), the indium source was trimethylindium (TMI), the arsenic source was tertiarybutylarsine (TBA), and the phosphorus source was tertiarybutylphosphine (TBP). The GaAs(001) substrates, nominally flat and 2° vicinal, were prepared from an "epi-ready" surface. To remove the surface oxide, a five-minute anneal was performed at 675° C under a 0.6 Torr partial pressure of TBA. The temperature was then lowered to 650° C. A 100 nm GaAs buffer layer was initially grown on the GaAs(001) substrate, followed by a 100 nm InGaP layer. For other optical studies, a 6 nm reference GaAs quantum well was also grown. The final 100 nm layer of InGaP was grown at 650° and 700° C. By varying the substrate angle and growth temperature we obtain markedly different surface morphology. At 700° C, the InGaP singular surface is relatively smooth with morphology consistent with diffusion limited two-dimensional island growth, whereas the vicinal surface shows uniform terraces within the lateral resolution of the AFM. For InGaP deposition at 650° C, the surface morphology is characterized by depressions which can be 6 nm deep and greater than 1 micron in lateral dimensions, while the vicinal surface shows step bunching, i.e., many small terraces in close proximity separated by large (1 μm) terraces.

For the growth of InP on the four different surfaces, the injected partial pressure of TMI was 0.014 Torr, the injected partial pressure of TBP was 3.2 Torr, and the substrate temperature was 650° C   The growth was terminated after 2.3 s and the sample was cooled to room temperature under a TBP over-pressure. The composition of all $In_xGa_{1-x}P$ layers was chosen to be x=0.49 since this stoichiometry is lattice matched to GaAs.

The constant-force AFM images were acquired in air with a Nanoscope III scanning probe microscope. We employed high-resolution silicon tips, supplied by Digital Instruments, with a radius of curvature of approximately 10 nm and a half-angle of 17°.

III. Results and Discussion

AFM images are presented after InP deposition on the 2° vicinal substrates with the InGaP grown at 650° C in Fig 1(a) and 700° C in Fig. 1(b). The InP islands observed on the InGaP singular surfaces grown at 650° and 700° C are qualitatively similar to the islands observed for the 700° C vicinal InGaP surface, and, hence, are not shown here. Considering all four surfaces, three types of islands are resolved independent of the surface morphology. In particular, we observe small, z (height) ≈ 2 nm (type-A), islands and cap shaped medium sized, z ≈ 23 nm (type-B), islands. Large islands, z ≈ 40 nm (type-C), are also observed which have a hexagonal base which is oriented along the [110] crystallographic direction of the substrate. The spatial distribution of the type-B islands is dependent on the surface morphology. For example, in Fig. 1(a), islanding is primarily associated with the edges of the bunched terraces, while a more random spatial distribution of type-B islands is observed in Fig. 1(b) and also for the 650° and 700° C singular surfaces. It is interesting to note that the type-A islands, from which the type-B grow [7], are spatially uniform for all of the surfaces.

From a detailed statistical analysis of the images, measured as a function of InGaP deposition temperature and vicinal angle, the island size distribution in terms of island base area has been plotted in Fig. 2. Since the base area of the various islands are relatively similar, data for all the islands is shown along with data for only type-B and type-C islands. At these coverages, there are few type-C islands (1 per 5 × 5 µm² area) and therefore the type-B islands dominants the type-B and type-C distributions. Generally, the base diameter of the type-B islands is more uniform with respect to the type-A islands for all of the surfaces investigated, as shown by the narrow density distribution with respect to the distribution for all islands.
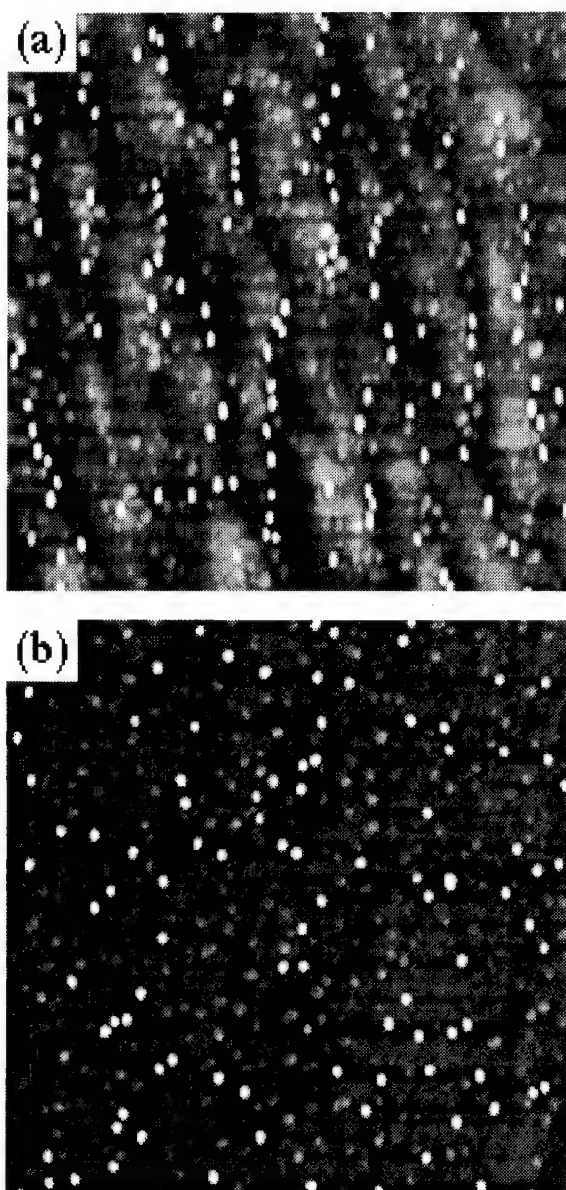
Fig. 1: InP deposition on InGaP lattice matched to a vicinal GaAs substrate. Deposition on InGaP grown at 650° C is shown in (a), while the 700° C surface is shown in (b). Images are 5 x 5 µm².

Depositing the InP on a vicinal InGaP grown at 650° C leads to a higher density of smaller islands as compared with a singular surface. As seen in Fig. 2(a), the island base area distribution decreases from 0.01 µm² to 0.006 µm² (for type-B and type-C islands). However, for deposition on 2°-InGaP grown at 700° C, the base area distribution increases from 0.004 µm² on the singular surface to 0.005 µm². In addition, the island density is

Fig. 2. Density of the InP islands as a function of base area. Densities for islands deposited on InGaP grown at 650° C is shown in (a). Densities for islands deposited on InGaP grown at 700° C is shown in (b). The results for all islands deposited on a singular surface is shown by (– ▣ –), the results for type-B and type-C islands deposited on a singular surface is shown by (– ■ –), the results for all islands deposited on a vicinal surface is shown by (–◇–), and the results for type-B and type-C islands deposited on a vicinal surface is shown by (–◆–).

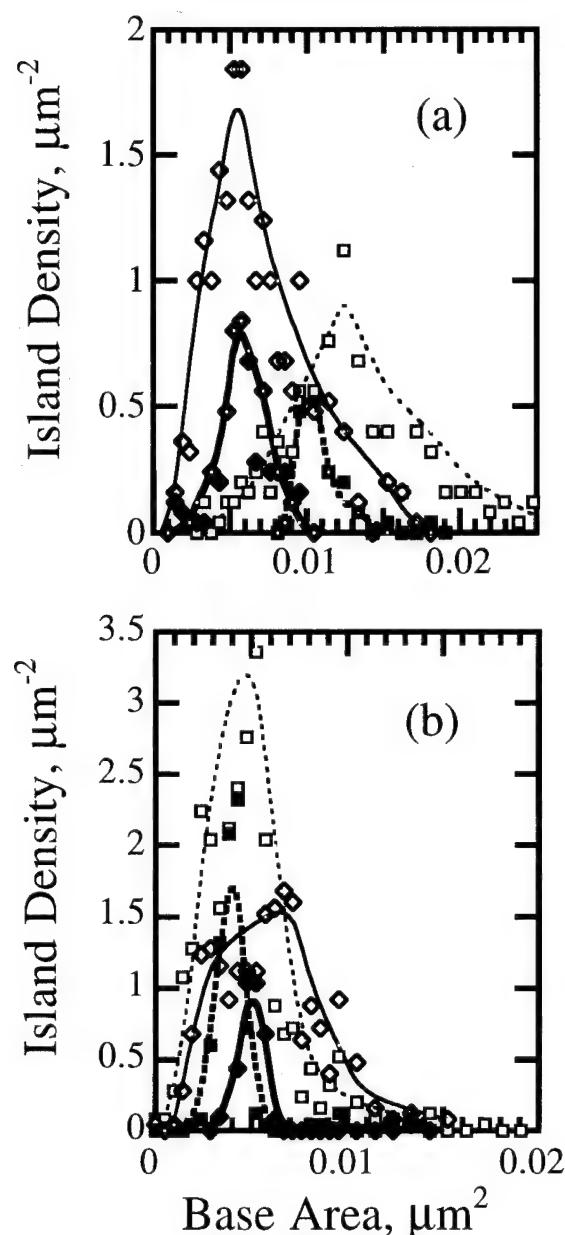increases on the singular surface. This can be understood in terms of the various morphology observed for the four surfaces.

Generally, deposition on rough GaInP surfaces (such as the singular surface grown at 650° C) leads to larger base areas and lower island density. The features making up the rough surface may act as heterogeneous nucleation sites for the InP islands which lead to a broad distribution of sizes. In contrast, the smooth surfaces produced at 700° C leads to homogeneous nucleation where the islands are more dense and smaller.

The heights of the type-A and -B islands remain relatively similar for all of the surfaces investigated. In particular, the type-A island height distribution shows peaks ranging from 1.2-2.6 nm with $\Delta z/z = 1.5$, while the type-B island height distribution shows peaks ranging from 20.9-26.6 nm with $\Delta z/z = 0.3$.

In conclusion, nanoscale InP islands formed on a InGaP(001) surface can be readily studied by AFM. We have found that the morphology of the InGaP surface does not alter the qualitative behavior of the growth. However, the effect on the base diameter and density of the islands is dramatic. The smallest islands, both in base areas and in height, are found on a singular InGaP surface grown at 700° C.

References

[1]   S. V. Ghaisas and A. Madhukar, Proceedings of the SPIE Symposium on Growth of Compound Semiconductor Structures (SPIE, Bellingham, WA, 1988), Vol. 944, p. 16.

[2]   D. J. Eaglesham and M Cerullo, Phys. Rev. Lett. 64 (1990) 1943.

[3]   D. Leonard, M. Krishnamurthy, C. M. Reaves, S. P. DenBaars, and P. M. Petroff, Appl. Phys. Lett. 63 (1993) 3203.

[4]   J. Moison, F. Houzay, F. Barthe, L. Leprince, E. Andre, and O. Vatel, Appl. Phys. Lett. 64 (1994) 196.

[5]   S. Guha, A. Madhukar, and K.C. Rajkumar, Appl. Phys. Lett. 57

[6]   J. Oshinowo, M. Nishioka, S. Ishida, Y. Arakawa, submitted to Appl. Phys. Lett.

[7]   V. Bressler-Hill, C. M. Reaves, S. Varma, S. P. DenBaars, and W. H. Weinberg, submitted to Surf. Sci..

[8]   J. Ahopelto, A. A. Yamguchi, K. Nishi, A. Usui, and H. Sakaki, Jpn. J. Appl. Phys. 32 (1993) L32.

Micro-manipulation of mono-disperse hematite particles by optical trapping

Shunichi Sato, Yasunori Harada, Yoshio Waseda and Tadao Sugimoto
Institute for advanced materials processing, Tohoku University
Katahira 2-1-1, Aoba-ku, Sendai 980-77, Japan
Tel:+81-22-227-6200 ext.2426
Fax:+81-22-261-0938

1. Introduction

Optical trapping technique, which uses a strongly focused laser beam[1], has become an important tool for the precise manipulation of micrometer-sized particles such as polystyrene latex spheres[2] and biological cells[3]. Almost the particles shown to be trapped are spheres, because the production of shape-controlled particles in micrometer range was quite difficult. Recently, mono-disperse hematite (α–Fe_2O_3) particles, of which both the shape and the size are simultaneously well-controlled, are produced by the gel-sol method[4]. It has been revealed that several types of the particle shape, for example, pseudo-cubic and peanut-type, are obtainable. It is very interesting to apply these shape- and size-controlled particles to optical trapping and investigate the feature of the trapped particles. With regard to the microstructure fabrication, these mono-disperse particles are also attractive to use as model parts. We believe that the microstructure fabrication achieved by using optical trapping will be the basis of nanostructure fabrication because nanometer-sized particles, for example, 26 nm silica[1] and 36 nm gold particles[5], have been demonstrated to be optically trapped.

Here we report micro-manipulation of mono-disperse hematite particles by optical trapping. The micrometer-sized hematite particles were optically trapped in water and manipulated one by one or collectively. Particle arrangement, which is not naturally caused by electrostatic force or van der Waals force, was also observed. It was indicated that the micro-manipulation by optical trapping is applicable to fabrication of micro-structure and probably nano-structure.

2. Experiments

Shapes of hematite particles used were pseudo-cubic, ellipsoid-type and peanut-type, which sizes were in the range of a few micrometer. A Nd:YAG laser beam of 1.064 μm wavelength is used for optical trapping. The laser beam was focused by a water-immersion microscope objective of which numerical aperture is 1.2. The beam focus patterns were point and line-shaped. The point focus was mainly used for the trapping of a single particle and the line-shaped focus was for the trapping of plural particles in line.

It was found that all types of hematite particles were trapped two-dimensionally. For example, Fig. 1 shows optical trapping of an ellipsoid-type hematite particle. The laser power
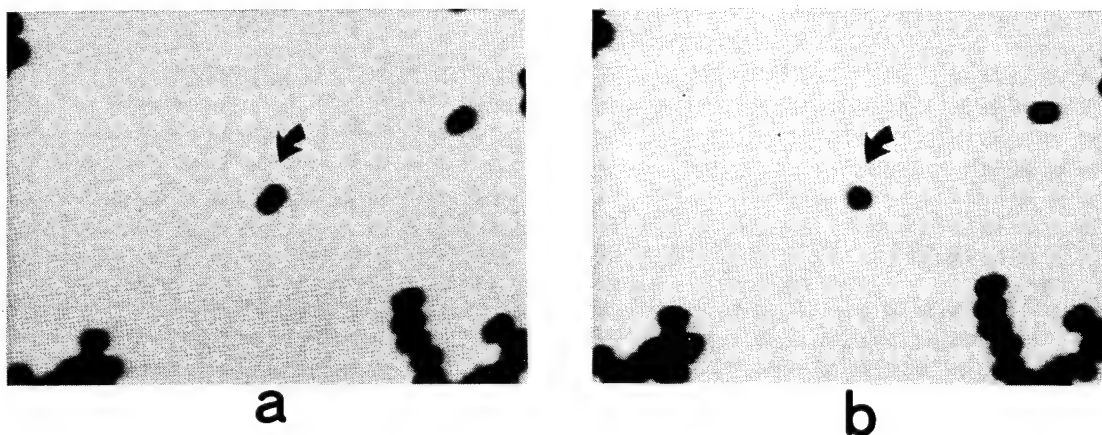
Fig. 1 An example of optical trapping of mono-disperse ellipsoid-type hematite particle. The size of the particle is 2.7 x 1.5 μm. The laser beam of 20 mW with a point focus is used. (a) A particle indicated by an arrow is seen to be ellipsoid before the laser irradiation. (b) The particle is seen to be circle during optical trapping because it is trapped and set up along the laser beam axis.

was approximately 20 mW. Before the trapping, ellipsoidal side of a particle indicated by an arrow is seen (Fig. 1 (a)). When the laser beam of point focus is irradiated, the particle is optically trapped as shown in Fig. 1 (b). It should be noted that the particle seems circle because it is set up along the laser beam axis, although other particles are not trapped and still seem ellipsoidal. This particle can be moved directly and relatively by moving the laser beam and the microscope stage, respectively.

When condensed particle suspension in water are left for several minutes, it is usually observed that the particles contact each other to form long chain provably due to electrostatic force or van der Waals force. For ellipsoid-type hematite particles, formed particle chains are seen as if they are piled up. Namely, the long axis of the particle and the direction of the chain formation is orthogonal. On the contrary, it is possible to connect the particles at their edges by using optical trapping. Then the formed particle chain seems to be a connected frankfurter. Fig. 2 shows an example of edge-connected particle chain by optical trapping. Two ellipsoid-type hematite particles indicated by an arrow are shown to be connected at their edges. In order to form this chain, two particles are trapped one by one using a laser beam with line-shaped focus. In our experiment, it was possible to arrange three or four particles simultaneously. For reference, piled particles, which are connected naturally, are shown in the upper and the lower left-hand sides of Fig. 2.

It is noted that the same phenomenon is observed for the peanut-type particles. For pseudo-cubic particles, the arrangement in line by optical trapping with line-shaped focus beam was also possible. Moreover, when the piled particles are trapped by a laser beam with line-shaped focus, it was observed that all the particles were set up simultaneously.

3. Conclusion

Micro-manipulation of mono-dispersed hematite particles by optical trapping was demonstrated. It is found that optical trapping will be a basic tool for the fabrication of micro-structure.

Until now, observation of second harmonic generation of optically trapped particles[6], which will be useful for the study of the material surface, and rotation of the trapped particles[7] have been reported. Under these circumstances, if production of mono-disperse nanometer-sized particles become possible in the future, nano-structure can be fabricated by optical trapping. It is thought that this macroscopic approach is one way for nano-structure fabrication in contrast with an atomic scale processing.

Fig. 2 An example of optical trapping in line of mono-disperse ellipsoid-type hematite particle. Two particles indicated by an arrow are optically trapped by using a laser beam of 30 mW with line-shaped focus. It is shown that these particles are connected at their edges. On the contrary, naturally assembled particles shown in the upper and the lower left-hand sides are connected at their cylindrical surfaces.

References

1) A. Ashkin, J. M. Dziedzic, J. E. Bjorkholm and S. Chu, Opt. Lett., **11** (1986) 288.

2) S. Sato, M. Ohyumi, H. Shibata, H. Inaba and Y. Ogawa, Opt. Lett., **16** (1991) 282.

3) A. Ashkin, J. M. Dziedzic and T. Yamane, Nature, **330** (1987) 769.

4) T. Sugimoto, M. M. Khan and A. Muramatsu, Coll. Surf., **70** (1992) 167.

5) K. Svoboda and S. Block, Opt. Lett., **19** (1994) 930.

6) S. Sato and H. Inaba, Opt. Lett., **19** (1994) 927.

7) S. Sato, M. Ishigure and H. Inaba, Electron. Lett., **27** (1991) 1831.

Nanomachining of Silicon by Direct Laser Processing

M. Müllenborn, H. Dirac, and J. W. Petersen

Mikroelektronik Centret

Danmarks Tekniske Universitet, Bldg. 345 East

DK-2800 Lyngby, Denmark

Tel. +45 4593-4610

Fax. +45 4588-7762

A laser direct write system consisting of a cw Ar ion laser with UV option, an acousto-optic modulator, high-quality optics for beam expansion and steering, and a reflective objective for focusing, has been designed to etch trenches into Si with nanometer resolution. The Si substrate, mounted in a process chamber, is exposed to Cl_2 gas and heated above its melting point by the laser light. Upon melting, a fast etch reaction is initiated,[1] resulting in an etched profile that corresponds directly to the induced melt. Translating the sample by high-resolution DC motor stages with a bidirectional repeatability of 25 nm, continuous, well-defined trenches are etched into the substrate with an extremely high writing speed of up to 100 mm/s. The trench width is completely determined by the melt size. By decreasing the laser power to the minimum required for melting, we have reached trench widths of less than 150 nm.

Numerical calculation of the induced temperature profile in the substrate, which takes the solid-to-liquid transition as well as temperature-dependent optical and thermal properties into account, reveals that the melt size can be infinitely small, if second order effects such as latent heat and surface tension are excluded. An analytical solution for two phases can be found assuming that generation takes place at the surface only, which is a good approximation for Si at elevated temperatures, and assuming a temperature-independent reflectivity. The temperature-dependent thermal conductivity κ can be included by a Kirchhoff transform using a linearized temperature θ.[2]

$$\theta(T) = \theta(T_0) + \int_{T_0}^{T} \frac{\kappa(T')}{\kappa(T_0)} dT' \tag{1}$$

T_0 is the substrate temperature far away from the excitation. Assuming $\kappa(T) \sim T^{-1}$ below the melting point T_m, it is possible to express the temperature T in terms of θ:

$$T(\theta) = T_k + (T_0 - T_k) \exp\left(\frac{\theta}{T_0 - T_k}\right) \quad , \quad \theta \le \theta(T_m) \tag{2}$$

T_k is found to be 99 K. The temperature dependence of κ above the melting point is not known experimentally. A constant thermal conductivity in the melt, κ_m, would result in:

$$T(\theta) = T_m + \frac{\kappa_0}{\kappa_m}\left(\theta - \theta(T_m)\right) \quad , \quad \theta > \theta(T_m) \tag{3}$$

The linearized temperature distribution follows the solution of Poisson's equation for a single phase:[2]

$$\theta = \sqrt{\frac{2}{\pi^3}}\, P\, \frac{1-R}{\kappa(T_0)\,\omega_0} \int_0^\infty (1+u^2)\, \exp\left(-\frac{2}{\omega_0^2}\left(\frac{x^2+y^2}{1+u^2}+\frac{z^2}{u^2}\right)\right) du \tag{4}$$

P is the laser power, R the reflectivity of Si, and ω_0 the laser spot radius. For the extent of the melt, it is sufficient to know the $\kappa(T)$ dependence below the melt. Melt depth and width decrease monotonously with decreasing laser power according to this analytical solution (Fig. 1).
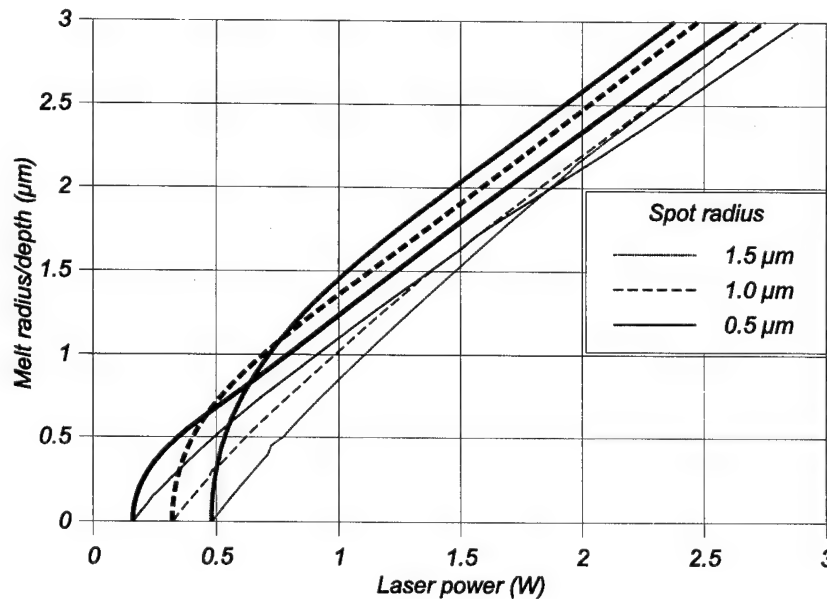

Fig. 1. Melt radius (thick lines) and melt depth (thin lines) as a function of laser power and spot size as calculated by an analytical solution of Poisson's equation for two phases.
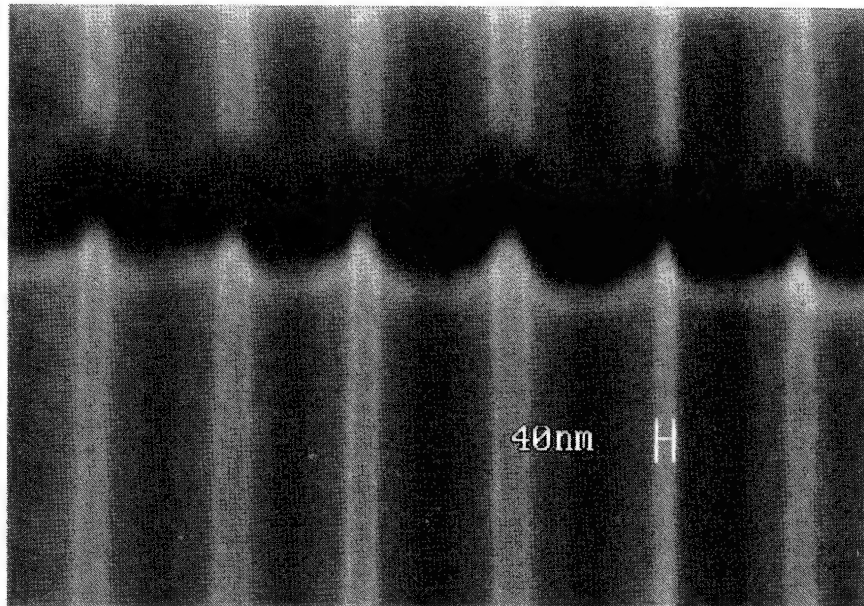
Fig. 2. Scanning electron micrograph of trenches (70° tilted view) etched into Si by 488-nm laser light in Cl_2 atmosphere. The trenches, about 200 nm wide and 300 nm spaced, were written with a scan speed of 10 mm/s, using a laser intensity of 0.6 W and a Cl_2 pressure of 300 mbar.

Experiments show a minimum trench size of less than 200 nm for 488-nm laser light (Fig. 2) and less than 150 nm for 351-nm excitation,[3] which is believed to be due to intensity fluctuations in the generation profile. Other effects, such as latent heat and surface tension, play a role on a scale of some tens of nanometers. If the melt depth approaches this limit, instabilities will prevent the formation of a melt. The melt width has, especially for large spots, a very strong dependence on laser power, which makes the condition for melting sensitive to intensity fluctuations.

Because the widths of the generation and temperature profiles depend linearly on wavelength, it should be possible to reach an even higher resolution with a shorter laser wavelength.

References

1. G. V. Treyz, R. Beach, and R. M. Osgood, Jr., J. Vac. Sci. Technol. B **6**, 37 (1988).

2. D. Bäuerle, *Chemical Processing with Lasers*, Springer Series of Materials Science, Vol. I, Springer Verlag, New York (1986).

3. M. Müllenborn, H. Dirac, and J. W. Petersen, to be published in Appl. Surf. Sci. (1994).

Step Height Standards for Calibrating an AFM/STM

Jean M. Bennett
Physics Department, Mount Holyoke College
South Hadley, Massachusetts 01075
(On leave from Naval Air Warfare Center, China Lake, California)
(413) 538-2816 phone
(413) 538-2357 FAX

Mecky Puiu
VLSI Standards, Inc.
3087 North First Street
San Jose, California 95134-2006
(408) 428-1800 phone
(408) 428-9555 FAX

Van A. Hodgkin
Physics Branch, Naval Air Warfare Center
China Lake, California 93555
(619) 939-3247 phone
(619) 939-6593 FAX

Thomas McWaid
National Institute of Standards and Technology
Gaithersburg, Maryland 20899
(301) 975-3466 phone
(301) 869-0822 FAX

Calibration of an AFM/STM requires step standards calibrated on another type of instrument. Typically this is a mechanical stylus profiler that has been calibrated using step height standards that have been measured with an optical interferometer. Since the bar dimensions are a few micrometers wide and a few tens of nanometers high, standard Fizeau-type optical interferometers cannot be used. Several types of optical profilers are suitable for the measurements. The question is, to what accuracy can a step ~20 to 100 nm high be measured? Intercomparisons between instruments in different laboratories suggest that a reasonable value for the accuracy is no better than 1% of the step height value. Examples will be shown and systematic errors relating to specific instruments will be discussed.

VUV Laser (157 nm) Chemical Vapor Deposition of High Quality Amorphous Hydrogenated Silicon: "Chemical Mechanism"

H.Karstens, J.Knobloch, A.Winkler, A.Pusel, M.Barth, P.Hess
Institute of Physical Chemistry, University of Heidelberg,
Im Neuenheimer Feld 253, D-69120 Heidelberg
TEL: 49-6221-565205; FAX 49-6221-564255

Energetic beams provide nonthermal conditions for film synthesis in order to achieve growth processes and material properties that cannot be obtained by using a thermal flux. However, a detailed understanding of the gas phase and surface chemistry responsible for film growth and the resulting material properties has not been achieved for the complex reaction and transport processes involved. In the following it will be shown how the deposition chemistry can be studied using localized initiation of the deposition chemistry by a VUV laser.

High quality amorphous hydrogenated silicon (a-Si:H) films were deposited from disilane as a source gas using a fluorine laser (157 nm) in a parallel configuration. The deposition of a-Si:H films at very low source gas partial pressures (3-10μbar) was possible due to the high photon flux (4W) and the relatively high absorption cross section of disilane ($5.8 \times 10^{-17} cm^2$) at this wavelength. Regarding its properties, the film material obtained by VUV laser CVD is comparable to high quality plasma CVD films deposited at similar substrate temperatures. Typical values of a sample grown at a substrate temperature of 270°C are a photoconductivity of 6.3×10^{-5} S/cm, dark conductivity of 5.0×10^{-11} S/cm, Urbach energy of 59 meV, optical bandgap energy of 1.62 eV, a hydrogen content of 11 at% and a SiH_2/SiH concentration ratio of 0.08. Besides the established methods for film analysis, in situ mass spectrometry was used to study the gas phase chemistry, in situ FTIR spectroscopy was employed to obtain information on hydrogen bonding and incorporation and the surface topography was measured with an AFM as a function of growth rate.

The composition of the gas phase is strongly dependent on the distance from the laser beam, since the generation of primary photolysis products is localized there and the formation of secondary and tertiary products occurs as the reactive primary species move away from the laser beam by diffusion. By changing the distance between surface and initiating laser beam the dependence of the film properties on the concentration of different precursor molecules has been studied. A one-dimensional model has been developed including diffusion, flow of the reaction gas mixture, chemical reactions, adsorption on the film and on the walls, and the interaction of species with laser light. It computes the spatial and temporal distribution of several gas phase components, the film growth rate on the

basis of estimated sticking coefficients, and the share of different film precursors in the growth process.

We assume H, SiH_2, SiH_3, Si_2H_4, and Si_2H_5 to be the reaction products of disilane photolysis. As the monoradicals H, SiH_3 and Si_2H_5 are far less reactive than the biradicals SiH_2 and Si_2H_4, the model predicts a high production rate of Si_3H_8 and Si_4H_{10} by insertion of these radicals into disilane. This corresponds very well with our mass spectrometric data as shown in Fig.1.
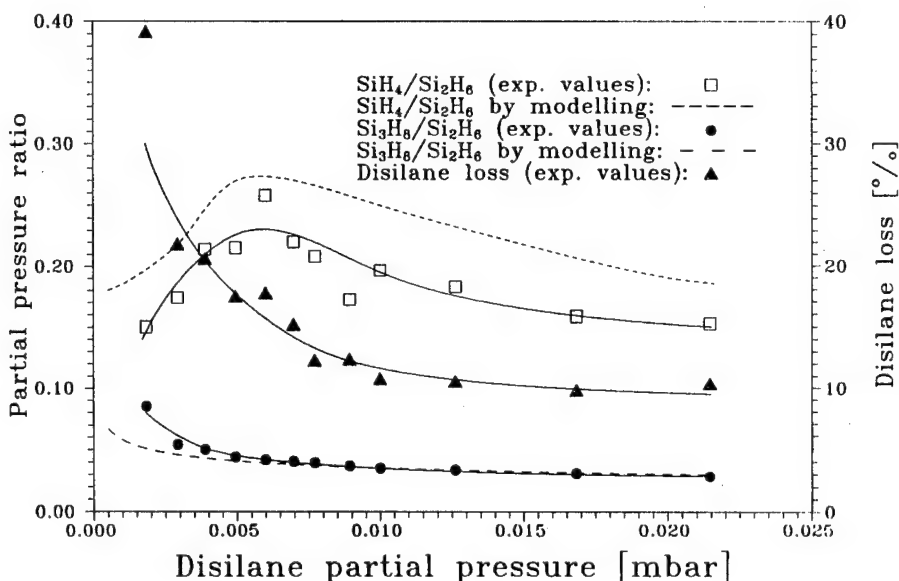

Fig.1: Monsilane/disilane and trisilane/disilane partial pressure ratio: experimental values and data obtained by modelling, and disilane loss by photolysis and secondary reactions (experimental values)

Since most reactions of the biradicals are nearly gas-kinetic, these molecules have a short lifetime and their concentration decreases strongly after their production during the laser pulse as shown in Fig.2. In contrast, the monoradical concentration decreases slowly due to their lower reactivity. Thus, the monoradical to biradical concentration ratio present at the surface can be changed by moving the initiating laser beam away from the surface. The calculated ratio is 1.3 at a distance of 1 mm and 3.4 at a distance of 10 mm. A higher concentration of SiH_2 in the gas phase above the film results in a larger number of SiH_2 groups in the deposited material due to the formation of polysilane chains on the surface. This leads to a deterioration of the electronic film properties. As expected the quality of the deposited films increases with increasing beam/surface distance.

The experiments demonstrate how information on the chemistry-stucture-performance relationships can be obtained. In this way the laser CVD experiments will contribute to a better understanding of the role played by different film precursors and contributes to a controversial issue discussed for many years.
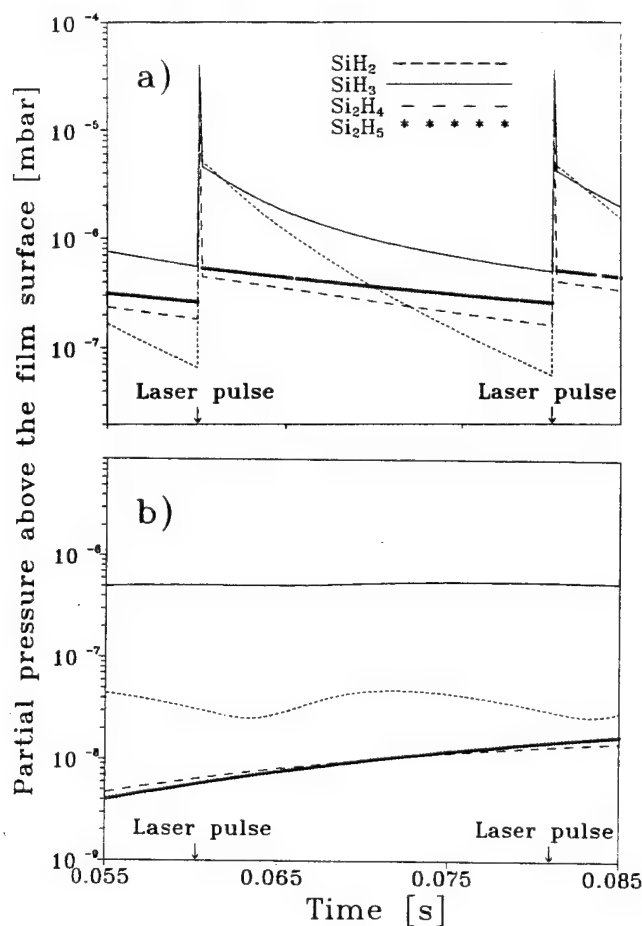

Fig.2: Calculated time evolution of the radical partial pressures at the film surface between two laser pulses. The laser beam/surface distance was a) 1 mm and b) 10 mm, the laser power 2 W and the repetition rate 50 Hz. The disilane partial pressure was 3×10^{-3} mbar in 1 mbar He.

SURFACE PLASMON ENHANCED RAMAN SCATTERING AT GRATINGS : OPTIMIZATION AND STIMULATED REGIME

I. BALTOG[1*] , N. PRIMEAU[1**], R. REINISCH[1], J. L. COUTAZ[2]

1 : LEMO-ENSERG, Unité de Recherche Associée 833 au CNRS, BP 257,
38016 Grenoble CEDEX 1, France
tel : 33 76 85 60 20, fax : 33 76 85 60 80

2 : LAHC, Université de Savoie, 73 376 Le Bourget du Lac CEDEX, France
tel : 33 79 75 87 50, fax : 33 79 75 87 42

* : on leave from Institute of Atomic Physics, Bucharest, Romania

** : corresponding author

The electromagnetic origin of surface enhanced Raman scattering (SERS) may involve local or delocalized surface plasmons (SP). We consider here grating excited delocalized SP. It is known that these SP may be resonantly excited leading in this way to enhanced Raman scattering. It has been even predicted that there exists an optimum groove depth of the grating for which the Raman efficiency is the greatest [1]. To the best of our knowledge, this effect has only been observed in the case of a prism coupler in the Kretschmann configuration where an optimum Ag-thickness has been found[2]. In this Communication, we report on optimized SERS at a coated grating of variable groove depth. We also show that, when optimization is achieved and SP resonance occurs, the Raman process is no longer a spontaneous one but becomes stimulated.

Two types of gratings were used. The experiment concerning the optimization has been performed using a grating of sinusoidal profile, of periodicity d =5556 Å and variable groove depth [3] ranging from 200 Å up to 800 Å. This grating was holographically made in a photoresist layer deposited on a glass substrate ; it was covered by 2000 Å of evaporated silver and then by a thin 50 Å overlayer of evaporated copper phthalocyanine (CuPc). The experiment is performed using an Argon ion laser working at 5145 Å. At the sample location, the maximum power is 30 mW and the spot size 135 μm^2. The excitation of the SP at the pump frequency is achieved through the +1 diffracted order of the grating. The outcoupled Stokes light (frequency ω_s) is focused on the entrance slit of a single pass HR-640 Jobin-Yvon monochromator equiped with a 1800 grooves/mm grating. The data are recorded through a computer assisted acquisition system. For each measurement, the angles of incidence and detection are independently adjusted in such a way that i) SP excitation occurs at the pump frequency and ii) the outcoupled SP at the Stokes frequency is detected. This is done for several groove depths of the grating.

Fig. 1 is a plot of the peak Stokes intensity as a function of the groove depth h for the 1530 cm^{-1} line of CuPc. It is seen that the optimum value of h is around 500Å.
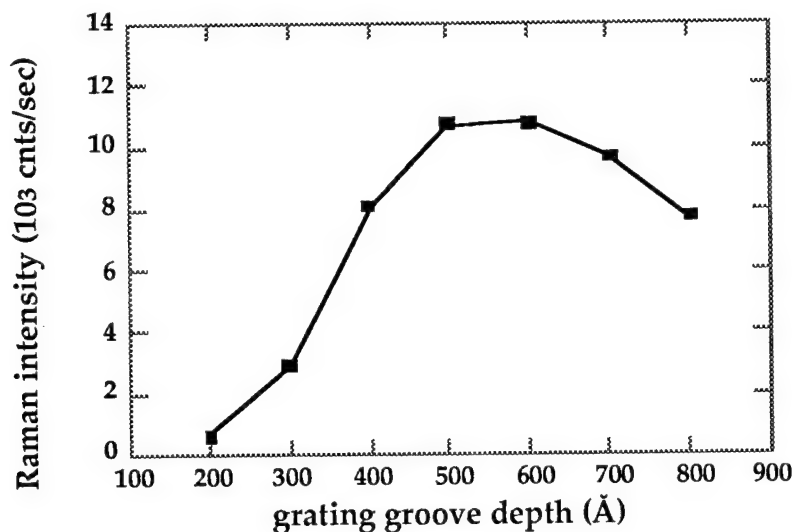
Fig. 1 Intensity of the 1530cm^{-1} Raman line of CuPc versus the grating groove depth. The line is meant to be a guide for the eye.

The existence of a groove depth for which the Raman efficiency is the greatest results from the simultaneous resonant excitation of SP at the pump and at the Stokes frequencies [2]. For the evaluation of the resulting enhancement, the reference is a flat silver surface coated by the *same* thin CuPc layer as for the grating case. In order to record the *very weak* signal generated by this coated *flat* surface, an *improved* detection system was necessary, consisting in a triple-pass T 64000 Jobin-Yvon monochromator together with a cooled CCD array associated to a photon counting system. The value of the enhancement E is determined as follows : we compare the Raman intensity per unit solid angle of detection considering the Stokes signal of the grating and of the flat surface. The influence of the depolarization factor is also taken into account. It must be noticed that for the flat surface, due to the incoherent nature of the spontaneous Raman emission, the solid angle is 2π, whereas for the grating experiment, due to the excitation of SP at Stokes frequency, the Raman beam propagates in a well defined direction. Accordingly the measured values of E is $E \approx 10^5$.

Another set of experiments has been performed using a nearly optimized lamellar grating of periodicity d =7000 Å with groove depth of 700 Å. As before, the grating was covered by 2000 Å of evaporated silver and then by a thin overlayer of evaporated CuPc of thickness 50 Å.

Figure 2 is a plot of $\text{Log}(I_{\text{Raman}}/I_{\text{Laser}})$ as a function of I_{Laser} (I_{Raman} and I_{Laser} respectively denote the Stokes and the laser light intensities) at an angle of incidence leading to SP resonance.
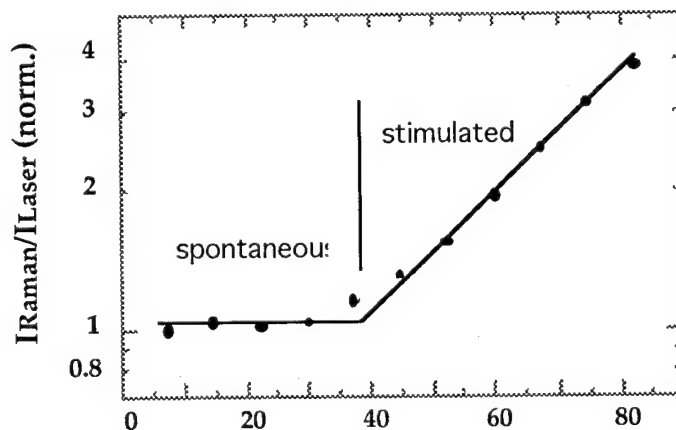

Fig. 2 $\text{Log}(I_{\text{Raman}}/I_{\text{Laser}})$ as a function of I_{Laser}. The two straight lines are meant to be a guide for the eye.

The existence of a threshold corresponding to I_{Laser}, which is of the order of 40 mW, is clearly observed : below this value, I_{Raman} is proportionnal to I_{Laser} and the Raman scattering is *spontaneous*. Above this value, the dependence in the laser intensity is an exponential one. This is the signature of a *stimulated* Raman effect. *These results are all the more noteworthy that the CuPc film has a very low thickness of 50 Å.*

It can be shown, using the coupled-mode formalism[4], that the amplitude c_s of the SP at the Stokes frequency is given by the following expression :

$$c_s(x) = c_s(0)e^{\omega_s |\xi_s''||c_\ell|^2 x} e^{-j\omega_s \xi_s'|c_\ell|^2 x} \tag{1}$$

In eq. 1, x denotes the direction of propagation of the SP along the mean plane of the grating; c_ℓ is the amplitude of the SP at the incident laser frequency; $\xi_s = \xi_s' + j\xi_s''$ is related to the overlap integral[4] and to the Raman nonlinear susceptibility at the Stokes frequency.

According to eq. 1, in the stimulated regime the SP intensity at the Stokes frequency depends exponentially on the laser intensity. This result which also holds for the diffracted Stokes beam is consistent with the curve reported on fig. 2.

The existence of an optimum groove depth leading to the largest enhancement of the Raman intensity has been experimentally demonstrated. The corresponding enhancement, of the order of 10^5, explains why the Raman spectra of a 50 Å thick CuPc layer can be recorded using a low sensitive detection system while an improved one is required for the flat case. It is remarkable that a stimulated regime exists for such a thin film of CuPc and a so low value of the pump power allowing the use of a cw laser. The experimental results reported in this paper demonstrate the interest of SP enhanced Raman scattering. This shows that the grating geometry is well adapted to Raman spectroscopy of thin (a few monolayers) films.

References

1. M. Nevière and R. Reinisch, Phys. Rev. B26, 5403 (1982)
2. N. Primeau, J. L. Coutaz and L. Abello, J. Appl. Phys. 73, 5158 (1993)
3. This grating is the same than the one previously used in a total reflection experiment at gratings : M. C. Hutley, D. Maystre, Opt. Commun. 19, 431 (1976).
4. "Theory of dielectric waveguides" in Integrated Optics, H. Kogelnik, ed. T. Tamir, Springer-Verlag (N. Y. 1975)

Z-scan Measurements of Porous Silicon Particles in a Colloidal Suspension

S. S. Choi, Department of Physics and Applied Physics, University of Massachusetts Lowell, One University Ave., Lowell, Ma 01854, M. A. Fiddy, Department of Electrical Engineering, University of Massachusetts Lowell, One University Ave., Lowell, Ma 01854, (508) 934-3300, Fax # (508) 934-3027.

Since Canham's report that porous silicon (PS) exhibits efficient visible photoluminescence under UV illumination at room temperature [1], extensive investigations addressing porous silicon's pore formation, surface morphology, photo/electroluminescent mechanism(s), and applications are already well reviewed [2-5]. Although much debate still surrounds porous silicon in the aforementioned areas, the viability of porous silicon as an optoelectronic material (e.g. optical switch) is well realized [6]. Thus, the motivation for our efforts is to find a new viable optoelectronic medium, namely a colloidal suspension of porous silicon nanoparticles in some cases microparticles. Colloidal suspensions of gold and polymer composites, possibly due to quantum confinement effects, have yielded large third order nonlinearities of 10^{-5} to 10^{-8} esu [7].

Porous silicon is formed in an electrochemical dissolution process with hydrofluoric acid (HF) as the electrolyte. Porous silicon's visible emission wavelength (red/orange, green/blue), morphological structure, and particle dimensions are dependent upon the wafer dopant and carrier density, the HF concentration, the applied current, and the etch time [3]. We have observed that powder-like microcrystalline particles can be formed on the surface of porous silicon which is readily separable physically, chemically, or ultrasonically. Furthermore, these removed microparticles continue to photoluminesce under UV (366 nm) illumination. In the myriad of papers concerning porous silicon, only a few papers have demonstrated unconventional examination of porous silicon particles. S. Guha et. al. have reported that porous silicon grains embedded in polymethyl methacrylate disks exhibited photoluminescent intensity comparable with that of porous silicon on a substrate [8]. This demonstrates that porous Si grains retain their inherent luminescent characteristics in a polymer. As described in Subhash H. Risbud's et. al. work, Si nanoparticles sequestered in a glass matrix exhibited visible photoluminescence (500 nm) upon UV excitation [9].

The third order nonlinear optical susceptibility of our colloid samples are determined with the Z-scan technique. The Z-scan is a simple yet a highly sensitive technique, based on the principles of spatial beam distortion, to determine the sign and the magnitude of the nonlinear refraction as well as the nonlinear absorption [10]. Again, our work demonstrates the viability of porous silicon particles in a colloidal suspension as an optoelectronic material. It also illustrates the fundamental principle of quantum confinement and the associated saturable absorption as a mechanism for the observed third order nonlinear effect.

References

[1] L. T. Canham, "Silicon Quantum Wire Array Fabrication by Electrochemical and Chemical Dissolution of Wafers," Appl. Phys. Lett. **57**, 1046-1048 (1990).

[2] R. L.Smith, S. D. Collins, "Porous Silicon Formation Mechanism," J. Appl. Phys. **71**, R1-R22 (1992).

[3] P. C. Pearson, J. M. Macaulay, S. M. Prokes, "The Formation, Morphology, and Optical Properties of Porous Silicon Structures," J. Electrochem. Soc. **139**, 3373-3378 (1992).

[4] K. H. Jung, S. Shih, D. L. Kwong, "Developments in Luminescent Porous Si," J. Electrochem. Soc. **140**, 3046-3064 (1993).

[5] Daniel C. Bensahel, Leigh T. Canham, Stephano Ossicini, "Optical Properties of Low Dimensional Silicon Structures," NATO ASI Series: Applied Sciences **244**, Kluwer Academic (1993).

[6] L. T. Canham, "A glowing future for silicon," New Scientist April 10, 23-27 (1993).

[7] A. E. Neeves, M. H. Birnboim, "Composite Strucutures for the Enhancement of Nonlinear-Optical Susceptibility," J. Opt. Soc. Am. B **6**, 787-796 (1989).

[8] S. Guha, G. Hendershot, D. Peebles, P. Steiner, F. Kozlowski, W. Lang, "Photoluminescence and Raman Studies of Porous Silicon in Polymethyl Methacrylate," Appl. Phys. Lett. **64**, 613-615 (1994).

[9] Subhash H. Risbud, Li-Chi Liu, James F. Shackelford, "Synthesis and Luminescence of Silicon Remnants Formed by Truncated Glassmelt-Particle Reaction," Appl. Phys. Lett. **63**,1648-1650 (1993).

[10] Mansoor Sheik-Bahae, Ali A. Said, Tai-Huei Wei, David J. Hagan, E. W. van Stryland, "Sensitive Measurement of Optical Nonlinearities Using a Single Beam," IEEE J. Quantum Electron. **26**, 760-769 (1990).

Laser and Optical Surface Analysis

MFA 8:30 am-10:00 am
Zia B & C

Richard M. Osgood, Jr., *Presider*
Columbia University

Optical Diagnostics during Film Processing of Micro- and Nanostructures

Irving P. Herman

Department of Applied Physics and Columbia Radiation Laboratory

Columbia University

202 S. W. Mudd

New York, NY 10027

(212) 854-4950 phone

(212) 854-1909 fax

The importance of real-time *in situ* sensors during the fabrication of electron and photon devices is increasing in light of tighter device tolerances, the trends toward larger wafer sizes and *in situ*, cluster and flexible processing, and the need for submonolayer composition control in heterostructure fabrication and surface passivation. Optical spectroscopies are often excellent diagnostics for practical control of these film processes, as well as for related fundamental and process development studies. They can be sensitive to crucial material and process parameters, and are usually noninvasive and nondestructive. The range of optical spectroscopies of the gas phase, the surface and the substrate that can be used to monitor gas-surface processes are surveyed. Of particular interest in micro- and nanoprocessing are optical probes that can determine the composition in regions near a surface or interface with submonolayer resolution and those that can measure temperature. The fundamental physical mechanisms underlying these applications are discussed.

Some optical probes are specifically sensitive to properties near a surface or interface. For example, several reflection-based methods, such as infrared reflection-absorption spectroscopy (IRAS), differential reflectometry, surface photoabsorption (SPA) and reflectance difference (anisotropy) spectroscopy (RDS/RAS), and other optical probes,

such as Raman scattering (under special conditions), laser-induced thermal desorption (LITD) and surface second harmonic generation, are surface specific. Other optical spectroscopies can provide detailed information about the surface though they are not inherently surface specific, including reflection ellipsometry, absorption (by transmission), and laser light scattering (LLS). Specific real-time applications of these probes to the submonolayer composition analysis of the surface region during etching and deposition are detailed. One application is the use of laser-induced fluorescence (LIF) to probe adsorbates that are desorbed from the surface by LITD during etching of wafers by a high density plasma.[1,2]

Virtually every optical spectroscopy can be used to measure temperature of either the substrate or the gas above it. Several applications of optical probes to the measurement of temperature will be presented. The basis of most optical thermometries can ultimately be traced to either one or two factors. One factor is the distribution function for species in a given system in thermal equilibrium; this species is either probed directly or affects optical parameters that are probed. These species may obey Maxwell-Boltzmann statistics (molecules - their state and velocity distributions), Bose-Einstein statistics (photons and phonons), and Fermi-Dirac statistics (free electrons and holes in a solid). The thermal population of phonons and the second factor, anharmonicity, and are important in practically every optical probe of temperature in solids.

1. I. P. Herman, V. M. Donnelly, K. V. Guinn, and C. C. Cheng, Phys. Rev. Lett. 72, 2801 (1994).

2. C. C. Cheng, K. V. Guinn, V. M. Donnelly, and I. P. Herman, J. Vac. Sci. Technol. A 12, 2630 (1994).

Profiling and Light Scattering Studies of Si Surfaces

E. L. Church and P. Z. Takacs
Brookhaven National Laboratory, Upton NY 11973-5000

J. C. Stover
TMA Technologies, Inc., Bozeman MT 59715

There is great interest in the semiconductor industry in the development of light-scattering techniques for the detection of "killer particles" on silicon-wafer surfaces. One of the principal limitations in the performance of such devices is the presence of background scattering or "haze" due to scattering from the random residual microtopography of silicon surfaces [1].

The threefold relationship between surface scattering, microroughness and profile measurements is well established in the literature [2-6]. Manufacturers of laser-scanning instruments have used these results to suppress haze effects through the use of glancing-incidence geometry, side collection, and polarization selection [7].

These design principles depend on angular and polarization dependencies that appear as separate factors in the expression for weak topographic scattering. In this paper, however, we are concerned with that additional factor that carries information about the surface topography -- the power spectral density (PSD) of the surface roughness.

The surface PSD is important since it determines the intensity and angular dependence of the background scattering. Understanding the nature and origin of this quantity will lead to a deeper understanding of finishing processes, and the possibility of improving detection performance by reducing the overall background intensity.

We have measured a number of silicon-wafer surfaces using light-scattering (BRDF), and optical- and AFM-profiling techniques. The scattering measurements have shown that the surfaces have the radiation-wavelength and angular dependencies expected for weak topographic scattering [8]. That established, we have used those measurements and independent profile measurements to deduce the consistent values of the surface PSDs over the spatial wavelength range from 50 nm to 1 mm.

Generally speaking, the profile PSDs are found to consist of a sum of inverse power-law components; that is,

$$PSD = S_1(f_x) \approx \sum \frac{K_n}{f_x^n}$$

where the values of K_n and the exponent n vary from surface to surface, but $1 < n < 3$. In other words, the surfaces are fractal-like [9]. Further experiments are now under way to confirm and extend these results, particularly at short spatial wavelengths.

There is an interesting analogy between the present results and the spontaneous thermodynamic roughening of solid surfaces. Below the critical roughening temperature the surface topography is determined by the underlying crystal structure, while above that temperature the surface "melts" and the roughness is determined by capillary-wave excitations of the surface.

Capillary waves have a well-known 1/f sub x profile power spectrum [10], while the PSD of low-temperature Si surfaces are complicated functions of the terrace and step distributions on the surfaces [11,12].

In these terms, the long-wavelength part of the measured PSD corresponds to the "high-temperature" surface, where the mechanics of the polishing process play the role of temperature, and the short-wavelength part of the spectrum corresponds to the "low-temperature" surface, where the roughness is dominated by crystal effects.

Whether this analogy is only superficial (sic) or has deeper physical significance, remains to be seen. In particular, the mechanism that would convert the $n = 1$ capillary-wave spectrum into the $1 < n < 3$ observed spectra has not yet been established. Also, it is not yet clear how terrace spectra can be averaged into the inverse-power-law forms observed in profile measurements.

REFERENCES

1. SEMATECH Symposium on Particles, Haze and Microroughness on Silicon Wafers. Austin, Texas, 2 - 3 November 1993, and the ASTM/NIST/SEMI Conference on Particles, Haze, and Microroughness on Silicon Wafers, San Jose, California, 22-23 September 1994.
2. E.L. Church, H.A. Jenkinson, and J.M. Zavada, "Relationship Between Surface Scattering and Microtopographic Features," Optical Engineering 18 (2), pp. 125-136, (1979)
3. E.L. Church and P.Z. Takacs, "Use of an optical-profiling instrument for the measurement of the figure and finish of optical-quality surfaces," Wear 109, pp. 241-257, (1986)
4. E.L. Church and P.Z. Takacs, "Specification of surface figure and finish in terms of system performance," Applied Optics 32 (19), pp. 3344-3353, (1993)
5. E.L. Church, P.Z. Takacs, and T.A. Leonard, "The prediction of BRDFs from surface profile measurements," in Scatter from Optical Components, J.C. Stover, ed., Proc. SPIE 1165, 136-150 (1989)
6. E.L. Church and P.Z. Takacs, "The optimal estimation of finish parameters," Proc. SPIE 1530, 71-85 (1992)
7. T. Larson, K. Gross and S. Stokowski "Surface scattering and its effect on defect detection in laser inspection systems". Presented at the ASTM/NIST/SEMI conference in San Jose given in ref. 1 above.
8. J.C. Stover, M.L. Bernt, E. Church, and P. Takacs, "Measurement and Analysis of Scatter from Silicon Wafers," to appear in Stray Radiation in Optical Systems, R.P. Breault, ed., Proc. SPIE 2260
9. E.L. Church, "Fractal surface finish," Applied Optics 27 (No. 8), pp. 1518-1526, (1988)
10. M. Bernasconi and E. Tosatti, "Reconstruction, disordering and roughening of metal surfaces", Surface Science Reports, Vol 17, Nos. 7/8, 1993 (Aug 1993).
11. M. Henzler, "Mesurement of surface defects by low-energy electron diffraction", Applied Physics A 34, 205-214 (1984).
12. P. R. Pukite, C. S. Lent and P. I. Cohen, "Diffraction from stepped surfaces", Surface Science 161, 39-68 (1985).

Laser Diagnostics of Film Properties by Coherent Surface Wave Pulses

Peter Hess
Institute of Physical Chemistry, University of Heidelberg,
Im Neuenheimer Feld 253, D-69120 Heidelberg
TEL: 49-6221-565205; FAX 49-6221-564255

Thin and ultrathin films play an increasing role in science and technology. In most cases conventional methods cannot be used to measure the mechanical and elastic properties of these films. Therefore, new techniques for the analysis of layered structures with nanoscale depth resolution are urgently needed.

A novel method has been developed for the determination of mechanical and elastic properties of thin films such as film thickness, density, Young's modulus and Poisson's ratio. In this technique short laser pulses (ns-ps) are used to excite a surface acoustic wave pulse ("broadband surface wave packet") and a cw laser (Michelson interferometer, probe beam deflection) or piezoelectric foil detector are employed for time-resolved detection of the resulting surface displacements (see Fig.1). With these detection methods displacements in the Ångstrom range can be measured at a frequency bandwidth of several hundred megahertz. Since surface waves penetrate only about one wavelength into the solid, the frequency spectrum of the broadband pulse (500 MHz) allows the simultaneous probing of different depths. If the surface is covered with a thin film the coherent waves with different wavelengths travel with distinct phase velocities causing strong interference effects with increasing propagation distance. Fourier transformation of the resulting oscillatory signals detected at two different distances of several millimeters to centimeters yield the dispersion of the phase velocity which can be used for the accurate determination of film properties such as Young's modulus and Poisson's ratio. These two elastic constants completely define the elastic properties of an isotropic film. In addition, the frequency dependence of the attenuation of the wave pulse is obtained, containing information on the microstructure and morphology of the material.

For a silicon single crystal surface the phase velocity of the wave pulse changes not only with the crystal plane but also with the direction on the plane. No dispersion of the wave packet is observed for a hydrogen-terminated ideal Si(111) surface prepared by etching of thermally oxidized samples in hydrofluoric acid. The thin native oxide layer, normally present on the silicon surface, leads to a linear decrease of the phase velocity with frequency ("normal dispersion"). This small dispersion effect has been used to determine the thickness of the oxide layer. Doping of the silicon crystal also causes a measurable dispersion effect.
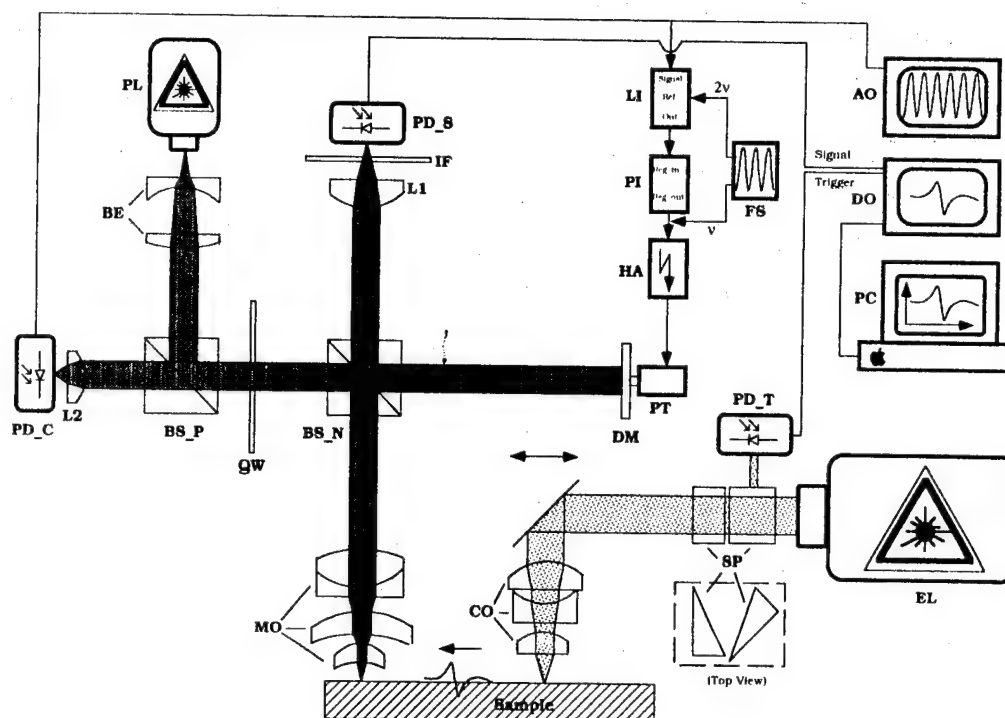
Fig.1: Scheme of the experimental setup with the excitation laser (EL: pulsed Nd:YAG, 355 nm) and the probe laser (PL: diodepumped Nd:YAG, 532 nm) and detection with a stabilized Michelson interferometer.

For layers or films with a thickness in the micrometer range the dispersion becomes nonlinear. In this case up to three film properties have been determined simultaneously, such as the density and two elastic constants by using a theoretical model to fit the measured dispersion curve. As an example results are presented for amorphous hydrogenated silicon films (a-Si:H) deposited on different substrates. For state-of-the-art films used in photovoltaics the density is only a few percent less than the crystal value and the Young's modulus (E-modulus) is only about 10%-30% smaller.

The element carbon exists in structures with extreme mechanical and elastic properties. Therefore, different carbon films with widely varying properties have been studied. For fullerite films the density (C_{60}: 1.67 g/cm^3, C_{70}: 1.64 g/cm^3), the Youngs's modulus (C_{60}: 10 GPa, C_{70}: 4 GPa), and the Poisson's ratio (C_{60}: 0.25, C_{70}: 0.35) have been determined for the first time. The results show that this is the softest allotrope of carbon. Attenuation measurements provide a new approach to study the internal motion of the fullerene molecules in the network.

The method has also been used to control the quality of amorphous carbon films (a-C, a-C:H). Most films investigated were more graphitelike with densities around 2 g/cm^3 and a Young's modulus at least an order of magnitude lower than the diamond value. The hardest films had a density around 2.9 g/cm^3 (diamond: 3.5 g/cm^3) and a Young's modulus of 400 GPa (diamond: 1164 GPa) (see Fig.2). This is in agreement with the best properties reported in the literature for diamondlike films and demonstrates the existing gap between the amorphous network and the diamond structure.
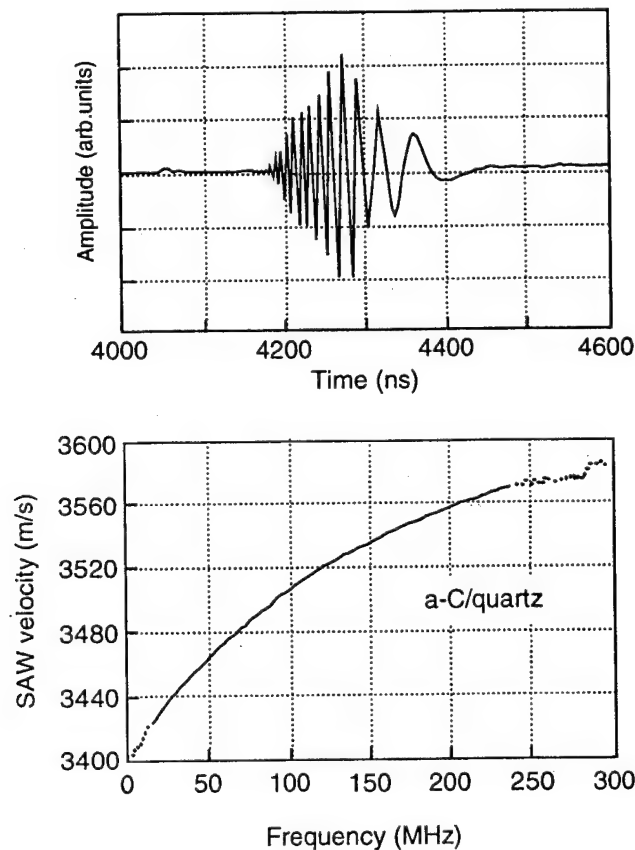

Fig.2: Measured oszillatory signal for a diamondlike carbon film on quartz and resulting anomalous dispersion of the phase velocity with curve fitted for extraction of film properties.

The large variety of possibilities for the diagnostics of layered structures and the ultimate limit for the depth analysis and determination of thin film properties by this non-destructive and contact-free laser technique will be discussed.

Analysis of Surface Roughness of Silicon Surfaces by Reflection Electron Energy Loss Spectroscopy

H.N. Frase, S.S. Wong, C.C. Ahn, and H.A. Atwater
MS 125-98
California Institute of Technology
Pasadena, CA 91125
(818) 395-2193, FAX (818) 395-2944.

The quantification of semiconductor surface roughness in the 0.5 - 10 nm range is a problem of current scientific and technological interest. Surface roughness measurements are also of great technological interest, particularly for silicon, since the starting surface roughness affects the roughness and ultimate quality of transistor gate dielectrics and other reacted or deposited layers. While atomic force microscopy and other scanning probe methods are now in widespread use for *ex situ* surface roughness evaluation, this is considerable interest in developing *in situ* methods for surface roughness measurement during growth or etching. Candidate *in situ* roughness analysis methods currently include reflection high energy electron diffraction (RHEED) and RHEED oscillations, widely used for monolayer roughness measurements, ellipsometry, and X-ray reflectivity. In this summary, we describe another method: the use of low-loss inelastic electron scattering measurements using reflection electron energy loss spectroscopy (REELS) to investigate silicon surface roughness.

We have investigated the effects of surface roughness on low-loss multiple inelastic scattering features, including surface and bulk plasmon scattering using silicon (001) surfaces prepared in four distinct ways: (i) a surface smoothened by epitaxial growth of 4.5 nm of silicon on a Si (100) substrate via molecular beam epitaxy (type I) , (ii) an as-received surface prepared with the manufacturer's polishing process (type II), (iii) a corrugated surface prepared by photolithography and anisotropic etching (type III) with a ridge width of the order of 100 μm, and (iv) a surface covered with square pyramidal peaks (type IV) of approximately 10 μm in width prepared by anisotropically etching a silicon substrate which had undergone mechanical abrasion with .25 μm diamond paste. Type III and type IV surfaces were created by anisotropically etching Si (100) substrates using a standard KOH-based solution[1], which etches (111) much more slowly than all others, yield structures bounded by (111) planes. Surface roughness was characterized using atomic force microscope (type I and II surfaces) and scanning electron microscope (type III and IV surfaces) images.

REELS spectra and RHEED patterns were collected simultaneously for all surfaces in a REELS-equipped molecular beam epitaxy system. Scattering was performed using a 25 keV electron beam incident along the [110] direction of the Si substrates, with a total beam current of 0.5-2 μA. RHEED patterns were recorded using video data acquisition with 8-bit resolution. The data reported here were taken between 22 and 118 mrad at various in-phase (specular reflected beam coincident with Bragg beam from Si bulk) and out-of-phase (specular beam located halfway between two Bragg beams from Si bulk) scattering conditions. The electron energy loss spectrometer is a second-order corrected magnetic prism

with a system resolution of approximately 5 eV.

Surface and bulk plasmon scattering are treated analytically using a modification of a standard model for low-loss scattering acquired in transmission geometry in which the intensities of the bulk plasmons are determined by a Poisson distribution[2]. Unlike the standard model, the modified model accounts for bulk plasmon scattering, surface plasmon scattering, and multiple scattering involving both surface and bulk plasmon scattering. The probability of any combination of surface and bulk plasmons was described by a multiplication of two Poission distributions. One distribution describes the surface plasmons which the other describes the bulk plasmons. The relative intensities of each multiple plasmon scattering is given by

$$I_{n,m} = IP_{n,m} = I(1/n!)(t_b/\lambda)^n exp(-t_b/\lambda)(1/m!)(t_s/\lambda)^m exp(-t_s/\lambda), \tag{1}$$

where n and m are the number of bulk and surface scattering events respectively, t_b and t_s are the average distances an electron travels while it is associated with creating bulk and surface plasmons respectively, and λ is the total electron mean free path. When $I_{0,0}$, the zero loss intensity, plus $I_{1,0}$ and $I_{0,1}$, the plasmon intensity in the single bulk and surface scattering approximations, are determined, then t_b/λ t_s/λ are known since

$$I_0 = Iexp(-t_b/\lambda)exp(-t_s/\lambda), \tag{2}$$

$$I_{1,0} = I(t_b/\lambda)exp(-t_b/\lambda)exp(-t_s/\lambda) = I_{0,0}(t_b/\lambda), \tag{3}$$

and similarly

$$I_{0,1} = I_{0,0}(t_s/\lambda). \tag{4}$$

The zero loss peak was represented as a gaussian with a FWHM of 5.0 eV, which was an artifact of the instrumental response. After the intensities for all plasmon combinations up to 92 eV were calculated, each plasmon was represented as a gaussian who's FWHM took into account the instrumental response and plasmon lifetime broadening effects.

The three variables $I_{0,0}$, $I_{1,0}$, and $I_{0,1}$ were used to fit all the data sets to find t_b/λ, and thus the bulk traveling distance, and t_s/λ, yielding the surface traveling distance. The type I surfaces have values of t_b/λ and t_s/λ which are larger than for other types of surfaces and are interpreted as being indicative of a smooth surface. The large t_b/λ is also consistent with grazing incidence reflection scattering from a smooth surface

Type II and III surfaces yield similar spectra and similar values of t_b/λ and t_s/λ, which are smaller than the values associated with the type I surface. The t_b/λ values are approximately 75% smaller while the t_s/λ are about 50% smaller. This indicates a similar order of roughness on each type of surface, and is indicative of nanometer scale roughness. Based on measurements of t_b/λ and t_s/λ both type II and III surface roughness are clearly distinguishable from type I surface roughness. We note that from the perspective of the incident electron beam, type II and type III surface should appear similar, as only the unetched flat tops of the faceted structures on type III surfaces, which are approximately 10 μm wide, are visible to the electron beam.

For the type IV surfaces, which consisted of arrays of anisotropically etched square pyramidal structures, t_b/λ is significantly greater than the t_s/λ. This difference in the relative traveling distances is consistent with the electron beam scattering from the square pyramidal structures at what is locally a high incidence angle (local angle is ≥ 25, as compared with macroscopic incidence angle of 1-5 °), thus resulting in significantly more bulk multiple scattering than surface multiple scattering.

The relative roughness length scales for types I-IV surfaces were also correlated with their respective RHEED patterns, as well as AFM and SEM images. The RHEED patterns of the type I surface consisted of Bragg rods, while types II-IV consisted of Bragg spots, indicating that qualitative RHEED observations are consistent with the REELS low-loss estimates of roughness. AFM images confirmed that type I surfaces are the smoothest. Like the low loss spectra, the RHEED patterns of the type II and III surfaces consisted of similar Bragg spot features, indicating similar roughness. The type IV surface contains the most distinct and circular Bragg spots, indicating that the majority of the incident beam underwent transmission instead of reflection scattering.

In summary, REELS low-loss inelastic scattering spectra can be used to deduce the average traveling distance of incident electrons, which is correlated with nanometer surface roughness. Large mean traveling distances and comparable bulk and surface plasmon intensities correlate with very smooth surfaces characteristic of growth by molecular beam epitaxy. Reduced mean traveling distances with comparable bulk and surface plasmon intensities correlate with surface exhibiting nanometer-scale roughness. Bulk plasmon scattering that is significantly larger than surface plasmon scattering correlate with very rough surfaces with high aspect ratio features 50-500 nm in size.

References

[1] W. Kern and C.A. Deckert, Ch V-1 in Thin Film Processes, J.L. Vossen and W. Kern, Eds., Acdemic Press, (1978).

[2] R.F. Egerton, "Electron Energy Loss Spectroscopy in the Electron Microscope" Plenum, New York, 1986.

[3] Z.L. Wang and J.M. Cowley, Surf. Sci. **193**, 501 (1988); Z.L. Wang and R.F. Egerton, Surf. Sci. **205**, 25 (1988).

[4] A. L. Bleloch, A. Howie, R. H. Milne and M. G. Walls, in "Reflection high-energy Electron Diffraction and Reflection Electron Imaging of Surfaces," P. K. Larsen and P. J. Dobson, Eds., NATO ASI, **188** (1990) 77.

[5] J. M. Cowley, in "Reflection high-energy Electron Diffraction and Reflection Electron Imaging of Surfaces," P. K. Larson and P. J. Dobson, Eds., NATO ASI, **188** (1990) 261.

Laser Surface Processing and Atomic Scale Analysis

MFB 10:30 am-12:00 m
Zia B & C

Richard Hall, *Presider*
Exxon Corporation

Sub-Monolayer Ablation of II-VI Semiconductor Surfaces

Peter Brewer, J.J. Zinck, and G.L. Olson
Hughes Research Laboratories, 3011 Malibu Canyon Road, Malibu, CA 90265.
Tel. (310) 317-5748, Fax (310) 317-5450.

and

M. Stuke
Max-Planck Institut für biophysikalische Chemie, Abteilung Laserphysik,
Am Fassberg, D-3400 Göttingen, Germany.
Tel. +49-551-201-338, Fax +49-551-201-330.

The pulsed laser ablation of compound semiconductors using above-bandgap radiation has been the subject of numerous experimental [1-4] and theoretical investigations [5]. Significant progress has been made in understanding the phenomenology of the ablation process, but many questions remain about the nature of the elementary ablation mechanism. It has recently been shown [5,6] that measurements of the velocity and angular distributions of particles ejected from the surface of a compound semiconductor during laser irradiation can be used to infer the energetics and dynamics of particle desorption, and thus provide useful information about the ablation mechanism. However, the interpretation of those experiments can be seriously complicated by the influence of near-surface collisions and changes in the surface structure and composition on the characteristics of the ejected particles. For example, multiple gas phase collisions have lead to inconsistencies between theoretical predictions [5] and experimental results [2] which show that the ejected products are characterized by translational temperatures that depend strongly on the angle and mass of the desorbed species. Likewise, the effect of surface damage on the behavior of the ejected particles may be manifested by non-stoichiometric and unstable yields, complex angular distributions, and flux characteristics arising from bulk diffusion processes.

In an attempt to identify a material system which can be used in developing a comprehensive model of the pulsed laser ablation of compound semiconductors, we have systematically studied the excimer laser ablation of a number of II-VI semiconductors, including CdTe [1,5], CdS [1] and HgCdTe; materials which exhibit some of the lowest ablation thresholds. Under low fluence laser ablation conditions the removal rates from these materials can be made sufficiently low to ensure that post-desorption collisions are minimal and their influence on the ejected particle dynamics can be neglected. In addition, we have demonstrated for CdTe, stoichiometric and atomically ordered surfaces can be maintained after multiple pulse ablation using nanosecond pulses over a limited fluence range. One important finding of this work is that the composition and structure of CdTe and CdS can be reversibly controlled by excimer laser irradiation;

i.e., damaged surfaces (non-stoichiometric surface composition and amorphous surface layers) can be removed and the surface restored to an ordered and stoichiometric condition by low fluence laser irradiation. These results are in sharp contrast to the ablation characteristics of other compound semiconductors in which irreversible damage to the surface occurs under all conditions above the ablation threshold.

In this paper we will discuss our work on the KrF excimer laser ablation of CdTe, CdS, and HgCdTe. Fluence-dependent changes in surface composition specific to each material system will be shown to be reversibly controlled by varying the laser fluence. A phenomenological model will be presented that treats the reversible, fluence-dependent composition changes in terms of the competition between the formation and desorption rates for each of the ejected species. The model also reveals the causes for non-reversible surface damage produced during laser ablation of a number of other compound semiconductors.

The remainder of the discussion will focus on results from CdTe that address issues related to changes to surface order and the velocity and angular distributions of ejected particles. Structural changes induced by the excimer laser irradiation of the CdTe (100) surface have been observed using Reflection High Energy Electron Diffraction (RHEED). These experiments reveal that under low fluence conditions above the ablation threshold highly ordered 2x1 reconstructed surfaces can be produced by multiple pulse exposure. However, under higher fluence conditions, the RHEED measurements indicate the formation of gross structural disorder in the near-surface region. A brief video of the RHEED data will be used to illustrate the real-time surface structure changes that are induced by various irradiation conditions and will demonstrate the differences between the mechanisms of sublimation and laser ablation in producing ordered surfaces.

Using time-of-flight mass spectrometry we have also investigated the velocity and angular flux distributions of the primary ablation products (Cd atoms and Te_2 molecules) from CdTe (100) and CdTe (211) surfaces using 248 nm nanosecond (FWHM 20 nsec, 7 nsec) and sub-picosecond (FWHM 600 fsec) laser irradiation [6]. The CdTe surfaces remain stoichiometric and atomically ordered during multiple pulse ablation with nanosecond pulses under low fluence conditions and yields of material removal are sufficiently low to ensure that multiple gas phase collisions can be neglected. Time-of-flight distributions for the ejected products are well-described by Maxwell-Boltzmann distributions for both low fluence nanosecond (<40 mJ/cm^2) and sub-picosecond (<4 mJ/cm^2) irradiation. Nascent angular flux distributions from nanosecond-ablated products are highly forward peaked about the surface normal under low fluence conditions and approach cosine distributions for high fluence irradiation. Angular flux distributions of products ejected from sub-picosecond irradiation are observed to follow a $\cos^3\theta$ form. These results will be used to support the conclusion that even though thermal effects contribute to the surface processes, non-thermal desorption pathways dominate much of the ablation phenomenon.

References

1. P.D. Brewer, J.J. Zinck, and G.L. Olson, Appl. Phys. Lett. 57, 2526 (1990). P.D. Brewer, J.J. Zinck, and G.L. Olson, Mat. Res. Soc. Symp. Proc. 201, 543 (1991).
2. A. Namiki, T.Kawai, and K. Ichige, Surf. Sci. 166, 129 (1986). A. Namiki, H. Fukano, T.Kawai, Y. Yasuda and T. Nakamura, J. Phys. Soc. Jpn. 54, 3162 (1985).
3. T. Nakayama, H. Ichikawa, and N. Itoh, Surf. Sci. 123, L693 (1982). N. Nakayama, Surf. Sci. 133, 101 (1983).
4. V.M. Donnelly, V. McCrary, and D. Brasen. Mat. Res. Soc. Symp. Proc. 75, 567 (1987).
5. R. Kelly, J. Chem. Phys. 92, 5047 (1990). R. Kelly and R.W. Dreyfus, Nucl. Instru. Meth. Phys. Res. B33, 341 (1988).
6. P.D. Brewer, M. Späth, and M. Stuke, Mat. Res. Soc. Symp. Proc. 334, 245 (1994).

THE SURFACE PREPARATION AND PHOTOCHEMISTRY OF CdTe(110)

P.J. Lasky, P.H. Lu, Y. Luo, R.M. Osgood Jr. and D.A. Slater*

Columbia Radiation Laboratory, Columbia University, New York, NY10027

*author to whom correspondence should be addressed.

1. INTRODUCTION.

Wide-band-gap II-VI compound semiconductors show great promise for the fabrication of LED's and lasers in the visible range [1]. In this paper we examine fundamental aspects of the processing of the surfaces of such materials, specifically the CdTe(110), surface, utilizing Electron Cyclotron Resonance (ECR) generated plasmas and laser-induced photochemical reactions.

ECR plasmas have significant advantages over other related plasma and ion based processes in that they operate at low pressure (10^{-3}-10^{-6} mbar) and produce chemically reactive species which are incident on the sample surface at low kinetic energy thus minimizing mechanical damage through sputtering processes. Such treatments have been shown to be capable of producing good quality surfaces of III-V semiconductor materials [2,3], this paper extends this methodology to II-VI materials.

We also present initial data from a study of the fundamental mechanisms underlying ultraviolet enhanced photochemistry on such surfaces. Many studies [4] have shown that the presence of a solid surface may enable the operation of reaction channels unavailable to the free molecule. Our combination of Time Of Flight (TOF) mass spectrometry with irradiation via tunable, pulsed lasers allows analysis of the kinetic energy of emitted photofragments as a function of photon frequency and is thus capable of providing detailed information on the microscopic mechanisms underlying surface enhanced photochemical processes [5]. This methodology is applied to a study of the model MOCVD precursor $(CH_3)_2Cd$ on the CdTe(110) surface.

2. SURFACE PREPARATION.

A comparison of XPS and Auger spectra of CdTe(110) surfaces cleaned by exposure to ECR generated hydrogen plasmas and by Ar^+ ion sputtering and annealing shows that both processes are capable of producing stoichiometric, contaminant free surfaces exhibiting the well ordered (1x1) periodicity characteristic of the (110) surfaces of compound semiconductors of the zinc blende structure.

Exposure of a clean CdTe(110) surface to an ECR generated oxygen plasma provides a facile means of growing an oxide overlayer. XPS spectra of both a clean surface and of a fairly thick (ca. 10ML) overlayer produced by this means are shown in figure 1.
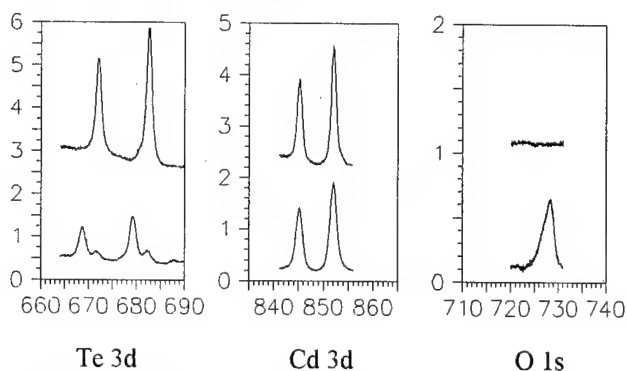

Te 3d   Cd 3d   O 1s

Figure 1 XPS spectra (kinetic energy) of clean (upper) and oxidized (lower) CdTe(110).

The ratio of the integrated peak intensities of Cd and Te 3d signals observed for such an overlayer are identical to those observed for a clean surface indicating that the 1:1 Cd:Te stoichiometry is preserved upon oxidation in contrast to many 'wet' chemical processes [6]. The shift in Te 3d peak position observed for the oxidized surface indicates the formation of a TeO_2 species as suggested by previous work

[7,8]. No shift in energy of the Cd 3d peak is observed upon oxidation; an affect attributable to the rather small chemical shifts typically observed for this feature [9]. However the fact that a Cd signal is observed at all for such a thick oxide overlayer indicates that oxide formation does not involve preferential Te segregation to form a TeO_2 overlayer and that cadmium is present in the overlayer in stoichiometric quantities possibly in the form of CdO.

Such oxide layers are stable under thermal annealing to at least 620K without a discernible change in stoichiometry. A substantial increase in order within the oxide layer upon annealing is however evident from a decrease in the FWHM of the Te 3d XPS peaks characteristic of the oxide layer.

As stated above, oxide layers may be easily and quantitatively reduced on the CdTe(110) surface by means of an ECR generated H plasma. Figure 2 illustrates the evolution of the XPS features characteristic of oxygen, cadmium, tellurium and tellurium oxide as a function of H plasma exposure time for such a process.
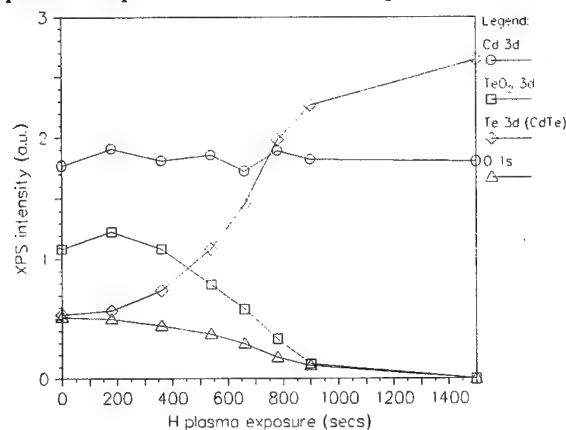
Figure 2. Evolution of XPS spectrum during H plasma cleaning procedure.

The extreme non linearity of the signals with plasma exposure is striking and indicates the operation of a reduction mechanism which produces hydrogen incorporation into the oxide lattice, probably in the form of tellurium and cadmium hydroxides, in the early stages of reduction with no net oxygen removal. This behavior has been observed over a wide range of oxide thickness and sample temperature.

3. SURFACE PHOTOCHEMISTRY.

Figure 3 illustrates the evolution of TPD spectra of $(CH_3)_2Cd$ from a clean CdTe(110) surface as a function of $(CH_3)_2Cd$ exposure at 80K. This indicates both that monolayer quantities of $(CH_3)_2Cd$ are weakly chemisorbed to the surface desorbing at ca. 245K and that further $(CH_3)_2Cd$ adsorption (for the first few layers at least) results in film growth in a well defined layer by layer fashion with the second layer desorbing at ca. 180K and subsequent multilayers at 170K.
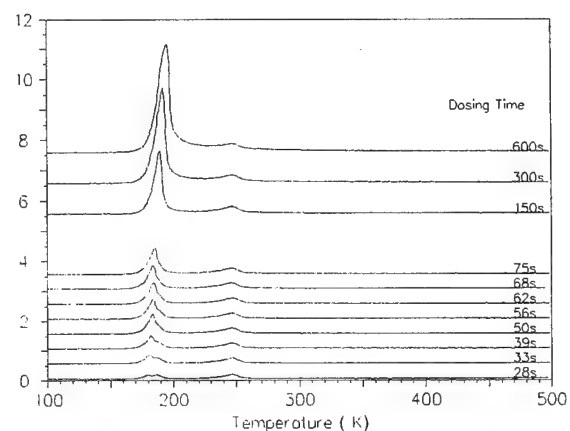

Figure 3. TPD spectra of $(CH_3)_2Cd$ with increasing coverage

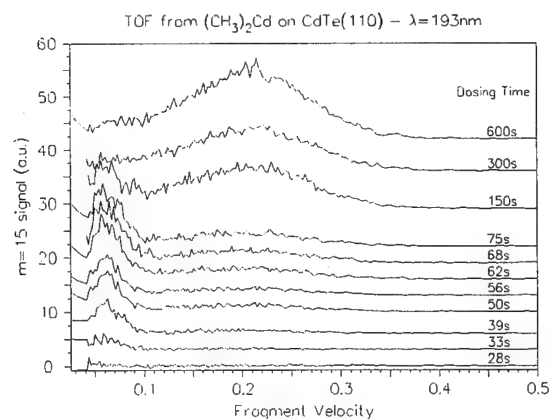**Figure 4.** Time of flight spectra as a function of increasing $(CH_3)_2Cd$ exposure

Figure 4 illustrates typical time of flight mass spectrometry data (m/z=15) obtained from such systems upon illumination with 193nm laser radiation. Two features with distinct kinetic

energies are evident which vary in relative intensity as a function of $(CH_3)_2Cd$ coverage.

Figure 5 shows the variation in these features when illuminated with 193 and 248 and 351nm radiation. Clearly the energy of the broad, fast peak is invariant with excitation frequency thus arguing against formation of this photofragment via a mechanism involving simple, direct photodissociation. The fact that this peak also persists to rather high coverages of $(CH_3)_2Cd$ where the molecular layers sampled by the TOF technique are spatially well removed from the substrate surface strongly suggests that the mechanism involved is characteristic of solid $(CH_3)_2Cd$ rather than specific to the CdTe surface.

At 1ML coverage no photoreaction products are observed due to efficient quenching of the intermediate excited ion states formed on irradiation due to proximity to the CdTe surface. However as shown in figure 4 as the thickness of the overlayer increases above 2-3 monolayers two TOF peaks due to photodissociation fragments are observed. Over a limited coverage range (~ 3-6 ML) a peak with a somewhat lower kinetic energy than that described above is observed. The fact that this feature is not observed for 'thick' adlayers suggests that the CdTe substrate may play a significant role in the underlying photochemical mechanism.
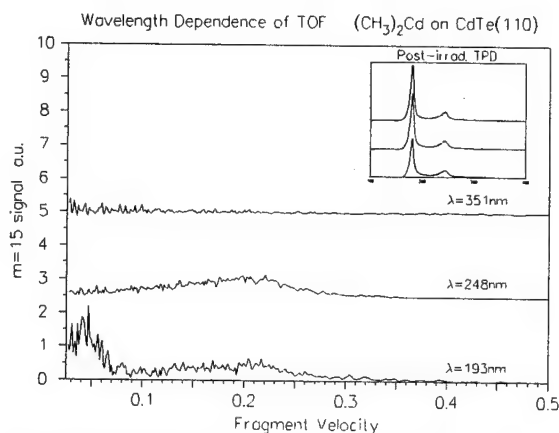

Figure 5. Relative intensity of observed time of flight features at different excitation frequencies.

The differing coverage and frequency dependencies observed for these two TOF features indicate the operation of two distinct reaction channels for the photodissociation of

$(CH_3)_2Cd$ adsorbed on CdTe(110). The likely microscopic origins of the mechanisms underlying these channels will be discussed with respect to direct photon absorption by and direct photodissociation of the adsorbed molecule, photon induced charge transfer within the adlayer and substrate photoabsorption with the subsequent dissociative attachment of photoemitted electrons to overlayer molecules.

4 REFERENCES.

1. Nurmikko A.V., Gunshor R.L. J.Luminescence 52 (1992) 89.

2. Takmori A., Sugata S., Askawa K., Miyauchi E., Hashimoto H. Jap.J.Appl.Phys. 26 (1991) L142.

3 Lu Z., Schmidt M.T., Chen D., Osgood R.M., Jr, Molder W., Poldlesnik D.V., Forster J. Appl. Phys. Lett. 58 (1991) 1143.

4 Polanyi J.C., Rieley H. in "Dynamics of the Gas-Surface interaction" (C.T.Rettner and M.N.R.Ashfold eds.) Royal Society of Chemistry (1991).

5 Yang Q., Osgood R.M., Jr J.Phys.Chem. 97 (1993) 8855.

6 Ricco A.J., White H.S., Wrighton M.S. J.Vac.Sci and.Tech. A2(2) (1984) 910.

7 Solzbach U., Richter H.J. Surf. Sci. 97 (1980) 191.

8 Werthen J.G., Haring J.P. Bube R.H. J.Appl.Phys. 54(2) 1983) 1159.

9 Handbook of Photoelectron Spectroscopy, Perkin-Elmer Corp. (1979).

REAL TIME MONITORING OF SURFACE REACTIONS DURING PLASMA PROCESSING

Masataka Hirose, Yasutoshi Miyoshi and Seiichi Miyazaki

Department of Electrical Engineering
Hiroshima University, Higashi-Hiroshima 724, Japan
(Tel: 0824-24-7655, FAX: 0824-22-7038)

Reacting silicon surfaces in contact with the glow discharge of SiH_4 or SiH_4+CH_4 have been studied by an FT-IR-ATR (Attenuated Total Reflection) technique. In the early stages of silicon film growth from a SiH_4 plasma at a substrate temperature of 200°C, SiH_2 is the major species on the surface, while at room temperature SiH_3 and $(SiH_2)_n$ chains are the dominant surface products. At a temperature of -95°C, polymerization reactions among adsorbates proceeds on the surface to form polysilane. At the beginning of silicon carbide deposition on a silicon film from a SiH_4+CH_4 plasma, the surface hydrogen bonds are scavenged by CH_3 radicals at room temperature, while they are stable at temperatures below -50°C.

1. Introduction

In situ or real time diagnostics of surface reactions in a reactive plasma is potentially important for atomic scale control of plasma deposition processes or dramatic improvement of step-coverage of a deposited thin film. Regarding gas phase reactions in a silane plasma the concentration of reactive species has been quantitatively measured[1]. Real time monitoring of surface reactions during plasma deposition from silane has been made by employing IR-RAS (Reflection Absorption Spectroscopy)[2] or ellipsometry[3]. In this paper we report on a newly developed FT-IR-ATR (Attenuated Total Reflection) system by which surface reactions in contact with a plasma can be directly probed. It is demonstrated that ATR sensitively detects the chemical bonding features of reacting surfaces and provides detailed information about surface reactions.

2. Experimental

A silicon or germanium crystal was used as the ATR prism, which was attached to a grounded electrode in a capacitively coupled PECVD reactor. As illustrated in Fig. 1, an infrared beam from an FT-IR spectrometer passed through a polarizer (P-polarized) and a BaF_2 window before entering the Si prism. Multiple internal reflections in the prism enabled us to probe surface chemical bonds whose vibrational spectra were obtained by a MCT detector. The resolution of ATR system was 4 cm^{-1} and the spectral data were obtained in 30 second or more. During PECVD, the flow rate of 3%SiH_4 diluted with H_2, the rf power density and the total pressure were kept at 90 sccm, 20 mW/cm^2 and 0.2 Torr, respectively. The deposition temperature was varied from 200°C to -95°C. The deposition rate of a Si thin film was estimated to be about 0.3 nm/min at room temperature and 200°C. For silicon carbide deposition, a gas mixture of CH_4:SiH_4: H_2=5:1:39 was used. The other conditions are basically similar to the case of silicon deposition except for the rf power density and the total pressure that was 40 mW/cm^2 and 0.25 Torr, respectively.
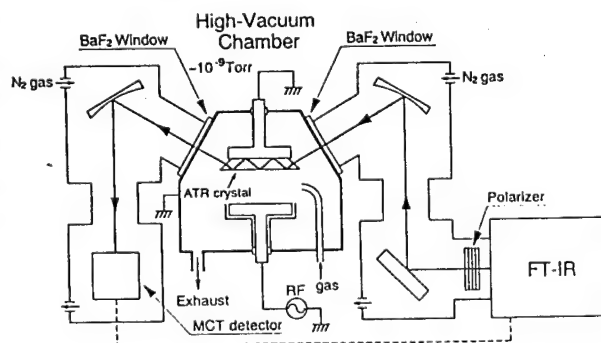

Fig. 1 Schematic of an FT-IR-ATR system for monitoring surface reactions in a UHV chamber.

3. Results and Discussion

3.1 H/D Exchange Reaction

An H-terminated Si(111) surface is exposed to a D_2 plasma in order to examine the submonolayer sensitivity of ATR and to monitor the exchange reaction of surface SiH bonds with deuterium. The intensity of the optical absorption due to the SiH stretching vibration at 2083 cm^{-1} is decreased by the D_2 plasma exposure. Correspondingly, the absorption peaks due to SiD_X (X=1,2,3) appear. The SiD bond absorption at 1512 cm^{-1} is predominant at 0.2 seconds exposure to a deuterium plasma. Further exposure of the H-terminated surface results in increasing number of SiD_2 (1533.5 cm^{-1}) and SiD_3 bonds (1550 cm^{-1})[4] presumably because the deuteration reaction of SiH bonds on the top surface is followed by further deuteration of the Si backbonds at SiD sites. As the exposure time increases, the decrease of SiH_X (mainly X=1) bonds is accompanied with the corresponding increase of the SiD_X absorption, showing that H/D exchange reaction proceeds on the top surface and also backbonds of surface Si atoms are partially deuterated. A few seconds of D_2 plasma exposure are enough to completely deuterate a monohydride terminated surface at room temperature.

3.2 Silicon Deposition Kinetics

ATR spectra due to SiH_X bonds on silicon deposition surfaces during PECVD are shown in Fig. 2. The time indicated for each of spectra denotes the period needed for the cumulative spectral measurements. In the early stages ($\leq$ 30 s or 0.15 nm thick layer) of the silicon film growth at 200°C the absorption due to the stretching modes of SiH_3 and $(SiH_2)_n$ molecular units are observable around 2140~2120 cm^{-1}. The absorption due to the surface SiH_2 vibration is increased with deposition time as a consequence of hydrogen desorption reaction at this temperature. Taking into account the fact that SiH bonds are mainly incorporated in the bulk hydrogenated amorphous silicon (a-Si:H) films grown at 200°C, it is likely that silicon network formation reaction in the near-surface region is not completed. This is basically consistent with a previous result of IR-RAS[2]. At room temperature, a significant absorption due to $(SiH_2)_n$ chains and SiH_3 bonds is clearly observed in the early stages of the growth ($\leq$ 30 s), reflecting the reduction of thermal desorption reactions of bonded hydrogen in the near-surface region. The H/D exchange reaction after silicon deposition at room temperature also reveals the hydrogen bonding features on the top surface even for a relatively thick film as shown in
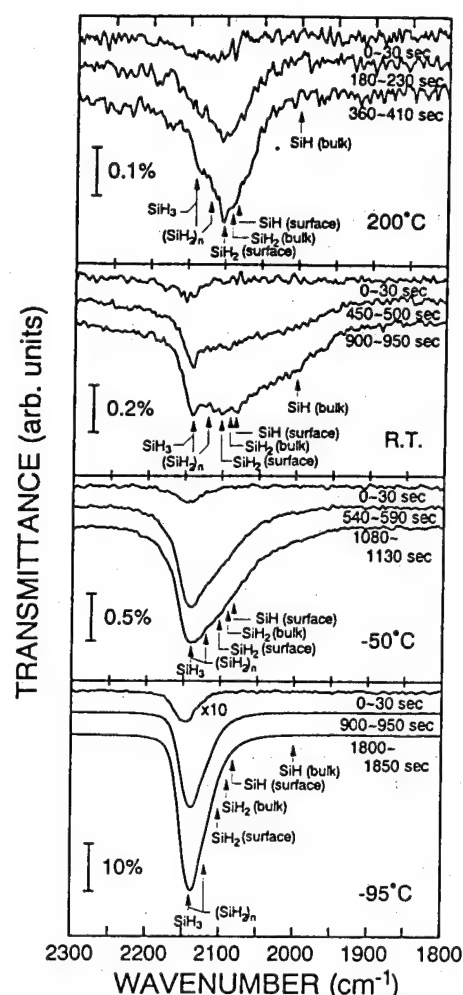

Fig. 2 P-polarized ATR spectra of surfaces of ultra-thin silicon films at different substrate temperatures. The times indicated in the figure refer to sampling time for data acquisition.
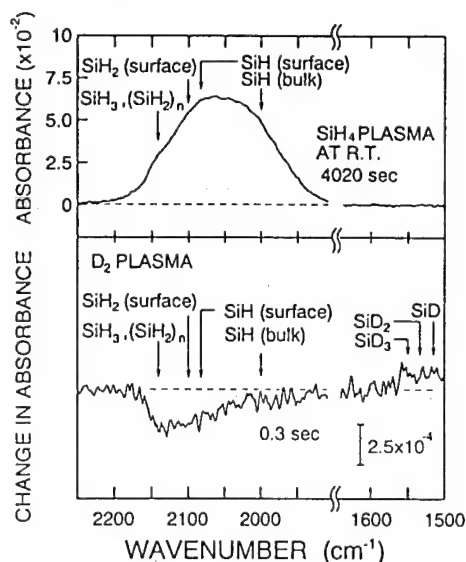

Fig. 3 H/D exchange reaction on a silicon surface after 4020 sec deposition.

Fig. 3. Significant reduction of $(SiH_2)_n$ chains, SiH_3 and SiH_2 bonds by deuteration for 0.3 seconds clearly shows the existence of such molecular units on the top surface.

By lowering the deposition temperature to $-50\,°C$ or $-95\,°C$, optical absorption due to $(SiH_2)_n$ chains and SiH_3 units are predominant from the beginning of the deposition and even after long time film growth. Particularly at $-95\,°C$, the absorption band due to $(SiH_2)_n$ chains terminated with SiH_3 is only observed during the film growth and the absorption intensity is increased by a factor of about 20 as compared to that at $-50\,°C$. This agrees very well with the result of a previous paper[5], where silicon film growth rate from a silane plasma dramatically increases at temperatures below $-84\,°C$ and the deposited films consist of the $(SiH_2)_n$ chains terminated with SiH_3 which are a typical structure of polysilane.
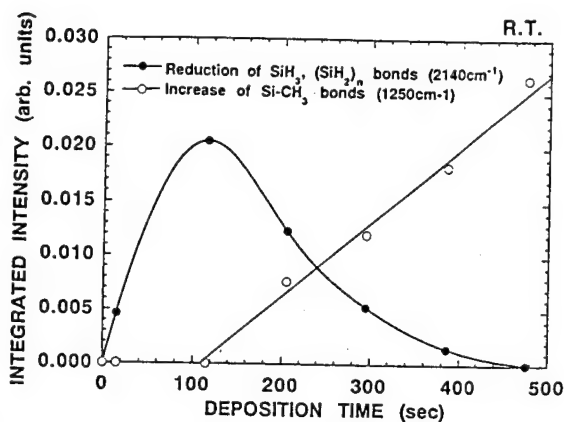

Fig. 4 Intensity of SiH_3 + $(SiH_2)_n$ and Si-CH_3 as a function of deposition time. There is a reduction of SiH_3 and $(SiH_2)_n$ bonds at the same time as the number of Si-CH_3 bonds increase.

3. 3 Silicon Carbide Growth on Silicon

A hydrogenated silicon carbide (a-SiC:H) film was deposited at room temperature on a 5 nm thick hydrogenated amorphous silicon (a-Si:H) layer. When a CH_4+SiH_4+H_2 plasma was turned on for a-SiC:H deposition, the stretching absorption at 2140 cm^{-1}, which arises from SiH_3 and $(SiH_2)_n$ bonds on a-Si:H surface, is significantly reduced. Also, the absorption due to Si-CH_3 at 1250 cm^{-1} is not observable. The extent of hydrogen bond reduction on a-Si:H surface and the absorption intensity due to Si-CH_3 bonds are compared in Fig. 4. Note that the reduction of hydrogen bonds on a-Si:H does not occur in the case that the surface is exposed to a silane plasma. Therefore, the result of Fig. 4 indicates that CH_3 radicals attack the surface hydrogen bonds on a-Si:H at the beginning of a-SiC:H deposition and scavenge hydrogen by a reaction such as CH_3+H (surface) → CH_4. As the deposition time exceeds 100 seconds, Si-CH_3 bonds become observable, showing the carbonization of a-Si:H surface and subsequent a-SiC:H growth. Apparent recovery of reduced SiH_3 and $(SiH_2)_n$ bonds (2140 cm^{-1}) at the a-Si:H/a-SiC:H interface is caused by the increase of absorptions due to SiH_2 and C_Y:SiH_X (Y=1,2, X=1,2) bonds on a-SiC:H surface and in the bulk whose absorption tails overlap the 2140 cm^{-1} band.

Conclusions

Chemical bonds on a growing film surface in a silane plasma have been sensitively probed by real-time ATR spectroscopy at substrate temperatures ranging from 200°C to -95°C. Dramatic change in surface reaction is observable by lowering the substrate temperature. CH_3 radicals in a CH_4+SiH_4 plasma preferentially scavenge hydrogen bonds on a-Si:H surface and carbonize it at the beginning of the silicon carbide growth.

References

1) N. Itabashi, N. Nishiwaki, M. Magane, S. Naito, T. Goto, A. Matsuda, C. Yamada and E. Hirota: Jpn. J. Appl. Phys. 29 (1990) L505.
2) Y. Toyoshima, K. Arai, A. Matsuda and K. Tanaka: Appl. Phys. Lett. 56 (1990) 1540.
3) N. Blayo and B. Drevillon: J. Non-Cryst. Solids 137&138 (1991) 771.
4) V. A. Burrows, Y. J. Chabal, G. S. Higashi, K. Raghavachari and S. B. Christman: Appl. Phys. Lett. 53 (1988) 998.
5) H. Shin, S. Miyazaki and M. Hirose: J. Non-Cryst. Solids 137&138 (1991) 713.

ATOMIC LAYER GROWTH OF SiO$_2$ ON Si(100) USING SiCl$_4$ AND H$_2$O IN A BINARY REACTION SEQUENCE

Ofer Sneh, Michael L. Wise[a] and Steven M. George
University of Colorado, Department of Chemistry and Biochemistry, Boulder, CO 80309.
[a]Present address: AT&T Bell Lab, Rm. 1B-213, 600 Mountain Ave., Murray Hill , NJ 07974.

Future silicon microelectronics technology will require nanoscale components to achieve ultra large scale integration. The reduction to nanometer scale sizes will be dependent on processing that can be controlled at the atomic level and conformally deposit into high aspect ratio structures. The Si/SiO$_2$ interface is central in silicon technology. Controlled and conformal deposition of SiO$_2$ dielectric layers will be crucial for the fabrication of MOS gate oxides as thin as 50 Å and high aspect ratio trench capacitors in DRAM. Both requirements can be inherently achieved by the technique known as atomic layer epitaxy (ALE)[1] or atomic layer processing (ALP) if the deposited film is not epitaxial.

Atomic layer epitaxy (ALE) is based on a repetitive application of two different reactions with two different reactants, A and B. Both reactions passivate the surface after the deposition of one monolayer or less. The A reactant reacts with the surface species deposited by the B reaction and vice versa. The role of the surface chemistry is dominant in determining the chemical vapor deposition using ALE or ALP schemes. The optimization of the deposition is based on the kinetics of the A and B reactions and the desorption kinetics of the surface species left after each reaction.

A binary reaction for the deposition of SiO$_2$ is SiCl$_4$ + H$_2$O $\rightarrow$ SiO$_2$ + HCl. This reaction can be separated into the following two half reactions:

(A) SiOH + SiCl$_4$ $\rightarrow$ Si-O-SiCl$_3$ + HCl

(B) SiCl + H$_2$O $\rightarrow$ SiOH + HCl
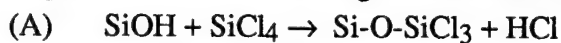
In this study we have demonstrated the applicability of this deposition scheme using ABAB... binary reaction sequence. We also have evidence that the deposition per AB cycle is affected by the thermal stability of the surface hydroxyl species left after the completion of the B reaction. The experiments were performed in a UHV chamber (2-5x10^{-10} Torr). Experiments at pressures as high as 1 Atm. were performed *in-situ* in a small internal high pressure chamber (IHPC)[2]. The two main experimental techniques employed in these investigations were temperature programmed desorption (TPD) and laser induced thermal desorption[3] (LITD).

Film growth experiments were performed inside the IHPC. High pressures of H$_2$O (up to 20 Torr) and SiCl$_4$ (1-50 Torr) were introduced into the IHPC and allowed to react for a given time and then evacuated. A clean Si(100) 2x1 surface was initially exposed to 100 L of SiCl$_4$ at 300K to saturate the chlorine coverage on the surface. Following the first SiCl$_4$ reaction (designated - A1), the first H$_2$O reaction, (B1), was performed at 600-680 K and 10 Torr. The reaction reached saturation in less than 10 minutes at 600K and less than 1 minute at 680K as determined by a complete loss of the surface chlorine species and the saturation of the oxygen coverage. Similar parameters for subsequent B2 and B3 reactions were also sufficient for complete reactions. The next A reaction (A2) was performed at 600-680 K and a pressure of 10-50 Torr. This reaction saturated in approximately 20 min at 600K and less than 1 minute at 660K when the chlorine coverage reached its maximum value. These same parameters for the A2 reaction were sufficient for a complete A3 reaction.

Following the reactions performed in the IHPC, the surface chlorine coverage was used as a measure for the completion of the first three A and B reactions. Chlorine coverages were

obtained from LITD signals of $SiCl_2$[4]. The total oxygen coverage was determined from SiO TPD signal. This procedure is accurate since SiO desorption is the only channel for oxygen desorption. The integrated SiO mass signals were calibrated by comparison with the SiO signal obtained from a H_2O saturation exposure on Si(100) 2x1. This H_2O exposure is known to deposit an oxygen coverage of $\theta_O = 0.5$ ML. The stoichiometry of the SiO_x film was qualitatively obtained from the AES spectra.

The results of the first three AB reactions are summarized in Fig. 1. In this figure, the chlorine coverage after reaction with $SiCl_4$ is given relative to the first $SiCl_4$ dose. This chlorine is then removed by the H_2O reaction when oxygen is deposited on the surface. The same behavior was observed for the subsequent AB cycles. Up to 10 AB cycles were employed. The oxygen coverage as a function of the number of AB cycles is summarized in Fig. 2. The first and second AB cycles deposit about 1.8 ± 0.2 and 1.2 ± 0.8 ML of oxygen, respectively. The following AB cycles deposit a constant amount of oxygen per AB reaction cycle of 0.73 ± 0.05 ML per AB cycle.

The ABAB... deposition was compared to H_2O thermal oxidation. Oxidation with H_2O at 600-700 K quickly reaches an apparent saturation coverage of about 2 ML of oxygen. In contrast, the ABAB... binary reaction chemistry continues to deposit a constant amount of oxygen with every AB cycle. AES experiments have indicated the growth of stoichiometric SiO_2 on the surface. The thicknesses of the films were estimated using the density of vitreous silica. The growth rate in the constant growth region occurring after ≥ 3 AB cycles is estimated to be 1.1 Å per AB cycle.
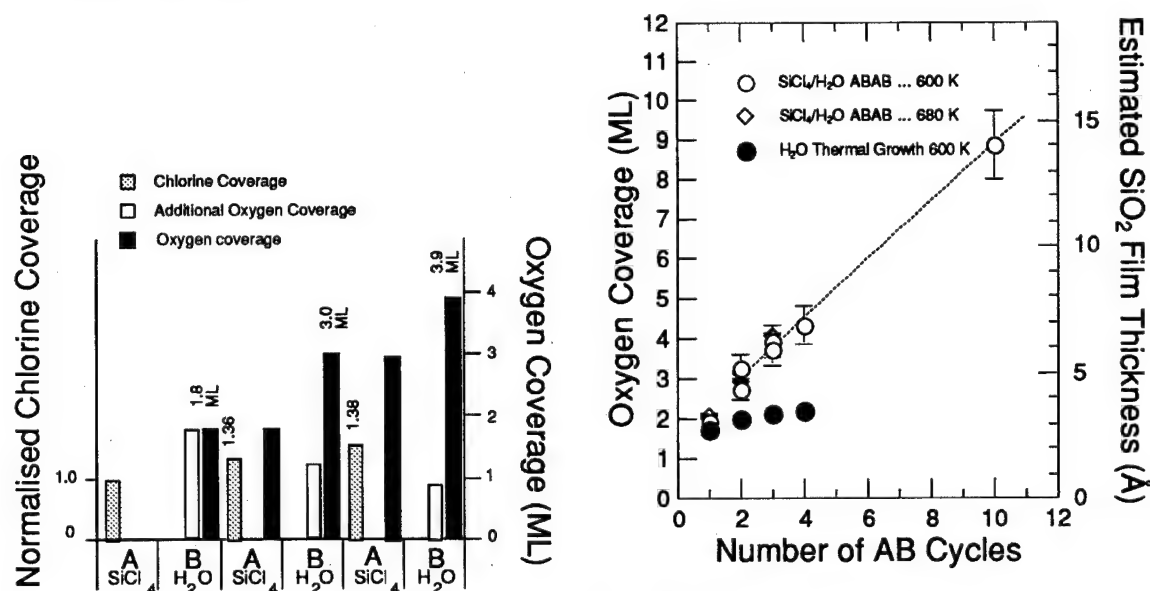

Fig. 1: The first three AB cycles

Fig. 2: SiO_2 deposition for 1-10 AB cycles. A comparison is made with H_2O thermal oxidation.

The mechanism of reaction B is interpreted as a reaction of Si-Cl + $H_2O \rightarrow$ Si-OH + HCl[5]. The $SiCl_2$ LITD results indicate that chlorine is completely removed by the B reactions. AES spectra also detect no chlorine in the films. Reaction A is more complicated and $SiCl_4$ molecules may react with one two and even three Si-OH groups[5]. The probability of these single, double and triple reactions may be a function of the hydroxyl groups coverage.

The maximum number density of hydroxyl groups on a silica surface is $4.6 \times 10^{14}/cm^2$ and the equilibrium silanol coverage decreases at higher temperatures[6]. We have studied the thermal stability of hydroxyl groups on a flat, annealed silica surface. Our results displayed at Fig. 3 are consistent with the literature results on high surface area silica surfaces[6,7]. The expected surface hydroxyl coverage at 600 K is about $2.67 \pm 0.14 \times 10^{14}/cm^2$. In good agreement, the oxygen deposition of 0.73 ± 0.05 ML per cycle is consistent with a silanol number density of $\approx 2.52 \pm 0.17 \times 10^{14}/cm^2$. This correspondence suggests that the SiO_2 deposition by the binary ABAB... reaction sequence chemistry is probably determined by the thermal stability of the surface hydroxyl species.
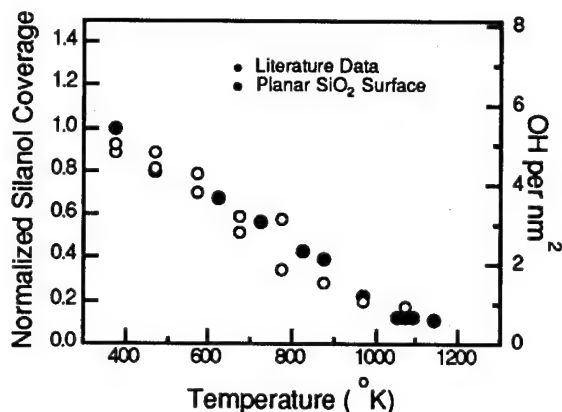

Fig. 3: Thermal stability of hydroxyl surface species on silica.

The binary reaction sequence chemistry is limited to the temperature range of 600-700K. Below 600K reaction B did not proceed to remove all the surface chlorine. At temperatures higher than 700K, thermal oxidation of silicon may result during the B reaction. This H_2O oxidation will alter the superior thickness control and conformality expected from the binary reaction sequence chemistry.

REFERENCES

1. C. H. L. Goodman and M. V. Pessa, J. Appl. Phys. **60**, R65 (1986).
2. O. Sneh and S. M. George, Submitted to J. Vac. Sci Technol. A.
3. S. M. George, in *Investigations of Surfaces and Interfaces* Part A, Eds. B. W. Rossiter and R. C. Baetzold, Physical Methods of Chemistry Series 2nd ed., Vol. IXA. John Wiley & Sons 1993, Chap. 7, p. 453.
4. P. Gupta, P. A. Coon, B. G. Kohler and S. M. George, J. Chem. Phys. **93**, 2827 (1990).
5. J. B. Peri and A. L. Hensley, J. Phys. Chem. **72**, 2926 (1968).
6. R. K. Iler, *The Chemistry of Silica*, 2nd Ed. Wiley, New-York (1979), Chap. 6.
7. O. Sneh and S. M. George, Submitted to J. Phys. Chem.

Optical and Electronic Properties of Nanostructures

MSaA 8:30 am-10:00 am
Zia B & C

Harry Atwater, *Presider*
California Institute of Technology

Optical Properties of Silcon Nanoclusters

Louis E. Brus
AT&T Bell Laboratories
Room 1A-256
600 Mountain Avenue
Murray Hill, NJ 07974

Summary not available.

A Silicon Solid-State LED: Long-Lived Visible Electroluminescence from Silicon Nanocrystallites

T. A. Burr, Department of Materials Science and Engineering, Room 13-5146, Massachusetts Institute of Technology, 77 Massachusetts Avenue, Cambridge, MA 02139
Phone: (617) 253-6924; FAX: (617) 258-6749; and
K. D. Kolenbrander, Department of Materials Science and Engineering, Room 13-5049, Massachusetts Institute of Technology, 77 Massachusetts Avenue, Cambridge, MA 02139
Phone: (617) 253-3365; FAX: (617) 258-6749

We have constructed and characterized visible electroluminescent devices based on Si nanocrystallite thin films. The key to stable electroluminescent emission is the nature of the Si surface capping layer, which determines the efficiency and stability of the devices. The layers must be transparent to the emitted light, provide sufficient electrical contact to insure carrier transport to the active layer, stabilize the Si surfaces to prevent chemical and electrical degradation, and passivate the dangling surface bonds which would act as non-radiative recombination centers and quench emission. Our devices use Al and ITO (indium tin oxide) electrodes, as well as transparent polymer capping layers to provide the necessary carrier injection and chemical and electronic passivation for the silicon nanocrystallite active layer. Their electrical and optical behavior was evaluated in terms of the I-V characteristics, electroluminescence spectra, and photoluminescence spectra. These devices represent a first step towards developing efficient silicon based light-emitting technology.

Thin films of Si nanocrystallites were deposited using a pulsed laser ablation supersonic expansion source. Discrete packets of Si nanocrystallites were entrained in the He carrier gas of the source. Nanocrystallites were deposited on a substrate placed in the beam line. Substrates can be varied according to characterization or device requirements. For this work, patterned indium tin oxide (ITO) on glass substrates were used.

Our simplest device is a three-layer construction which consists of Si nanocrystallites sandwiched directly between high and low work function materials which act as hole and electron injecting contacts, respectively. Positive and negative carriers are injected into the light emitting nanocrystallite region, where they either recombine or pass through to the electrode of the opposite charge. Device fabrication begins with a glass substrate coated with strips of ITO 2 mm wide and ~200 nm thick. The ITO acts as the hole-injecting electrode. A self-supporting nanocrystallite thin film (20-100 nm thick) is then deposited onto the patterned ITO substrate. Vacuum evaporation of a top electrode of aluminum lines (2 mm wide, 90-200 nm thick) placed perpendicular to the ITO strips results in a matrix configuration in which each of the 2 mm x 2

mm active devices ("pixels") can be addressed individually. Silver paint is used for contact between electrodes and external wires.

In an attempt to enhance the emission efficiency of our three-layer device we improved the nanocrystallite-electrode contact by inserting a conducting polymer as a fourth layer between the hole-injecting ITO electrode and the Si nanocrystallite active layer. A four-layer device was fabricated using poly(N-vinyl carbazole) (PVK), a transparent polymer with hole transport properties. PVK films were spun cast from tetrahydrofuran (THF) solution onto the patterned ITO substrate prior to Si nanocrystallite deposition.

We expected that further enhancement would be seen by improving the electron injection into the active layer as well. Consequently, a fifth layer was introduced between the emissive layer and the metal electrode of the four-layer system. The additional layer served to confine carriers within the nanocrystallite emitter layer, enhance electron injection, and inhibit exciton migration to the metal contact. The fifth layer was a molecular semiconductor, 2-(4-biphenylyl)-5-(4-*tert*-butylphenyl)-1,3,4-oxadiazole (butyl PBD), in an insulating matrix of poly (methyl methacrylate) (PMMA).
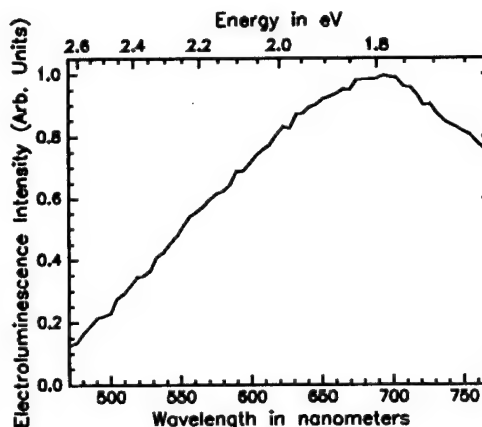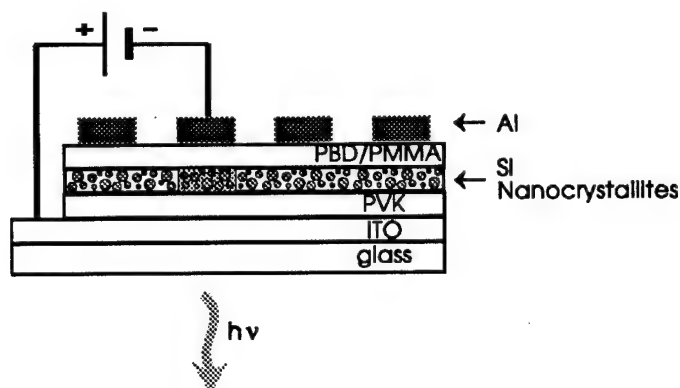
The electroluminescent emission from the three-layer devices appears yellow-orange in color and is clearly discernible with dark adapted eyes. While ramping the applied bias, the yellow orange light becomes visible at ~15 V. Light emission became more intense with increasing applied voltage. The three-layer devices had very short lifetimes, lasting only minutes before failure. Four- and five-layer devices constructed with intervening polymer layers exhibit significantly brighter luminescence and longer lifetimes than devices with only ITO and metal contacts. The 5-layer devices showed greater emission intensity than the 4-layer devices. The device had a turn-on voltage of ~6 V under forward bias. Electroluminescent intensity increased

slowly with increasing bias up to ~30 V whereupon the pixel failed. Failure was due to Joule heating of the resistive nanocrystallite films, leading to sparking and degradation of the Al films.

Long device lifetimes were observed in the four- and five-layer systems. Light emission has lasted for hours and appears to last indefinitely. These devices have the advantage of being robust -- they can be stored and operated in normal room air and emit visible light at room temperature. Luminescence efficiency and stability are significantly improved in devices containing polymer layers. This improvement is presumably caused by a more extensive, uniform electrode coverage and a resultant increase in the contact area. These two factors contribute to reduce the potential drop across the nanocrystallite layer and to produce more efficient carrier injection. After storage in air for several weeks, the devices exhibit only slightly weaker electroluminescence intensity. This decrease in efficiency is thought to be to due to humid air degrading the polymer contacts.

In summary, multilayer electroluminescent devices have been developed as a first step in developing useful light emitting applications. The devices produce visible light with spectra similar to the photoluminescence emission observed from the Si nanocrystallite thin films. The silicon layer serves as the active layer for the devices and visible light emission has its origin in the recombination of quantum confined carriers in the nanocrystallites. The emission efficiency and device lifetime were greatly enhanced by the addition of polymer hole and electron transport layers. Although further analysis regarding electrical, optical, and interfacial properties of these multilayer devices is necessary, this work indicates that Si based nanostructures have a strong potential for future exploitation in optoelectronic technologies.

STM Imaging of Electron Scattering and Confinement
at Metal Surfaces

Phaedon Avouris,
IBM Research Division, T.J. Watson Research Center
Yorktown Heights, NY 10598
Phone: (914) 945-2722 / Fax: (914) 945-3715

Electrons in Shockley-type metal surface states act as a quasi-two-dimensional free-electron gas (2DFEG). We show that scanning tunneling microscopy (STM) and spectroscopy (STS) can be used to study the interactions of this 2DFEG with features such as individual steps and adsorbed or embedded atoms[1,2]. Two approaches were utilized in our studies. One is based on the fact that an incident surface electron-wave when partially reflected by localized potentials such as those produced by steps, can interfere with the incident wave. This interference leads to an oscillatory local density-of-states near the step. Such oscillations were observed in dI/dV maps of Au(111) and Ag(111) surfaces. From dI/dV images as a function of the bias voltage the dispersion of the surface states and the scattering phase-shifts were obtained. Point-defects lead to isotropic scattering which appears in the form of concentric circles surrounding the defect. Because of the finite penetration depth of the surface state, not only adsorbed but also ebbeded species were found to act as scatterers. The electron oscillations observed at 300K decay exponentially as a function of the distance from the scatterer. We attribute this to the temperature-dependent Δk-width of the STS measurement which leads to the dephasing of the thus formed wave-packet. Another approach we used to study the interactions of the 2DFEG involves the spectroscopy of the onset region of the surface state band as a function of the distance from the scatterer[2]. In this way, the range of strong perturbation of the surface state was estimated to be 15-20 Å, and evidence was found for defect-induced bulk-surface state mixing.

Since steps act as barriers to surface electrons, they can be used to confine them and form lower-dimensionality structures[3]. We have studied two types of such structures: (a) Quasi-one-dimensional structures provided by narrow terraces at stepped surfaces, and (b) quasi-zero-dimensional structures provided by metal islands. In both cases we have been able to observe discrete quantum states, image their probability distributions and obtain their spectra at 300K. The implications of these findings on surface dynamical processes will be discussed.

1. Y. Hasegawa and Ph. Avouris, Phys. Rev. Lett. **71**, 1071 (1993); Ph. Avouris et al., J. Vac. Sci. Technol. B **12**, 1447 (1994).

2. Ph. Avouris and I.-W. Lyo, to be published.

3. Ph. Avouris and I.-W. Lyo, Science **264**, 942 (1994).

Single Nanocrystal Spectroscopy by Two Photon Excitation

Sean. A. Blanton, Ahmad Dehestani, Peter C. Lin,
and Philippe Guyot-Sionnest

The James Franck Institute
The University of Chicago
5640 S Ellis Ave
Chicago, IL 60637

Current methods of semiconductor nanocrystal synthesis produce samples which are nearly monodisperse in size. The remaining polydispersity in size, along with possible variations in surface configuration, still introduce an inhomogeneous broadening to most spectroscopic studies. In an effort to eliminate this broadening, we perform spectroscopy on single nanocrystals.

We do this by two-photon excitation microscopy[1] which relies on a tightly focused laser to produce luminescence in a region of roughly one cubic micron. We are also able to scan the laser focus in two-dimensions. While two-photon microscopy excitation is not new, we are not aware that it has been previously applied to the study of single molecules or nanocrystals.

We synthesize CdS (55Å diameter) and CdSe (28 and 43Å) nanocrystals according to the literature[2,3]. The CdS nanocrystals are imbedded in a glycerin/water glass and the CdSe in a glass-forming branched alkane. The liquid samples are attached to a microscope objective and immersed in a He vapor cryostat. Most spectra are taken at 5K.

We observe the published one-photon excited large-ensemble emission spectra[2] at high concentrations of CdS, multiple peaks at intermediate concentrations, and single lines at low concentrations. The width of the lines is ≈3nm or 15meV. No evidence of phonon emission is detected. The concentration of nanocrystals in the sample is known to be greater than can be accounted for by the observed number of spectral features, and the intensity of the features is seen to vary with time.

The CdSe nanocrystals did not yield long-lived, well defined features. The difference in behavior might be explained by different trapping mechanisms between the CdS and CdSe nanocrystals as previously described[4,5].

Our detection level for CdS is consistent with a model previously proposed in which there exists a shallow "trap" state and for which thermal excitation back to the fluorescing state is allowed. For CdSe, an LO phonon progression has been seen in small ensembles and a longer fluorescence decay time than CdS measured. By employing the Huang-

Rhÿs coupling scheme one sees that for CdS, a shorter fluorescence decay time is consistent with weak LO phonon coupling. The width of the emission line is consistent with the estimated trapping time.

Two-photon excitation microscopy is spatially selective in all three dimensions and should provide a powerful complement to the booming field of single molecule/nanocrystal studies. The technique's ability to probe the interior of solids and scan in all three dimensions is a trait lacking in the NSOM.

We have obtained emission linewidths of 15meV. This is the most narrow yet reported for CdS and probably indicate that the homogeneous linewidth for electron-hole recombination is due to the trapping time. We are currently using two-photon excitation microscopy to obtain excitation spectra of nanocrystals and to expand our studies to include dyes and other fluorophores.

References

1. W. Denk, J. H. Strickler, W.W. Webb, *Science* **248**, 73 (1990)
2. L. Spanhel, M. Haase, H. Weller, A. Henglein, *J. Am. Chem. Soc.* **109**, 5649 (1987)
3. C.B. Murray, D.J. Norris, M.G. Bawendi, *J. Am. Chem. Soc.* **115**, 8706 (1993)
4. A. Eychmüller, A. Hässelbarth, L. Katsikas, H. Weller, J. Lumin. **48 & 49**, 745 (1991)
5. M.G. Bawendi, P.J. Carroll, W.L. Wilson, L.E. Brus, J. Chem. Soc. **96**, 946 (1992)

Figure Captions

1. The emission spectra of a single 55Å diameter CdS nanocrystal compared with that of a large ensemble. The large ensemble spectrum is not to scale.

2. A double-peak emission spectra which may arise from a single CdS nanocrystal

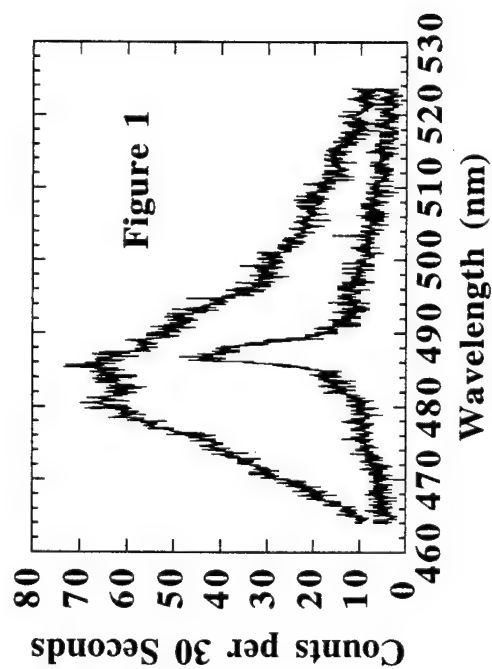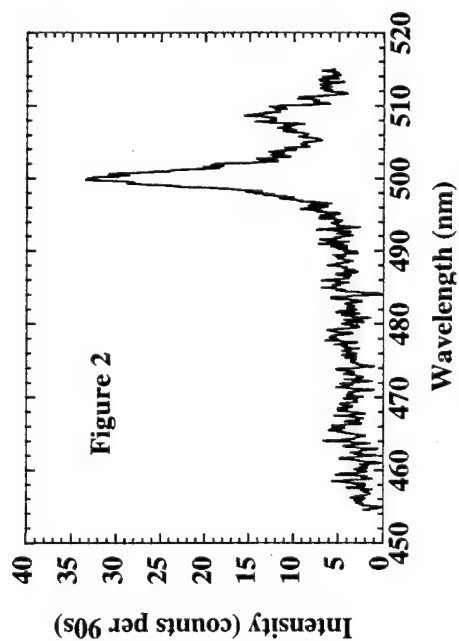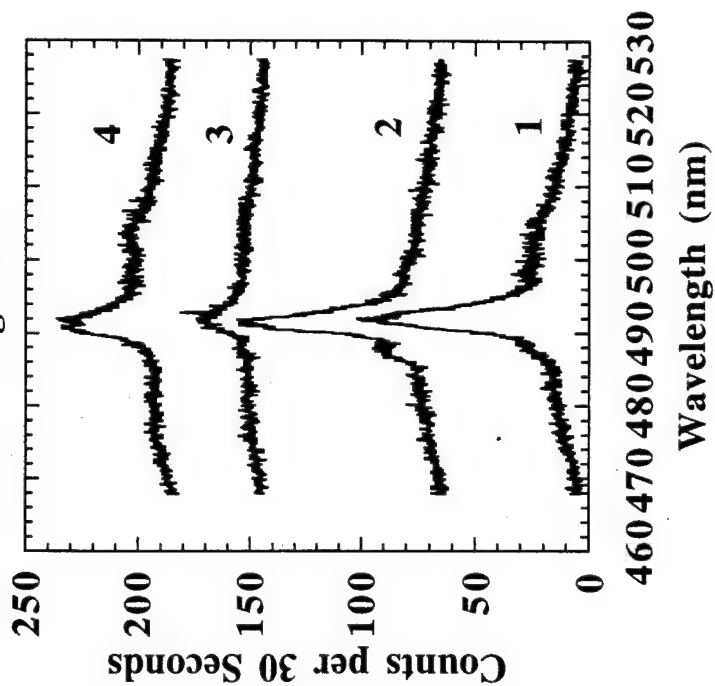3. Emission spectra recorded at successive 30 second intervals

Figure 3

Figure 1

Figure 2

Electronic Structure and Light Emission from Nanostructures

MSaB 10:30 am-12:00 m
Zia B & C

Masataka Hirose, *Presider*
Hiroshima University, Japan

Obtaining Bulk Electronic Structure with Atomic Resolution
Using Spatially Resolved Electron Energy Loss Spectroscopy

Philip E. Batson
IBM Thomas J. Watson Research Center
P.O. Box 218
Yorktown Heights, New York 10598
Tel: (914) 945-2782
Fax: (914) 945-4001

Recently, it has been shown that higher performance within the silicon-based technology can be obtained by using Si-Ge alloys in both strained and unstrained configurations. For instance, very high electron mobilities can be obtained in a strained Si quantum well structure formed by CVD deposition of Si on a relaxed $Ge_{30}Si_{70}$ substrate. [1] In addition, there remains the more difficult goal of obtaining optically active device structures within the Si-based technology. [2] In each of these cases, the relevant electronic structure of the device is completely dependent on the local structure, composition, and strain within a few Angstrom units of an internal interface. In the past, electron microscopy has been very successful at determining the local structure of buried interfaces and defects, but has not provided a good tool for measurement of either the bonding or the electronic structure in the same areas. Spatially Resolved EELS has therefore been devised as a technique to obtain the bulk electronic structure in a way that is compatible with electron microscopy so that direct comparisons can be made between electronic and atomic structure.

The instrument used in these studies is based on the VG Microscopes HB501 Scanning Transmission Electron Microscope (STEM). With modifications made at IBM, this instrument produces a 1.95Å probe of electrons at 120KeV energy for use in Annular Dark Field "Z-Contrast" imaging. [3] This imaging mode produces easily interpretable atomic resolution images having atomic number contrast. [4] Electron Energy Loss Spectroscopy (EELS) is accomplished with a Wien Filter spectrometer constructed at IBM. This instrument obtains an energy resolution of about 0.2eV with an energy axis accuracy of $\pm$20meV using the 1.95Å probe comprising a transverse momentum spread of about $3Å^{-1}$. [5] Therefore, Spatially Resolved EELS, with its inherent average over transverse momentum, is the natural compliment to Angle Resolved EELS, which obtains wavevector resolved spectra integrated over large specimen areas.

In these studies, we use the Si $2p_{3/2}$ core absorption Energy Loss Near Edge Structure (ELNES) to tell us about the conduction bandstructure close to the probed Si atom. This turns out to be possible throughout the Si-Ge alloy system, both in the relaxed [6][7] and strained [8] situations. Figure 1 shows a set of these spectra for relaxed Ge-Si alloys having Ge content ranging over 0-95%. The shape of the spectra can be understood using a model for the symmetry-projected local Density of States, indicated by the dashed lines. This reflects contributions from the s-like conduction band minimum at Δ_1, the s-like local minimum in the [111] direction L_1 and a d-like saddle point at L_3. To compare this model with the measured data, it is inserted into a scattering theory that includes effects due to instrumental resolution, lifetime broadening and core excitonic distortion [9], producing the solid line fits. Movement of the three major critical points can then be tracked as a function

of composition. In addition, it turns out that the Si 2p core level provides a fixed reference energy for this system [7], so we are able to use the absolute position of the absorption edge as a measure of the conduction band offset as a function of either alloy composition or position on the sample. Thus, in Figure 1, we can track the upwards shift of Δ_1 and the downwards shift of L_1 as we add Ge to Si. Near 85%, consistent with the optical data, there is a cross over which places L_1 as the conduction band minimum.
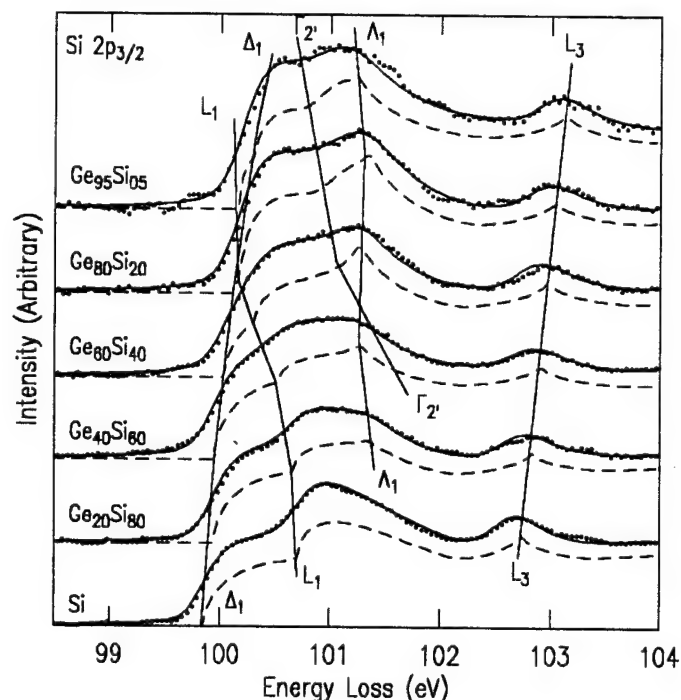
Figure 1. Summary of data, DOS models (dashed lines) and resulting fits to the data (solid lines) for a range of relaxed Si-Ge alloys. The major critical points revealed are Δ_1, L_1 and L_3. In order to match the measured data, the DOS model functions have to be inserted into a scattering theory that includes effects due to the core exciton, instrumental resolution, and lifetime damping. Because the core level is constant as a function of Ge content in this alloy, the measured positions are absolute and provide measures of heterojunction band offsets in completed devices.

$\Gamma_{2'}$ is dipole forbidden, but is symmetry compatible with the Λ_1 line which eventually terminates at the dipole allowed L_1. Therefore it is needed to model the observed data, and can be inferred with somewhat reduced accuracy. The descent of $\Gamma_{2'}$ with Ge content, weakly inferred by the data, is expected from the bandstructure calculations. Λ_1 here is used to denote a saddle point in the Λ_1 branch which is produced by the descent of $\Gamma_{2'}$. L_3 follows its symmetry compatible conduction band minimum Δ_1.

The measured positions, particularly of the conduction band minimum, Δ_1, are useful because they reflect the heterojunction offsets present in real devices. For instance, the heterojunction band offset in a strained Si quantum well was measured to be 170meV, in agreement with the calculated value, and consistent with that needed to produce adequate screening of charge carriers from potential fluctuations caused by dopant atoms. [10] In Figure 2, the conduction band offset has been measured as a function of position through a 10nm Si quantum well. The dark field image shows the lower atomic number Si to be darker than the $Ge_{30}Si_{70}$ buffer and spacer layers. A line scan of the dark field intensity shows the Ge content, including fluctuations caused by the high resolution imaging of atomic double columns. The band offset data is superposed to show that it roughly follows the composition on the buffer (substrate) side, but appears to change more rapidly than the composition on the spacer (top) side.

At the present time, the systematic variation of these results with composition, strain, proximity to defects and interfaces, and interfacial roughness are all being examined. Interpretation of both the EELS data and the dark field images are still uncertain to some extent. And in spite of the obvious spectral trends, the instrumental requirements are still demanding, leading to some uncertainty in the measured quantities. However, these results clearly demonstrate that Spatially Resolved EELS provides an extremely rich set of information with a high sensitivity to local atomic structure in buried volumes.
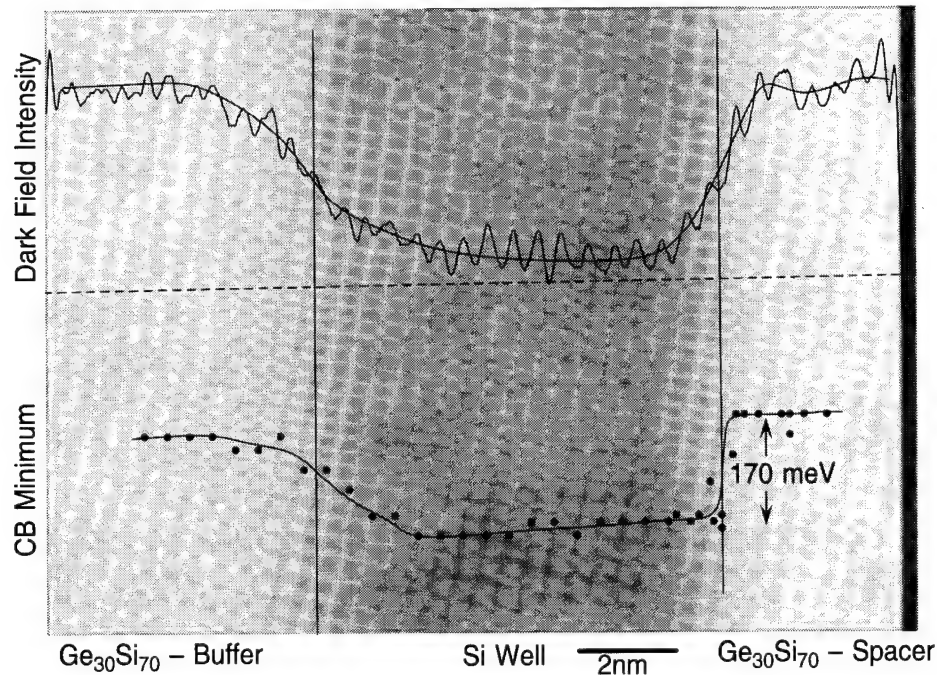
Figure 2. Dark Field image of atomic composition of a strained Si quantum well. Upper line shows a rough indication of the Ge content. The lower line shows the heterojunction band offset determined from the threshold energies of spectra similar to those shown in Figure 1. The band offset follows the composition on the left, but appears to be sharper than the composition on the right.

References:
[1] K. Ismail, J.O. Chu, K.L. Saenger, B.S. Meyerson, and W. Rausch, Appl. Phys. Lett., **65** 1248 (1994).
[2] T.P. Pearsall, Prog. Quant. Electr., **18** 97 (1994).
[3] P.E. Batson, Ultramicroscopy, in press.
[4] S.J. Pennycook, and L.A. Boatner, Nature, **336** 565. (1988)
[5] P.E. Batson, Rev. Sci. Inst., **57** 43 (1986).
[6] P.E. Batson and J.F. Morar, Appl. Phys. Lett., **59** 3285 (1991).
[7] J.F. Morar, P.E. Batson and J. Tersoff, Phys. Rev. B, **47** 4107 (1993).
[8] P.E. Batson and J.F. Morar, Phys. Rev. Lett., **71** 609 (1993).
[9] P.E. Batson, Phys. Rev. B, **47** 6898 (1993).
[10] F. Stern and S.E. Laux Appl. Phys. Lett., **61** 1110 (1992).

Fabrication and Properties of Ultrathin Films of Porous Silicon

P.M. Fauchet

Department of Electrical Engineering
University of Rochester NY 14627

Voice: (716) 275-1487
Fax: (716) 275-2073
email: fauchet@ee.rochester.edu

We have manufactured thin films of light-emitting porous silicon (LEPSi) by electrochemical etching in HF and subsequently lifted them off the silicon wafer by an electropolishing step [1]. The film thickness was varied from 100 μm to 0.1 μm and the porosity ranged from < 40% to ≥ 90%. To insure the structural integrity of the thinner, higher porosity films, they were deposited on sapphire windows where they remain attached by van der Waals or electrostatic forces, in a manner reminiscent of earlier work with ultrathin film of III-V semiconductors [2]. The microstructural, chemical and optical properties of these films have been investigated using a variety of tools, including AFM, XRD, FTIR, cw and time-resolved absorption and luminescence measurements. These films are optically flat (see Fig. 1), do not scatter light, show pronounced Fabry-Perot interference fringes in the transparency region which can extend to photon energies well above the bandgap of crystalline silicon (see Fig. 2) and can have a refractive index as low as 1.2 to 1.3. The peak of the luminescence spectrum, which is determined by quantum size effects and surface chemistry, has no clear relation to the onset of absorption, which is dominated by the largest nanocrystallites. The broad luminescence spectrum splits into a few narrow peaks which are produced by multiple interference (see Fig. 3).

Because of their unusual properties, these LEPSi films can find many uses in science and technology. They have allowed us to perform photoinduced absorption measurements with 100 femtosecond time resolution that reveal the

first step in the carrier dynamics, namely the trapping of carriers in surface states and they promise to be useful in resolving the controversy concerning the origin of the luminescence in porous silicon. They can also be used for different device applications, such as active waveguides or antireflection coatings to low index substrates such as glass. Several examples will be discussed.

Ackowledgments

References

1.   J. von Behren, L. Tsybeskov and P.M. Fauchet, submitted for publication
2.   T. Gong, W.L. Nighan Jr. and P.M. Fauchet, Appl. Phys. Lett. 57, 2713 (1990)
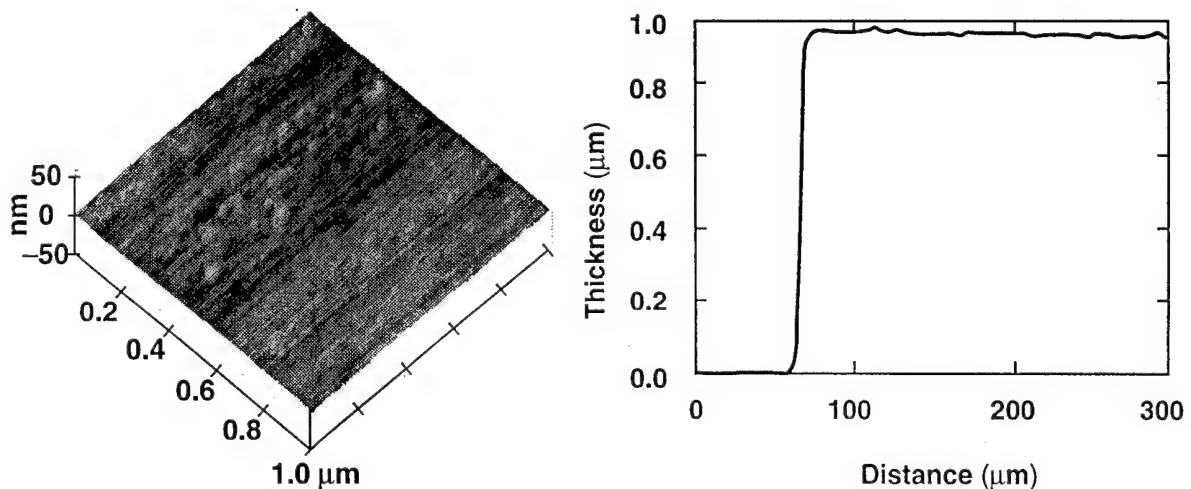
Figure 1

Atomic force microscope image and profilometer scan of a 0.94 μm thick porous silicon film deposited on a sapphire substrate.
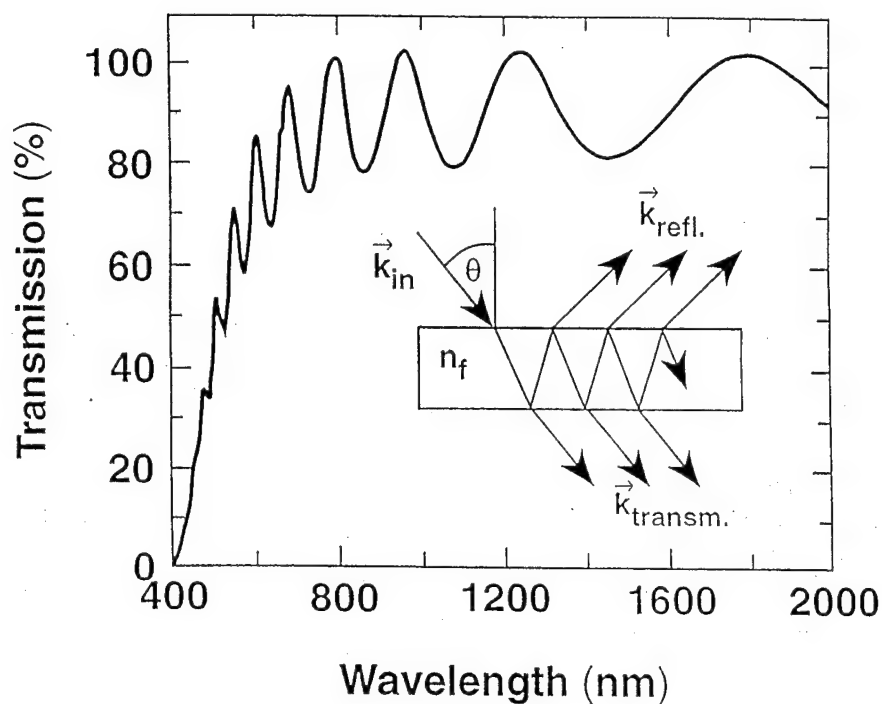
Figure 2

Transmission spectrum of the film of Fig.1. The film is opaque below 400 nm and at longer wavelengths it exhibits pronounced Fabry-Perot fringes.
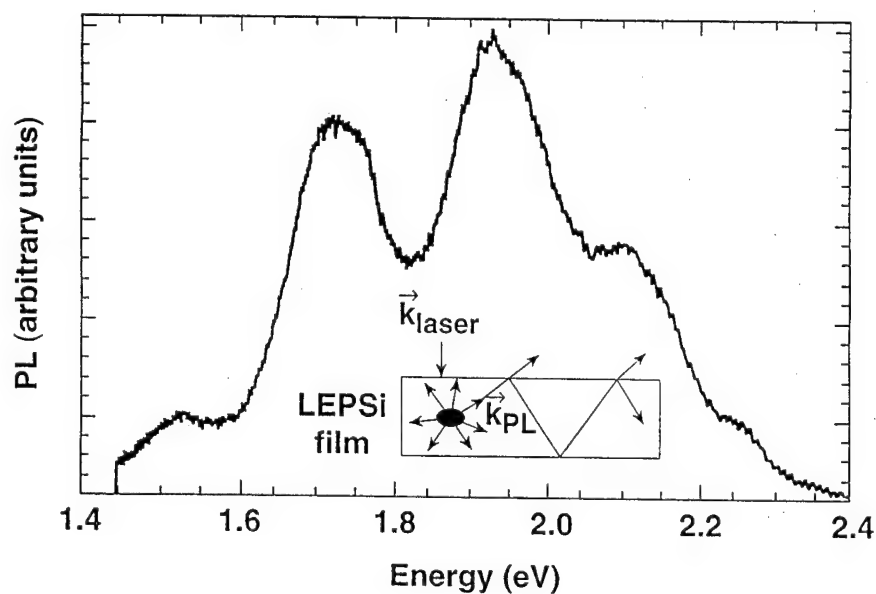

Figure 3

Time-integrated PL spectrum of the film of Fig. 1. The broad spectrum breaks into several peaks produced by multiple interference. The excitation wavelength is 337 nm.

PHOTOLUMINESCENCE AND ELECTROLUMINESCENCE OF Ge-IMPLANTED Si/SiO$_2$/Si STRUCTURES.

K.V. Shcheglov, C.M. Yang, and H.A. Atwater, Thomas J. Watson Laboratory of Applied Physics, California Institute of Technology, Pasadena, CA 91125, tel.: (818) 395-2154; fax: (818) 395-2944.

Although it was observation of efficient photoluminescence [PL] from porous silicon that prompted numerous investigations into the optoelectronic properties of group IV semiconductor nanocrystals, there is interest in other related materials which are more robust in various chemical and thermal ambients and which can be easily incorporated into standard silicon VLSI processing. A promising approach that meets the above requisites is synthesis of semiconductor nanocrystals in an SiO$_2$ matrix accomplished by various techniques. In this letter we report on the fabrication of a Ge nanocrystal-based electroluminescent device using ion implantation and precipitation.

Samples consisted of 45 nm thick polycrystalline Si films deposited by ultrahigh vacuum electron beam evaporation onto 70 nm thick SiO$_2$ films thermally grown on n+ Si substrates. These were implanted with Ge at doses of 4×10^{16} /cm^2 at 140 keV and 1×10^{16} /cm^2 at both 130 and 150 keV, the energies being chosen to create a supersaturated solid solution of Ge in SiO$_2$ with approximately uniform Ge concentration of 5 atomic % throughout the oxide. The samples were subsequently annealed at 600 °C at high vacuum (1×10^{-6} torr.) for 40 min. to induce precipitation, the top layer was p-doped with B in a furnace at 900 °C for 15 min. Other experiments suggest that Ge nanocrystal growth continued during this 900 °C anneal. Finally photolithography was used to define mesas for individual devices and to define Al contacts using lift-off.

Figure 1(a) is a bright-field cross-sectional transmission electron micrograph of the completed device prior to metal contact deposition. Visible on top is the polycrystalline p+ layer with grain sizes comparable with film thickness. Below is the SiO$_2$ layer, with the speckles corresponding to numerous Ge nanocrystals, also visible in the accompanying dark-field image of the same region shown in Fig. 1(b).
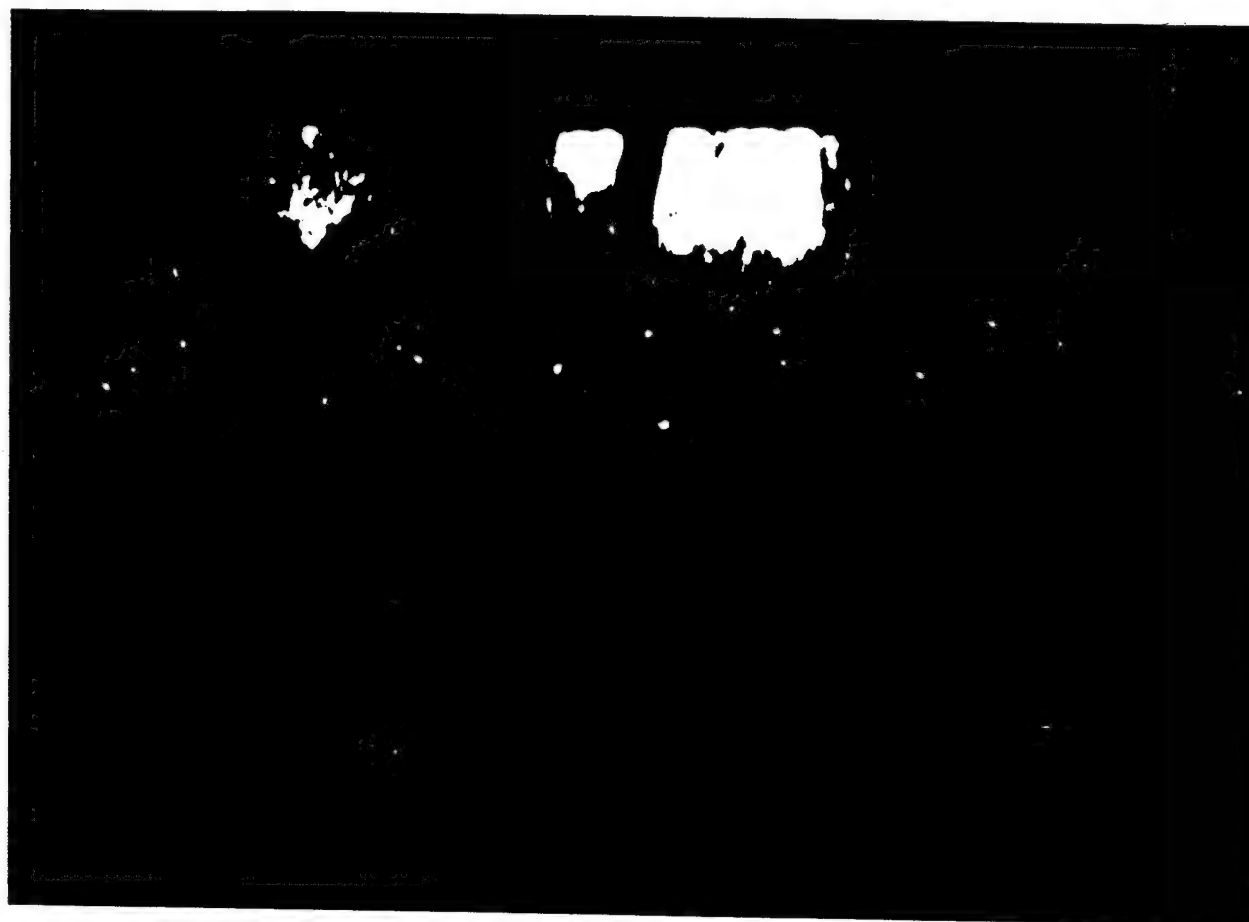
The current-voltage characteristic of a typical device is shown in Fig. 2. Rectifying behavior is seen in forward bias and a relatively broad breakdown feature is seen in reverse bias between -5 V and -10 V. Electroluminescence [EL] is characterized by an onset at reverse bias less than approx. -10 V, which corresponds to an electric field in the oxide greater than 10^6 V/cm. The strongly luminescent area covered approximately 10 % of the device surface, probably due to thickness non-uniformities of the oxide. Figure 3 shows a comparison between PL and EL spectra. The onset of luminescence occurs around 500 nm, the narrow feature there being a calibration-amplified noise artifact. A luminescence efficiency of 10^{-4} was estimated.

We speculate that EL excitation proceeds by extended state carrier transport in SiO$_2$ followed by trapping into localized states associated with the Ge nanocrystals. It is important to note that emission via black-body radiation is most likely insignificant, since it would require local temperatures in excess of 900 °C, resulting in significant microstructural and optical changes in the process of operation. Pump densities of (.5 - 5 W/cm^2) are unlikely to produce enough heating in the film which is in intimate thermal contact with 2 cm^2 of Si substrate.
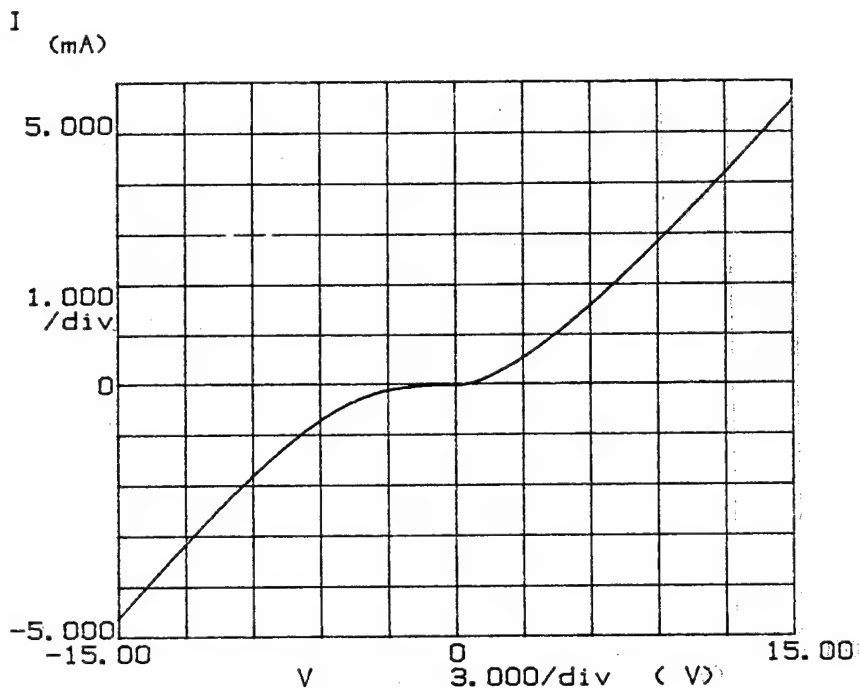
(a)

50 nm
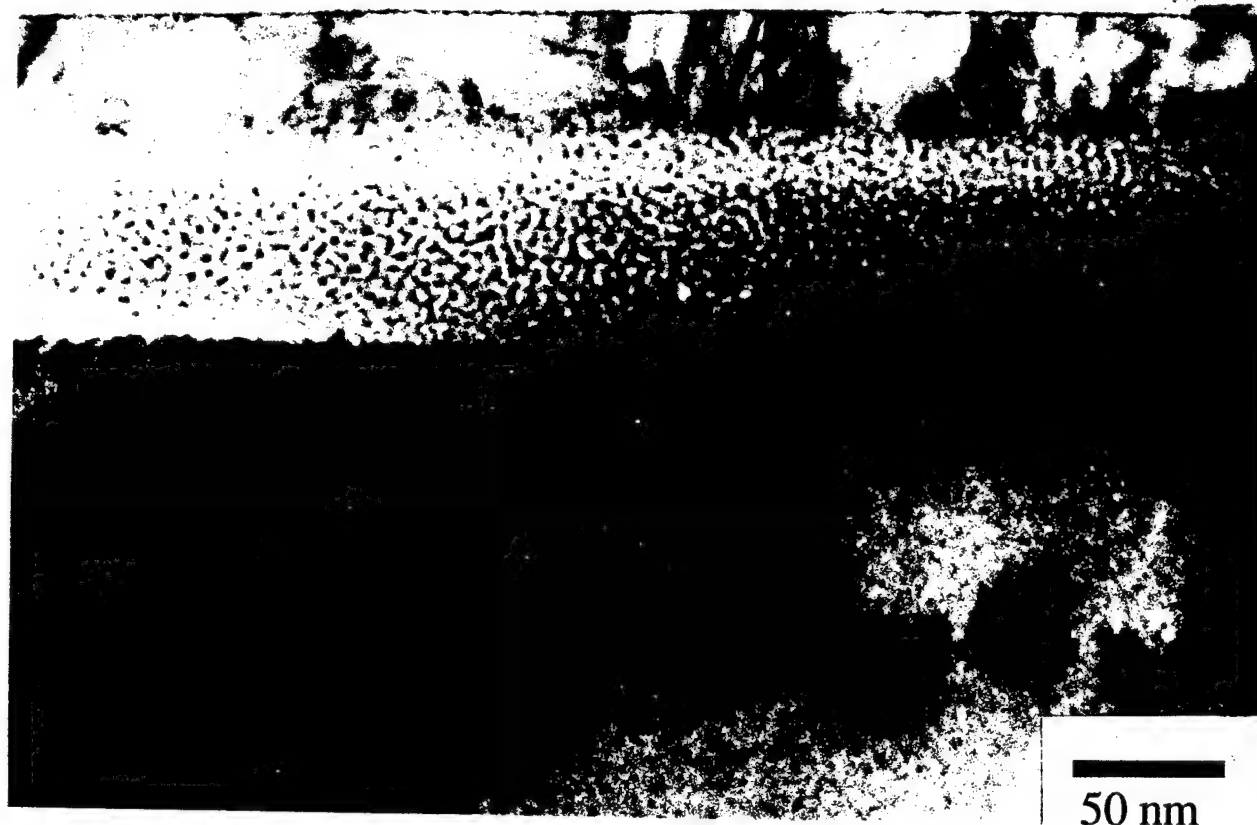
(b)

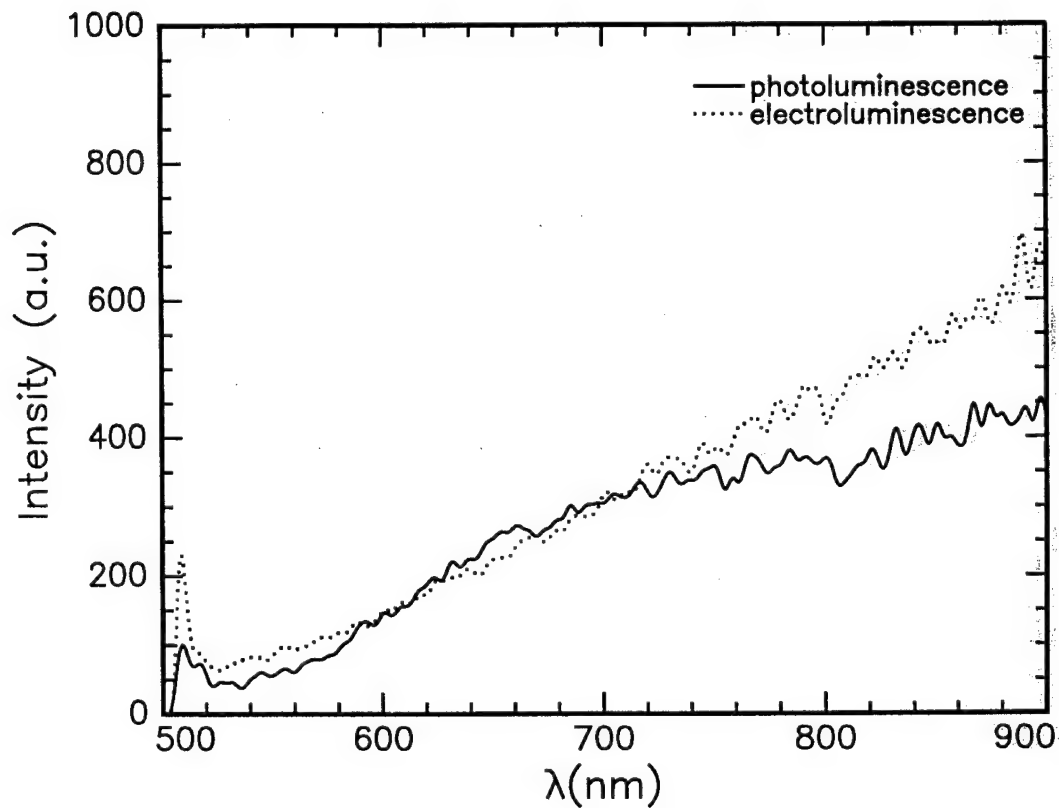Figure 2. The current-voltage characteristic of a typical device.

Figure 3. Photoluminescence and Electroluminescence spectra for a typical device operating in reverse breakdown. Spectra are corrected for the system response of the optical spectrometer.

CORRELATION OF SIZE AND PHOTOLUMINESCENCE FOR GE NANOCRYSTALS IN SIO₂ MATRICES.

C.M Yang, K.V.Shcheglov, K.J.Vahala and H.A.Atwater
Thomas J. Watson Laboratory of Applied Physics
California Institute of Technology
Pasadena, CA 91125.
Telephone: (818) 395-3826
Fax: (818) 395-2944

Thermally-grown silicon dioxide films 100 nm thick were implanted with 70 keV Ge ions at a dose of 2 x 10^{16}/cm². These samples were subsequently annealed for 40 min. at 600 °C, 800 °C, 1000 °C and 1200 °C. Plan-view transmission electron microscopy (TEM) was performed to obtain crystal size distributions. Photoluminescence spectra were measured at room-temperature, excited by 50 mW of 457 nm radiation from an Ar ion laser and spectra were acquired by a charged-coupled-device optical multichannel analyzer (OMA) spectrometer with optical fiber input. The system response of the OMA spectrometer was calibrated using a black body radiation source, and all spectra are corrected for the system response of the spectrometer.

Figure 1(a)-(d) shows bright field TEM images of samples that were treated with 40 min anneals at 600 °C, 800 °C, 1000 °C and 1200 °C, respectively. Figure 2 shows the Gaussian fits to the nanocrystal size distributions, which were used to generate predicted PL spectra.

Figure 3(a) shows a set of observed PL spectra for samples annealed at 600 °C, 800 °C, 1000 °C, and 1200 °C. To model the PL spectra, we assume for simplicity that a Ge nanocrystal is a two-level system, and thus that photoexcited carriers with greater than band gap energy relax instantaneously to the minimum of the conduction band. Nanocrystals of a given radius were assumed to emit at a single wavelength, and calculated values for the size-dependent optical energy gap and size-dependent radiative carrier recombination rate were obtained from the effective mass exciton recombination model of Ref.[1].

Assume that a nanocrystal of radius r, which is excited by a pump power I_p, has an absorption efficiency A at pump wavelength. Furthermore, let $N(r)$ be the number of nanocrystals, and $f(r)$ be the fraction of nanocrystals of radius r that are excited. The absorption, radiative emission and nonradiative emission rates are all assumed to be size-dependent. The size-dependent radiative emission rate, $Y_r(r)$, is taken directly from [1]. The nonradiative emission rate $Y_n(r)$ is assumed to be proportional to the average number of electronic states at the nanocrystal-matrix interface, and hence is proportional to the interface area. The absorption efficiency $A(r)$ is taken to be the complex bulk Ge refractive index, scaled by the particle volume, and shifted in wavelength by the energy gap as a function of size from Ref. [1]. The absorption efficiency is also assumed to be proportional to the nanocrystal volume. In steady state the excitation rate and the relaxation rate of the particles are equal, and one obtains

$$[Y_r(r) + Y_n(r)]f(r)N(r) = [1 - f(r)]N(r)I_pA(r) \tag{1}$$

where $f(r)$ is the excited fraction and $N(r)$ are the Gaussian fits to nanocrystal size distributions from Fig. 2. and thus the photoluminescence intensity in steady state, I_{PL}, is

$$I_{PL}(r) = f(r)N(r)Y_r(r) = \frac{I_pA(r)N(r)Y_r(r)}{I_pA(r) + Y_r(r) + Y_n(r)}. \tag{2}$$

The wavelength-dependent PL intensity $I_{PL}(\lambda)$ is calculated by converting radius r in the above equation into wavelength λ using the calculated energy gaps $E_g(r)$ from Ref. [1].

Figures 3(b)-3(d) show sets of spectra calculated using Eq. 2 and the four particle size distributions from Fig. 2. For the calculated PL spectra in Fig. 3(b), $Y_r(r)$ is assumed to dominate the non-radiative decay rate $Y_n(r)$ and the pumping rate, which is the product of the pump intensity and absorption rate, $I_pA(r)$. For the calculated spectra in Fig. 3(c), $Y_n(r)$ is assumed to dominate the other two rates.
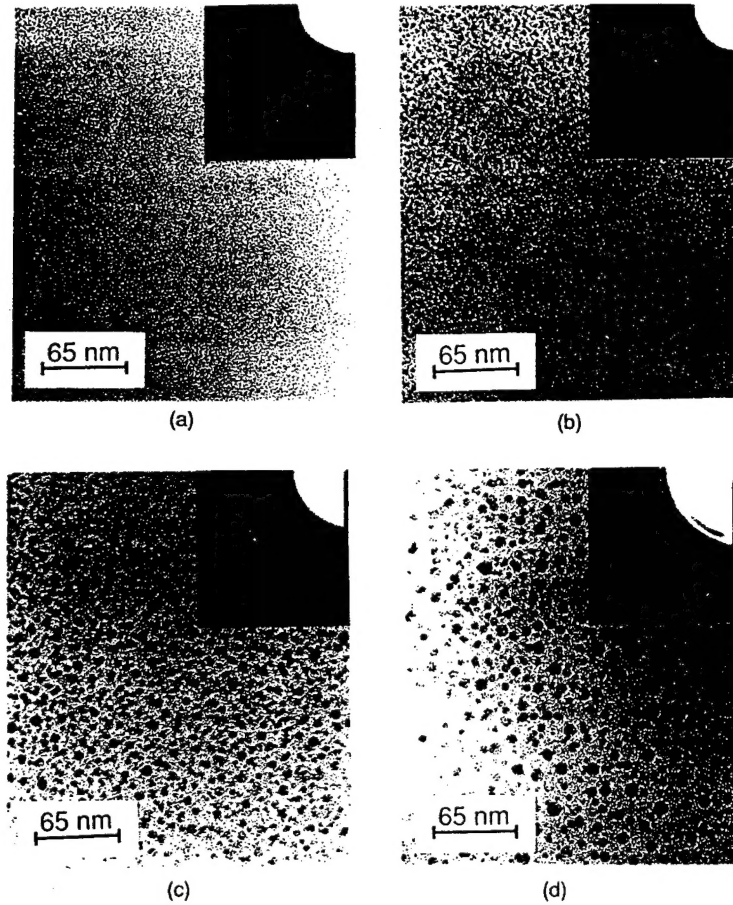
Figure 1: Bright-field transmission electron micrographs of Ge nanocrystals annealed for 40 min at (a) 600 °C, (b) 800 °C, (c) 1000 °C, and (d) 1200 °C.

A better—though not ideal—fit to experimental PL spectra, shown in Fig. 3(d), can be obtained by making several assumptions. First, we assume that $Y_n(r) \simeq Y_r(r)$ for $r \simeq 2.0$ nm. Second, we assume that a small fraction of the nanocrystals present in the samples annealed at 600 °C consist of two nanocrystals which have coalesced, and thus result in an electronic state which corresponds effectively to one nanocrystal of twice the volume of the isolated nanocrystals. This assumption is well supported by images such as Fig. 1(a), which show a very high nanocrystal density in this sample. A final assumption is that for all samples the "electronic" radius, r_{el}, (i.e., the radius of the confining potential) is $r_{el} = 0.75r$. While the last is an *ad hoc* assumption, it can be physically motivated. An "electronic" radius which is smaller than the radius measured by electron microscopy may indicate the presence of a complex interfacial region, which would give rise to a electronic confinement potential that deviates from a spherical hard shell of radius r. While this set of assumptions correctly yields the highest PL intensity for the samples annealed at 1000 °C, and it does yield PL peak intensities in the visible for all samples, it does not produce quantitative agreement with the experimental results. Indeed, we could not identify a set of reasonable physical assumptions which would yield quantitative agreement with the experimental results of Fig. 3(a).

References

[1] T. Takagahara and K. Takeda, Phys. Rev., **B46**, 15578 (1992).
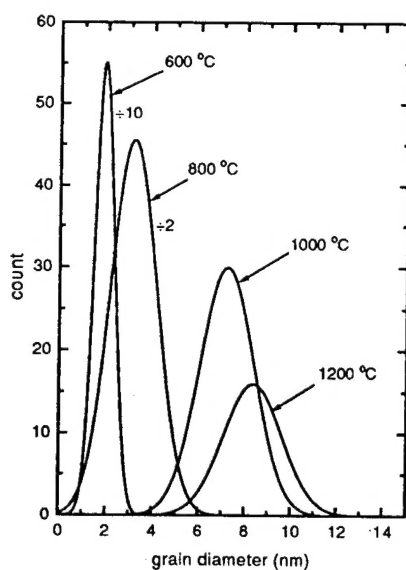
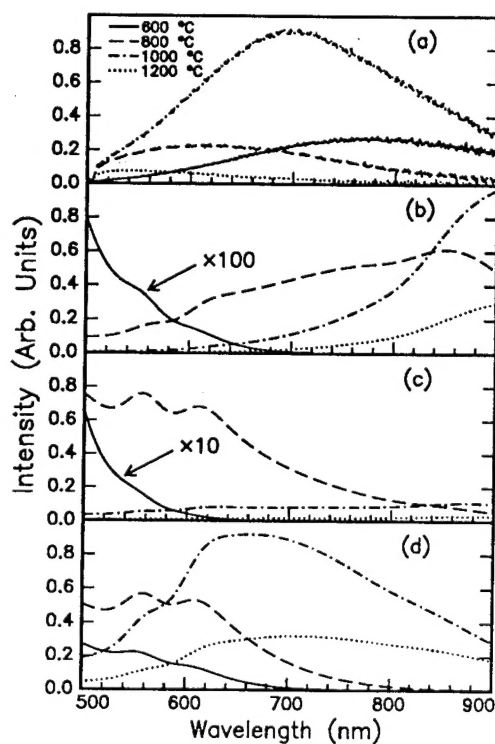Figure 2: Gaussian fits to the nanocrystal size distributions.

Figure 3: In (a), measured room-temperature PL spectra for samples annealed at 600 °C (solid lines), 800 °C (dashed lines), 1000 °C (dot-dashed lines) and 1200 °C (dotted lines). Calculated room-temperature PL spectra, using size distributions of Fig. 2, assuming (b) $Y_r(r) \gg Y_n(r)$, (c) $Y_r(r) \ll Y_n(r)$. In (d), calculated room-temperature PL spectra assuming $Y_r(r) \simeq Y_n(r)$, $r_e l = 0.75r$ and nanocrystal coalescence in the 600 °C sample (see text for details).

Adams, D. P. — MThA5
Ahn, C. C. — MFA4
Atwater, Harry A. — MFA4, MSaA, MSaB3, MSaB4
Avouris, Phaedon — MThA, MSaA3

Baltog, I. — MThD6
Barth, M. — MThD5
Batson, Philip E. — MSaB1
Behringer, E. R. — MThA2
Bennett, Jean M. — MThD4
Blanton, Sean A. — MSaA4
Bressler-Hill, V. — MThD1
Brewer, Peter — MFB1
Brus, Louis E. — MSaA1
Burr, T. A. — MSaA2

Celotta, R. J. — MThB3
Chason, E. — MThA4
Choi, S. S. — MThD7
Church, E. L. — MFA2
Coutaz, J.-L. — MThD6
Creighton, J. R. — MThC1

Dehestani, Ahmad — MSaA4
Denbaars, S. — MThD1
Dillon, A. C. — MThC2
Dirac, H. — MThD3

Eaton, H. K. — MThC2
Eres, Gyula — MThC3

Fauchet, P. M. — MSaB2
Fiddy, M. A. — MThD7
Frase, H. N. — MFA4

Gamo, Kenji — MThB2
George, Steven M. — MThC, MThC2, MFB4
Greene, Joe — MThB
Gupta, R. — MThB3
Guyot-Sionnest, Philippe — MSaA4

Hall, Richard — MFB
Harada, Yasunori — MThD2
Herman, Irving P. — MFA1
Hess, Peter — MThD5, MFA3
Hirose, Masataka — MFB3, MSaB
Hodgkin, Van A. — MThD4
Houston, J. E. — MThA3
Howard, A. J. — MThA4

Jensen, J. A. — MThA2

Karstens, H. — MThD5
Kellerman, B. K. — MThA4
Kendall, D. L. — MThA3
Knobloch, J. — MThD5

Kolenbrander, K. D. — MSaA2
Kummel, A. C. — MThA2

Lasky, P. J. — MFB2
Lin, Peter C. — MSaA4
Lu, P. H. — MFB2
Luo, Y. — MFB2

Marrian, Christie R. K. — MThB1
Matzke, C. M. — MThA3
Mayer, T. M. — MThA4, MThA5
McClelland, J. J. — MThB3
McWaid, Thomas — MThD4
Miyazaki, Seiichi — MFB3
Miyoshi, Yasutoshi — MFB3
Mullenborn, M. — MThD3

Olson, G. L. — MFB1
Osgood, Richard M., Jr. — MFA, MFB2
Ott, A. W. — MThC2

Petersen, J. W. — MThD3
Primeau, N. — MThD6
Puiu, Mecky — MThD4
Pusel, A. — MThD5

Reaves, C. M. — MThD1
Reinisch, R. — MThD6

Sato, Shunichi — MThD2
Shcheglov, K. V. — MSaB3, MSaB4
Slater, D. A. — MFB2
Sneh, Ofer — MFB4
Stover, J. C. — MFA2
Stuke, M. — MFB1
Sugimoto, Tadao — MThD2
Swartzentruber, B. S. — MThA3, MThA5

Takacs, P. Z. — MFA2
Truong, C. M. — MThC1

Vahala, K. J. — MSaB4
Varma, S. — MThD1

Waseda, Yoshio — MThD2
Way, J. D. — MThC2
Weaver, J. H. — MThA1
Weinberg, W. H. — MThD1
Winkler, A. — MThD5
Wise, Michael L. — MFB4
Wong, S. S. — MFA4

Yan, C. — MThA2
Yang, C. M. — MSaB3, MSaB4

Zinck, J. J. — MFB1